The
University
Of
Sheffield.

MOCVD Overgrowth and Characterisation of Nonpolar GaN on Patterned Templates on Sapphire for Advanced III-nitride Optoelectronics

Ling Jiu

The University of Sheffield

Department of Electronic and Electrical Engineering

Centre for GaN Materials and Devices

Supervisor: Professor Tao Wang

A thesis submitted for the degree of Doctor of Philosophy

July 2019

“*One man’s ‘magic’ is another man’s engineering.*”

— Robert Heinlein,

Time Enough for Love

Abstract

III-nitride semiconductors are expected to lead a revolution in general illumination, and they have been accepted to play a critical role in the fabrication of advanced optoelectronics. Currently, III-nitride optoelectronics are predominantly based on c-plane polar GaN, which has made unprecedented achievements in the last two decades but exhibits a number of fundamental limitations. In our team, non-polar (11-20) GaN with a step-change in crystal quality on widely used sapphire substrates has been achieved by developing cost-effective overgrowth approaches on patterned templates. Systematic investigation on the material structure and the material properties have been made. Finally, novel LEDs with great performance based on the non-polar GaN have been demonstrated.

Non-polar (11-20) GaN with significantly improved crystal quality has been achieved by means of overgrowth on regularly arrayed micro-rod templates on sapphire. The high crystal quality with a step-change has been characterised by X-ray rocking curve measurements showing massively reduced linewidth with typical values of 270 arcsec along the [0001] direction and 380 arcsec along the [1-100] direction. These values are among the best reported. Detailed X-ray measurements have been performed in order to investigate strain relaxation and in-plane strain distribution. It has been found that the standard non-polar GaN grown without involving any patterning processes typically exhibits highly anisotropic in-plane strain distribution, while the overgrown GaN on our regularly arrayed micro-rod templates shows a highly isotropic in-plane strain distribution.

A novel multiple-facet structure consisting of only semi-polar and non-polar GaN facets has been achieved by means of overgrowth on non-polar GaN micro-rod arrays on r-plane sapphire, which allows the major drawbacks of utilising c-plane GaN for the growth of III-nitride optoelectronics to be eliminated. InGaN multiple quantum wells (MQWs) are grown on the multiple-facet templates. Due to the different efficiencies of indium incorporation on semi-polar and non-polar GaN facets, multiple-colour InGaN/GaN MQWs have been obtained.

Photoluminescence (PL) measurements have demonstrated that the multiple-colour emissions with a tunable intensity ratio of different wavelength emissions can be achieved simply through controlling the overgrowth conditions. Detailed cathodoluminescence measurements and excitation-power dependent PL measurements have been performed, further validating the approach of employing the multiple facet templates for the growth of multiple colour InGaN/GaN MQWs.

InGaN MQWs light-emitting diodes (LEDs) have been grown on the above high-quality non-polar GaN templates on sapphire. PL measurements show one main emission peak at 418 nm along with another weak peak at 448 nm. Wavelength mapping measurements carried out by using a high spatial-resolution confocal PL system indicate that the two emissions origin from different areas associated with the underlying micro-rod patterns. Electroluminescence measurements exhibit a negligible blue-shift of 1.6 nm in the peak wavelength of the main emission with increasing injection current from 10 to 100 mA, indicating an effective suppression in quantum confined Stark effect in the non-polar LED. Polarisation measurements demonstrate a polarisation ratio of 0.49 for the low-energy emission (~448 nm), while the main emission (~418 nm) shows a polarisation ratio of 0.34. Furthermore, the polarisation ratios are independent of injection current, while the energy separation between m-polarized and c-polarized lights increases with the injection current for both emissions.

The crystal quality of non-polar (11-20) GaN has been further improved by means of the double overgrowth approach, i.e. first overgrowth on micro-stripes and second overgrowth on micro-rods. The double overgrowth technique takes advantages of both kinds of overgrowths, which allows more effective dislocation and BSF blocking, without the sacrifice of sample morphology. A comparative study has been carried out on the non-polar (11-20) GaN grown on micro-rod templates, micro-stripe templates and also through the double overgrowth technique. The mechanism of defect reduction was revealed by transmission electron microscopy characterisation, which further validates the effectiveness of the double overgrowth technique.

Acknowledgements

This thesis marks the end of my journey of pursuing a PhD degree. During the past few years, many have helped and assisted me. None of these would be possible without them. Therefore, here, I would like to take this precious opportunity to express my deepest gratitude to those who have walked with me all the way through this journey.

My first thanks must go to Professor Tao Wang, who is a remarkably skilful, knowledgeable and intellectual mentor to me. His words and deeds not only benefited me substantially in my research but also shaped my personality and truly changed the trajectory of my life. Thank you.

I would like to thank Dr. Jie Bai for her assistance on the device fabrication and measurement of EL and TEM data included in this thesis. She also shared lots of instructive advice on my research and helped me with proofreading of this thesis.

I would like to offer my special thanks to Dr. Yipin Gong, who worked closely with me on the project. Without his help on the growth and contribution in the discussion, this work would be impossible to complete.

I would like to express my gratitude to all my group members: Dr. Rick Smith, Dr. Xiang Yu, Dr. Yaonan Hou, Dr. Kun Xing, Dr. Modestos Athanasiou, Dr. Yuefei Cai, Dr. Benbo Xu, Dr. Yun Zhang, Mr. Shuoheng Shen, Mr. Zohaib Ahmed, Mr. Peter Fletcher, Mr. Xuanming Zhao, Mr. Chenqi Zhu, Mr. Peng Feng, and Mr. Ye Tian, for their kind support and for the valuable feedback during my PhD. It is an honour to work with them. Especially, I would like to express my very great appreciation to those who have had a vital role in this project. Thank Dr. Kun Xing for initiating me into the fabrication and sharing his valuable experience and expertise on the template fabrication. Thank Dr. Benbo Xu for teaching me a variety of characterisation techniques and all the in-depth discussion about everything. Thank Mr. Peter Fletcher for measuring confocal PL data presented in this thesis. I would also like to offer my special thanks to Professor Robert Martin and Dr.

Jochen Bruckbauer as well as their team members from the University of Strathclyde for helping me with the CL measurement.

I would like to acknowledge the support provided by technicians and staffs from our EEE department and the National Epitaxy Facility. I owe a great debt to Mr. Paul Haines for his extensive technical support on the fabrication instruments and the MOCVD. I would like to thank Dr. Kenneth Kennedy, Dr. Rob Airey, Dr. Paul Fry and Mr. Saurabh Kumar, for their guidance and coaching on various equipment. I would also like to thank Mr. Jon Milner and Mr. Stephen Atkin for the routine management and maintenance of the cleanroom. My special thanks go to Mr. Gordon Askwith, who is a good man. Thank him for inspiriting me with his magical brilliance aura.

Finally, I want to give my heartfelt gratitude to my family. Thank my parents, especially my mother, for their support, both materially and spiritually. I would also like to thank my grandfather, who is a brilliant engineer, and my grandmother, who is a dedicated doctor. It was them who inspired my interest in engineering and my pursuit of science. Thank you and love you all.

Ling Jiu
Sheffield, UK
01/06/2019

List of Publications

Journal Publications

1. C. Trager-Cowan, A. Alasmari, W. Avis, J. Bruckbauer, P. Edwards, B. Hourahine, S. Kraeusel, G. Kusch, R. Johnston, G. Naresh-Kumar, R. Martin, M. Nouf-Allehiani, E. Pascal, L. Spasevski, D. Thomson, S. Vespucci, P. Parbrook, M. Smith, J. Enslin, F. Mehnke, M. Kneissl, C. Kuhn, T. Wernicke, S. Hagedorn, A. Knauer, V. Kueller, S. Walde, M. Weyers, P. Coulon, P. Shields, Y. Zhang, **L. Jiu**, Y. Gong, R. Smith, T. Wang, and A. Winkelmann, *"Scanning electron microscopy as a flexible technique for investigating the properties of UV-emitting nitride semiconductor thin films"*, Photon. Res. 7, B73-B82 (2019).
2. J. Bai, **L. Jiu**, N. Poyiatzis, P. Fletcher, Y. Gong and T. Wang, *"Optical and polarization properties of nonpolar InGaN-based light-emitting diodes grown on micro-rod templates*", Sci. Rep. 9(1), 9770, (2019).
3. Y. Zhang, R. M. Smith, **L. Jiu**, J. Bai and T. Wang, *"Confocal photoluminescence investigation to identify basal stacking fault's role in the optical properties of semi-polar InGaN/GaN lighting emitting diodes*", Sci. Rep. 9(1), 9735, (2019).
4. Y. Cai, X. Yu, S. Shen, X. Zhao, **L. Jiu**, C. Zhu, J. Bai and T. Wang, *"Overgrowth and characterization of (11-22) semi-polar GaN on (113) silicon with a two-step method*", Semicond. Sci. Tech. 34, 045012, (2019)
5. Y. Gong, **L. Jiu**, J. Bruckbauer, J. Bai, R.W. Martin, T. Wang, *"Monolithic multiple colour emission from InGaN grown on patterned non-polar GaN*", Sci. Rep. 9(1), 986, (2019).
6. J. Bai, **L. Jiu**, Y. Gong, T. Wang, *"Non-polar (11-20) GaN grown on sapphire with double overgrowth on micro-rod/stripe templates*", Semicond. Sci. Tech. 33(12), 125023, (2018)
7. Y. Cai, C. Zhu, **L. Jiu**, Y. Gong, X. Yu, J. Bai, V. Esendag, T. Wang, *"Strain Analysis of GaN HEMTs on (111) Silicon with Two Transitional* $Al_xGa_{1-x}N$ *Layers*", Materials 11(10), 1968. (2018)

8. **L. Jiu**, Y. Gong, T. Wang, *"Overgrowth and strain investigation of (11–20) non-polar GaN on patterned templates on sapphire*", Sci. Rep. 8(1), 9898, (2018)
9. G. Naresh-Kumar, D. Thomson, Y. Zhang, J. Bai, **L. Jiu**, X. Yu, Y. P. Gong, R.M. Smith, T. Wang, C. Trager-Cowan, *"Imaging basal plane stacking faults and dislocations in (11-22) GaN using electron channelling contrast imaging*", J. Appl. Phys. 124(6), 065301, (2018)
10. C. Brasser, J. Bruckbauer, Y. Gong, **L. Jiu**, J. Bai, M. Warzecha, P.R. Edwards, T. Wang, R.W. Martin, *"Cathodoluminescence studies of chevron features in semi-polar InGaN/GaN multiple quantum well structures*", J. Appl. Phys. 123(17), 174502, (2018)
11. Y. Hou, Z. Ahmed Syed, **L. Jiu**, J. Bai, and T. Wang, *"Porosity-enhanced solar powered hydrogen generation in GaN photoelectrodes*", Appl. Phys. Lett. 111(20), 203901, (2017)
12. J. Bruckbauer, Z. Li, G. Naresh-Kumar, M. Warzecha, P. R. Edwards, **L. Jiu**, Y. Gong, J. Bai, T. Wang, C. Trager-Cowan, R.W. Martin, *"Spatially-resolved optical and structural properties of semi-polar (11-22) $Al_xGa_{1-x}N$ with x up to 0.56*", Sci. Rep. 7(1), 10804, (2017)
13. B. Xu, **L. Jiu**, Y. Gong, Y. Zhang, L.C. Wang, J. Bai, and T. Wang, *"Stimulated emission from semi-polar (11-22) GaN overgrown on sapphire*", Aip. Adv. 7(4), 045009, (2017)
14. Z. Li, L. Wang, **L. Jiu**, J. Bruckbauer, Y. Gong, Y. Zhang, J. Bai, R.W. Martin, and T. Wang, *"Optical Properties of Semi-polar (11-22) $Al_xGa_{1-x}N$ with High Al Composition*", Appl. Phys. Lett. 110(9), 091102, (2017)
15. Z. Li, **L. Jiu**, Y. Gong, L. Wang, Y. Zhang, J. Bai, and T. Wang, *"Semi-polar (11-22) AlGaN on overgrown GaN on micro-rod templates: Simultaneous management of crystal quality improvement and cracking issue*", Appl. Phys. Lett. 110(8), 082103, (2017)

Conference Contributions

1. **L. Jiu**, J. Bai, N. Poyiatzis, P. Fletcher, and T. Wang, *"Nonpolar (11-20) InGaN/GaN light-emitting diodes overgrown on a micro-rod Template"*,

Presented at the Semiconductor and Integrated Opto-Electronics, Cardiff, UK, 16th-18th April 2019.

2. Y. Cai, S. Shen, X. Yu, X. Zhao, **L. Jiu**, C. Zhu, J. Bai, and T. Wang, *"A two-step method of growing (11-22) semi-polar GaN on (113) silicon"*, Presented at the Semiconductor and Integrated Opto-Electronics, Cardiff, UK, 16th-18th April 2019.
3. **L. Jiu**, J. Bai, N. Poyiatzis, P. Fletcher, Y. Gong, and T. Wang, *"Nonpolar a-plane (11-20) InGaN-based light-emitting diodes grown on micro-rod templates"*, Presented at the UK Nitrides Consortium Winter, Glasgow, UK, 9th-10th January 2019.
4. **L. Jiu**, Y. Gong, J. Bruckbauer, J. Bai, R. W. Martin and T. Wang, *"Monolithic multiple colour emission from InGaN grown on patterned non-polar GaN"*, Presented at the UK Nitrides Consortium Winter, Glasgow, UK, 9th-10th January 2019.
5. **L. Jiu**, Y. Gong, and T. Wang, *"Morphology and strain evolution in non-polar a-plane GaN overgrown on patterned templates"*, Presented at the Semiconductor and Integrated Opto-Electronics, Cardiff, UK, 27th-29th March 2018.
6. **L. Jiu**, Y. Gong, and T. Wang, *"A study of stain evolution during overgrowth of (11-20) non-polar GaN on patterned templates on sapphire"*, Presented at the UK Nitrides Consortium Winter, Manchester, UK, 10th-11th January 2018.
7. J. Bruckbauer, G. Naresh-Kumar, Z. Li, **L. Jiu**, P. R. Edwards, J. Bai, T. Wang, C. Trager-Cowan, and R. W. Martin, *"Optical and structural properties of semi-polar (11-22) AlGaN epilayers with high AlN content"*, Presented at the International Symposium on Semiconductor Light Emitting Devices, Alberta, Canada, 8th-12th Oct 2017.
8. C. Brasser, J. Bruckbauer, Z. Li, **L. Jiu**, J. Bai, P. R. Edwards, T. Wang and R. W. Martin, *"Luminescence and conductivity studies of chevrons in semi-polar (11-22) InGaN/GaN multiple quantum well structures",* Presented at the International Conference on Nitride Semiconductors, Strasbourg, France, 24th-28th July 2017.

9. **L. Jiu**, Y. Gong, Z. Li, Y. Zhang, and T. Wang, *"Greatly Improved Crystal Quality of (11-20) Non-polar GaN Overgrown on Regularly Arrayed Micro-Rod Templates",* Presented at the UK Nitrides Consortium Summer, Sheffield, UK, 12th-13th July 2017.
10. **L. Jiu**, Y. Gong, Y. Zhang, Z. Li, J. Bai and T. Wang, *"High quality non-polar (11-20) GaN overgrown on mask-patterned micro-rod arrayed templates"*, Presented at the Semiconductor and Integrated Opto-Electronics, Cardiff, UK, 18th-20th April 2017.
11. Z. Li, L. Wang, **L. Jiu**, J. Bruckbauer, Y. Gong, Y. Zhang, J. Bai, R. W. Martin, and T. Wang, *"Optical Investigation of Semi-polar (11-22) $Al_xGa_{1-x}N$ with High Al Composition on overgrown GaN"*, Presented at the Semiconductor and Integrated Opto-Electronics, Cardiff, UK, 18th-20th April 2017.
12. B. Xu, Y. Zhang, **L. Jiu**, Y. Gong, L. C. Wang, J. Bai and T. Wang, *"Stimulated Emission from Semi-polar (11-22) GaN Overgrown on Sapphire",* Presented at the UK Nitrides Consortium Winter, Oxford, UK, 5th-6th Jan 2017.
13. Z. Li, L. Wang, **L. Jiu**, J. Bruckbauer, Y. Gong, Y. Zhang, J. Bai, R. W. Martin and T. Wang, "*Exciton Localization of Semi-polar (11-22) $Al_xGa_{1-x}N$ with High Al Composition*", Presented at the UK Nitrides Consortium Winter, Oxford, UK, 5th-6th Jan 2017.
14. Z. Li, **L. Jiu**, Y. Gong, L. Wang, Y. Zhang and T. Wang, *"Growth and optical investigation of semipolar (11-22) AlGaN with high Al composition on overgrown GaN on micro rod templates",* Presented at the UK Nitrides Consortium Summer, Sheffield, UK, 6th-7th July 2016.

Contents

List of Figures

List of Tables

Chapter 1

Introduction

This chapter provides a brief introduction on the history, current status and great challenges of III-nitride material and device research. Furthermore, the motivation and the objectives of the project performed through the thesis will be summarised. A thesis organisation is described at the end of this chapter.

1.1 The Energy Crisis and Lighting Technology

Since the Second Industrial Revolution, electricity has been playing an indispensable role in human development. In the past few decades, global electricity consumption has quadrupled from 5271 TWh to 20863 TWh. However, despite the sustained growth of renewable energy, electricity supply still heavily relies on fossil fuels such as oil, natural gas and coal, which account for 67.3% of the overall global total electricity production[1]. The dependence on fossil fuels possesses two major risks. Firstly, fossil fuels are not sustainable, as they will eventually be depleted. Secondly, global warming and climate change as a result of carbon emission mainly due to the combustion of fossil fuels are becoming increasingly worse. In 2018, the global energy-related carbon dioxide (CO_2) emissions just hit a historic high record of 33.1 Gt, leading to the five warmest years from 2014 to 2018 in a row in the last century[2,3]. The climate change has exhibited in the form of the regular appearance of extreme weather, El Niño and La Niña, heat waves and storm surges. These also lead to a reduction in water resources, fishery resources and crop yields globally[4].

Globally, lighting was one of the major sectors for electricity consumption, which once consumed 19% of total electricity[5]. This enormous consumption was largely due to inefficient lighting technology such as incandescent lamps with an efficacy of only 12 – 16 lm/W. This means only approximately 5% of energy can be converted to light, while the rest energy is wasted as heat. In the early twentieth century, the development of fluorescent lamps, followed by the development of compact fluorescent lamps (CFLs) enabled a higher luminous efficacy of 60 – 70 lm/W. However, the main concern of fluorescent lamps is the use of mercury, which is not healthy and environmentally friendly. For this reason, the fluorescent lamps, alongside with the incandescent lamp, are being gradually phased out by multiple countries through legislation, and their sales volume have been decreasing since 2010[6,7].

Solid state lighting (SSL), which are mainly based on III-nitride light-emitting diodes (LEDs), are considered as the ultimate lighting sources for general illumination. LEDs have a great potential for high efficiency, and unlike fluorescent lamps, there is no toxic element involved. White LEDs are achieved based on the development of blue LEDs, which is one of the greatest inventions leading to the winning of a Noble Prize awarded in 2014. White LEDs are fabricated predominantly through a simple combination of “blue III-nitrides LEDs + yellow phosphor” combination. For the last 20 years, LEDs have shown a steady improvement in efficacy. Current white LEDs commercially available exhibit an efficacy of above 90 lm/W, while the topmost commercialised product can reach an efficacy of 200 lm/W[8]. As of 2018, the market share of white LEDs is comparable to that of fluorescent lamps for residential lighting, while the sales of incandescent lamps have dropped to less than 5%. Owing to the high energy efficiency of LEDs, the lighting technology is on track to achieve the UN Sustainable Development Goals (SDGs) by 2030[7].

So far a number of countries have already been working on the new legislation to establish a standard for LED lighting[9]. Currently, the best efficacy of LEDs achieved in the laboratory is 303 lm/W reported by Cree, which is still distant from the theoretically predicted maximum of 370 lm/W[10,11]. On the other hand, the application of LED also expanded to various other areas, such as visible light communication (VLC) which has been purposed as a part of the solution to ease the looming “spectrum crisis”. However, one of the challenges current VLC technology is facing is due to a very limited modulation bandwidth as a result of c-plane III-nitrides which exhibit an intrinsically long carrier recombination lifetime. Therefore, there is an increasing demand to develop new technologies and further improve the performance of III-nitrides LEDs.

1.2 History and Development of III-nitrides LEDs

Holonyak and Bevacqua reported the first visible LED in 1962, where they diffused phosphorus into gallium arsenide (GaAs) to increase the bandgap and generate visible red light[12]. In 1968 and 1971, the breakthrough of using nitrogen dopant as radiative recombination centres enabled the generation of green light in GaP:N and yellow light in GaAsP:N[13,14]. By the end of the 80s, the III-V LED efficacies have been improved to 2.5 lm/W for green GaP:N LED and 10 lm/W for red AlGaAs LED[15]. However, the fundamental limitation of either GaP or AlGaAs with high Al content is due to their indirect band structure along with their bandgaps which are far from the blue spectral region. Without blue LEDs, it would be impossible to cover the full visible spectrum or combine three primary colours to create high-quality white light.

Before the arrival of GaN-based blue LED, blue LEDs were obtained by using SiC and ZnSe. However, SiC is an indirect bandgap semiconductor meaning the optical quantum efficiency is extremely low with a reported maximum of 0.03%[16]. ZnSe intrinsically exhibits dark-line defects (DLDs) that grow and propagate an active region during continuous operation at ambient temperature, hence significantly limiting the lifetime of ZnSe LEDs or laser diodes[17].

The first report of GaN was from Johnson et al. who synthesised powder GaN by flowing ammonia (NH_3) through hot liquid gallium in 1931, aiming to investigate the chemical properties of GaN[18]. Maruska and Tietjen grew the first single-crystalline GaN films for electrical and optical research in 1969[19]. They imitated the vapour-phase growth technique used for the growth of GaAs, GaP and GaSb, and successfully grew GaN on sapphire by using gallium monochloride (GaCl) as a gallium source and NH_3 as a nitrogen source. However, GaN films grew by this method are naturally n-type doped with an electron concentration of 10^{19} cm^{-3} due to a high density of nitrogen vacancies. The attempt of obtaining p-type GaN through germanium (Ge) doping also led to a poor uniformity and reproducibility. Since then, p-GaN could not have been obtained for 20 years. Due to the lack of p-GaN, research of III-nitrides LEDs was focused on metal-insulator-semiconductor (MIS) structures on the early stage[20,21]. Zinc (Zn) and magnesium

(Mg) were doped into GaN as acceptors in order to compensate electrons. Although Mg has proven to be a proper p-type dopant in later research, only semi-insulating GaN could be obtained at that time.

Besides the p-GaN issue, the quality and morphology of GaN were far from satisfactory. GaN on sapphire exhibits a high dislocation density, as there is a lattice mismatch of up to 16% between GaN and sapphire. In 1983, Yoshida et al. improved the crystal quality of GaN by using a two-step method, namely, initially coat sapphire with AlN buffer and then grow GaN on top by using reactive molecular beam (MBE)[22]. They suggested that the improvement in crystal quality was due to the reduced lattice mismatch by inserting the AlN buffer between GaN and sapphire, but no morphologic details were included in their report. In 1986, Amano et al. utilised AlN buffer in metal organic chemical vapour deposition (MOCVD) growth and achieved a GaN film with a mirror-like morphology for the first time[23]. In 1991, Nakamura further advanced the two-step method by alternatively using a low-temperature GaN buffer[24].

Another major breakthrough is due to achieving p-GaN by Amano et al. in 1989. They obtained the first conductive p-GaN by exposing an Mg-doped GaN film under low-energy electron beam irradiation (LEEBI)[25]. The results indicated that GaN:Mg films were activated by LEEBI, leading the resistivity to drop dramatically from ~10^8 Ω·cm to ~35 Ω·cm. However, the activation mechanism was unclear, and LEEBI can only activate a shallow region near the surface of a GaN:Mg film, which restricted the LED fabrication. In 1992, Nakamura et al. demonstrated that the full activation of GaN:Mg film could be achieved by using a post-growth thermal annealing process instead of LEEBI[26]. As a result, the hole concentration was increased by an order of magnitude, and the resistivity was further reduced to 2 Ω·cm. They also proposed a model to explain the mechanism behind the p-GaN activation[27]. The magnesium-hydrogen (Mg-H) neutral complexes, which was formed by Mg acceptors and atomic hydrogen dissociated from NH_3, were considered to be responsible for the hole compensation and the consequently high resistivity in untreated GaN:Mg films. LEEBI or annealing in hydrogen-free environment can break the complexes, releasing the hydrogen and thereby reenabling Mg as acceptors. This proposal was later confirmed by Neugebauer and Van de Walle in 1995 through theoretical calculation[28].

The discovery of p-GaN activation made the fabrication of a GaN p-n junction possible. In 1989, the first GaN p-n homojunction LED was demonstrated by Amano et al. in their LEEBI article[25]. However, the efficiency of the homojunction LED was very low, and the fixed wavelength further limited the application of such a LED. Therefore, a double heterojunction (DH) LED is desired. InGaN with a tunable bandgap is a good candidate for an active region in a DH based LED. In 1993, Nakamura et al. reported a blue LED using a GaN/InGaN/GaN DH structure as an active region, achieving 125 μW light output power at 440nm under 20 mA injection current, representing 0.22% external quantum efficiency (EQE)[29]. They further improved the performance of blue LEDs by introducing a thin AlGaN layer, as an electron blocking layer (EBL)[30], leading to high brightness with > 1 cd luminous intensity. The met the requirements for commercialisation, achieved by the Nichia Corporation, where Nakamura was then a chief engineer. In 1995, they reported high-brightness III-nitride based blue, green and yellow LEDs with an InGaN multiple quantum well (MQW) structure as an active region[31]. These techniques, including aforementioned AlN or GaN low-temperature nucleation layer, Mg-doped p-type GaN, EBL and QW structure, have been widely used in current III-nitride epitaxy growth and LED fabrication.

1.3 Development of Semi-polar and Non-polar III-nitrides

So far, the major achievements of III-nitride emitters are primarily based on (0001) c-plane GaN on sapphire but are mainly limited to the blue spectral region. One of such limitations is the quantum confined Stark effect (QCSE), which leads to wavelength instability, long radiative recombination lifetime, and low quantum efficiency in c-plane LEDs, especially in longer wavelength. The mechanism for the formation of QCSE is due to an internal polarisation along the (0001) orientation resulting from the asymmetrical crystal structure of III-nitrides. Therefore, the use of semi-polar and non-polar GaN instead of the polar (0001) c-plane GaN in LEDs has been proposed as a solution to eliminate or reduce the QCSE.

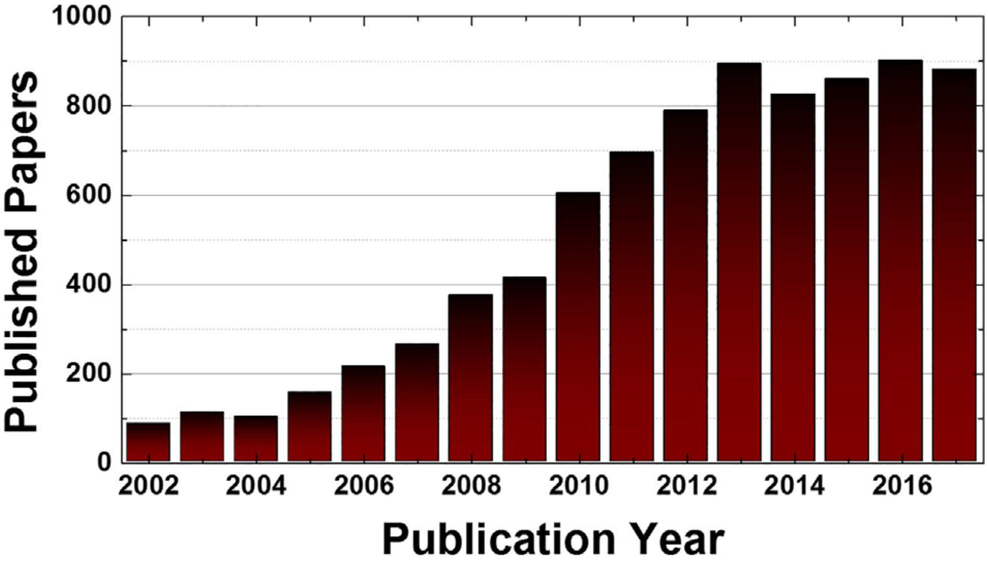

Figure 1.1. Number of publications in the semi-polar and non-polar research area each year from 2002 to 2017. Reproduced with permission[32].

The study of semi-polar and non-polar GaN can be found on the early stage of III-nitrides research, especially (11-20) a-plane non-polar GaN, due to the fact that r-plane sapphire was the cheapest and the most readily available substrate at that time[33–37]. However, all researches conducted prior to the 2000s were not targeting to achieve semi-polar or non-polar GaN on purpose, but instead were trying to find the most suitable substrate for GaN growth. The first intentional attempt of growth targeting at non-polar GaN was conducted by Waltereit et al. in 2000[38]. In their experiment, non-polar m-plane GaN was grown on a γ-$LiAlO_2$ substrate using molecular-beam epitaxy (MBE). Although a γ-$LiAlO_2$ substrate is not good for MOCVD growth due to its chemical instability and high diffusivity of Li and Al atoms at a high temperature, the AlGaN/GaN MQW structure grown on a γ-$LiAlO_2$ substrate shows zero polarisation confirming the effectiveness of non-polar orientation on the suppression of QCSE. In 2002, non-polar a-plane GaN grown on r-plane sapphire substrates using both MBE and MOCVD were reported[39,40]. Since then, the research of semi-polar and non-polar III nitrides have been gaining increasing attention, and the number of publications has been growing rapidly every year up to now (Fig. 1.1).

Due to the cost and availability issue of native GaN substrate, heteroepitaxial growth on foreign substrates mainly dominates the research of semi-polar/non-polar III-nitrides. The typical substrates for the epitaxial growth of semi-polar or non-polar GaN include non-polar (11-20) a-plane on r-plane sapphire[39,40], non-polar (1-100) m-plane on m-plane sapphire[41,42], and semi-polar (11-22) on m-plane sapphire[43,44], by using MBE[40,44], MOCVD[39,41], or hydride vapour phase epitaxy (HVPE)[42,43]. Other semi-polar planes include (1-102)[45], (10-1-3)[43,46] (10-1-1)[46], (11-26)[47] etc. Various substrates other than sapphire were also used, such as silicon (Si)[45], silicon carbide (SiC)[48–51] and less common substrates such as spinel substrates[46,52], a-plane sapphire[53], GaAs[54], graphene[55], and SiC grid on Si[56]. The use of unconventional growth technique, such as pulsed laser deposition (PLD) also enable the growth of III-nitride at ambient temperature and provides a wide range of substrate options[57–59].

However, the crystal quality of either semi-polar or non-polar GaN on foreign substrates are far from satisfactory. As a consequence, there have been very limited reports on semi-polar/non-polar III-nitrides emitters with reasonable device performance so far[40,48,51,52,60], which are hardly comparable to c-plane devices. Typically, these semi-polar or non-polar GaN on foreign substrates exhibit a high density of crystalline defects including thread dislocation (TD) with a density of ~10^{10} cm^{-2} and basal stacking fault (BSF) with a density of 10^5 cm^{-1}. Various techniques have been employed in order to reduce the defect density in the heteroepitaxial growth, including in-situ interlayer/nano-mask[61,62], semi-polar micro-facet[63–65], epitaxial lateral overgrowth (ELOG)[66–69], sidewall lateral epitaxial overgrowth (SLEO)[70], and patterned substrates[71–79]. For the growth of semi-polar or non-polar GaN on silicon substrates, patterned Si is almost essential, as a result of the lack of epitaxial relation between GaN epilayer and planar Si substrate[71–75]. Patterned silicon can be obtained by means of anisotropic chemical etching in potassium hydroxide (KOH). The growth of semi-polar or non-polar GaN on patterned sapphire substrate (PSS) is also possible but requires a careful design in terms of the inclined angle along with post-growth chemical mechanical polishing (CMP)[80]. In addition, PSS is also the only method that can achieve some artificial semi-polar planes such as (20-21) on sapphire substrate[80,81]. In ELOG and its advanced version, SLEO, silicon nitride (SiN) or silicon dioxide (SiO_2) mask is patterned into certain geometry with window region either on a sapphire substrate or an as-grown GaN template. The GaN grows out of the window regions either from the bottom or the sidewall, and eventually coalesces laterally over the mask, blocking defects that propagate vertically. The effectiveness of defect blocking depends on the choice of crystal orientation and the design of the mask. So far, there are a number of reports demonstrating that ELOG can reduce TD density by around two orders of magnitude and BSF density by about an order of magnitude[69,70].

Despite the many efforts, the effectiveness of defect blocking still largely depend on the growth orientation and the choice of approach. In most cases, the defects, especially BSF, cannot be fully blocked. These defects either propagate vertically and then penetrate through an epilayer or are regenerated at the epilayer/mask interface or are partially blocked leading to the formation of inhomogeneous defect-rich areas. As a result, semi-polar/non-polar emitters with the best performance are still grown on native free-standing semi-polar and non-polar GaN substrates. Most of these free-standing GaN substrates available with a very limited size are obtained by growing thick c-plane GaN using HVPE[82] or ammonothermal growth[83] and then slicing along a certain angle to expose the desired semi-polar or non-polar orientation. Such substrates have a TD density as low as 10^6 cm^{-2} and a very low BSF density. So far, III-nitrides emitters grown on various semi-polar and non-polar GaN substrates have been reported, including m-plane[84–88], (11-22)[89,90], (10-1-1)[91], a-plane[92], (20-21)[93,94], (30-31)[95], (30-3-1)[96] and (20-2-1)[97,98], etc. Blue, green and amber LEDs have been grown on semi-polar (11-22) GaN[89]. Non-polar m-plane LED with ~40% peak EQE has been reported[87]. In addition, laser diodes (LDs) with blue or green emission have been realised on various semi-polar and non-polar GaN substrate[86,88,90,93–95,98].

In order to address the great challenges in developing larger and cost-effective semi-polar and non-polar GaN templates with a step-change in crystal quality on foreign substrates, our group have been devoted considerable effort to developing the overgrowth of semi-polar and non-polar GaN on foreign substrates for over a decade. Previously, we have reported high-quality semi-polar (11-22) GaN overgrown on micro-rod array template on sapphire, with reduced TD density of 2×10^8 cm^{-2} and BSF density of 2.8×10^4 cm^{-1} [99]. Semi-polar (11-22) InGaN LEDs with emission wavelength ranging from blue to amber have been demonstrated[100]. We have also reported high-quality semi-polar (11-22) GaN on patterned (113) Si with x-ray rocking curve (XRC) full width half maximum (FWHM) of 511 and 580 arcsec along the c- and m- orientations, respectively[101]. Recently, we have also achieved high quality non-polar (11-20) GaN grown on sapphire through double overgrowth technique. The (11-20) GaN has a TD density of 5×10^{7} cm^{-2} and BSF density of 1×10^{4} cm^{-1}, with XRC FWHM of 226 and 313 arcsec rocking along with the [0001] and [1-100] direction[102]. The details of this work are included in Chapter 7.

1.4 Challenges in III-nitrides

Tremendous development has been made in the past 30 years, but the major success is still limited to conventional c-plane III-nitrides. Semi-polar and non-polar GaN are expected to exhibit superior performance to c-plane GaN, but suffer from severe crystal quality issues, implying that there is still a long way to go before commercialisation. In this section, the main issues and major challenges that are hampering the development of both c-plane and semi-polar/non-polar III-nitride emitters are discussed.

1.4.1 Quantum Confined Stark Effect

As briefly mentioned in the last section, the QCSE has a strong impact on the performance of c-plane emitters. In the wurtzite structure GaN, strong spontaneous and piezoelectric polarisations exist due to the lack of inversion symmetry. As a result, a polarisation induced electric field is generated parallel to the c-axis. Such electric fields significantly reduce the overlap of electron-hole wavefunctions in QWs. This phenomenon is called the QCSE.

As a result of QCSE, a red-shift in emission wavelength is generated in comparison with a polarisation-free case. Such a red-shift can be screened out by injected carriers with increasing of injection current, leading to a blue-shift and thus a wavelength instability issue. Additionally, the reduced overlap of electron-hole wavefunction increases the radiative recombination lifetime, limiting the modulation speed when using c-plane emitters for VLC. Similarly, the reduced overlap also leads to a reduction in radiative recombination probability, which decreases internal quantum efficiency (IQE). The QCSE also restricts the use of thick QW and high In composition in InGaN QW structure. However, the thicker QW is an effective technique to reduce efficiency droop, and higher In composition is vital for achieving longer wavelength.

1.4.2 Substrates

The greatest challenge for III-nitrides is due to substrates. Unlike Si and GaAs, it is impossible to pull single crystal GaN boule direct from the melt using matured crystallisation technologies such as Czochralski or Bridgman method, due to the requirement of an extremely high decomposition pressure and melting point of GaN[103]. As a result, foreign substrates such as SiC, Si and sapphire are more commonly used in III-nitrides research and commercial product.

Among all the foreign substrates, SiC substrate has the smallest lattice mismatch with GaN and AlN, which are only 3.5% and 1% respectively[104]. Because of the reduced lattice mismatch, SiC is expected to produce epitaxy layers with much lower defect density. In addition to the small lattice match, SiC has good thermal stability and high thermal conductivity which could benefit both epitaxial growth and LED design. Currently, common SiC substrate is available in two hexagonal polytypes, 4H-SiC and 6H-SiC. Both types of SiC substrate have different stacking sequences from that of GaN, which can potentially generate stacking faults that penetrate throughout the whole epilayer once GaN is grown on it. The stacking order matched polytype, 2H-SiC, however, is not commercially available yet. Similar to GaN, due to the extremely high temperature and pressure requirement, SiC cannot be grown by conventional crystal pulling. Instead, most SiC substrates are produced by physical vapour transport (PVT)[104]. This method limited the length of the grown boule and led to a fairly high price of SiC substrates.

Silicon is widely used in integrated circuits. Since the silicon industry is well-developed, silicon substrates are available in large size of up to 18-inch. However, there are still several challenges in growing GaN on Si[105]. The lattice mismatch between GaN and silicon is as large as 17%, which leads to a high density of dislocations. The thermal expansion coefficient of silicon is 54% smaller than GaN, not only leading to seriously bowing and cracking, but also hindering employment of conventional dislocation reduction methods, which normally require thick GaN layer for silicon substrate. The contact of gallium and silicon at a high-temperature results in “meting back reaction” seriously damaging the surface of the substrate and epilayers.

Sapphire is the most common foreign substrate for III-nitride semiconductor due to its hexagonal symmetry, stable thermal stability under epitaxial growth condition, relatively close thermal expansion coefficient match, and availability. R-plane sapphire is typically used for the growth of a-plane non-polar GaN discussed in this thesis. The lattice mismatches along the m-direction and c-direction are 16% and 1%, respectively[106]. Such large lattice mismatches generate a high dislocation density in epilayers, which must be reduced in order to obtain satisfying device performance.

1.4.3 Crystal Quality and Morphology

Due to the lack of native substrates, the growth of GaN on foreign substrates remains the primary approach, leading to a high density of defects in III-nitrides epilayers. For example, GaN grown on sapphire exhibits a high density of TD with an order of 10^9 - 10^{10} cm^{-2}. The case for silicon substrate is even worse, as it has a larger difference in thermal expansion coefficient and melting back issue. As for the semi-polar and non-polar, the quality is far below c-plane GaN, and there is an additional BSF issue that has to be taken into account. TDs serve as nonradiative recombination centres which lower the optical performance, while BSF acts as a cubic QW-like structure. TDs have also been found to be related to the generation of pyramidal hillocks on the surface of semi-polar and non-polar GaN, which limit the fabrication of device and device performance.

1.4.4 Efficiency Droop

Efficiency droop has been widely observed in III-nitride LEDs[107]. As shown in Fig. 1.2, the efficiency of a LED increases initially at low current density (typically below 10 A/cm^2) with increasing injection current density, and then quickly decreases with further increasing injection current density. A number of models have been proposed to explain the mechanism of efficiency droop, including Auger recombination[108], electron leakage[109], density activated defect recombination

(DADR)[110], delocalisation of carriers[111], current crowding[112], and loss of current injection efficiency.[113] Although both Auger recombination and electron leakage are considered more likely to be the cause, there is still no leading consensus was reached.

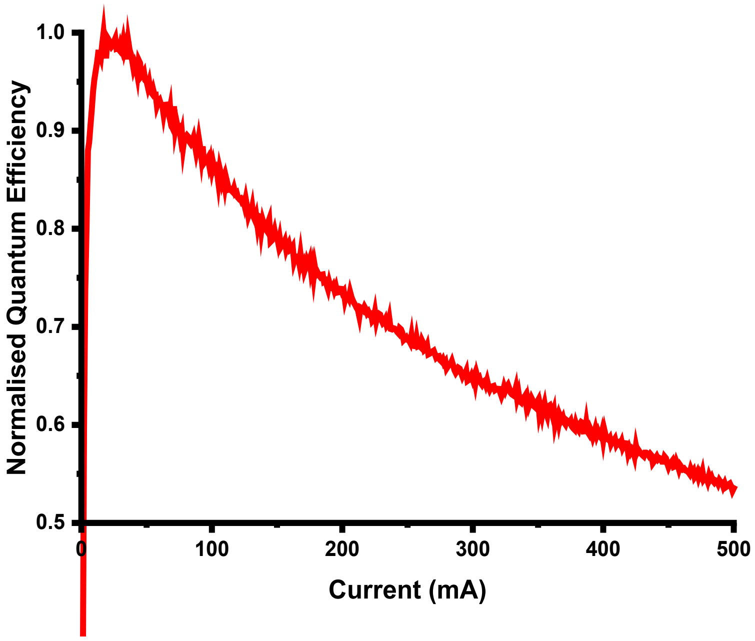

Figure 1.2. Normalised quantum efficiency of a commercial blue InGaN LED as a function of injection current. The efficiency is only 54% of the peak efficiency at 500 mA operating current. The data was measured using Labsphere LCS-100 integrating sapphire.

1.5 Motivation and Aims

Despite the success of III-nitride LED general illumination, there is still strong demand for III-nitride LED with higher luminous efficacy and optical performance. Additionally, new applications, such as VLC, also raise new requirements, such as modulation speed. To tackle these issues, the growth of III-nitrides along semi-polar or non-polar orientation was proposed as a potential solution. However, heteroepitaxially grown semi-polar and non-polar III-nitrides usually contains a high density of defects, and homoepitaxial free-standing GaN substrate is not a preferred option due to its high price, limited size and poor availability. Therefore, considerable effort will have to be devoted to improving the crystal quality of semi-polar and non-polar GaN grown on foreign substrates.

The aim of the research presented in this PhD thesis is to achieve high quality non-polar (11-20) GaN on r-plane sapphire through overgrowth on regularly arrayed micro-rod templates, and further advance the development of non-polar InGaN-based LED.

Four topics are focused in this work:

- The anisotropic strain within the non-polar (11-20) GaN grown on regularly arrayed micro-rod template has been investigated, demonstrating the major advantage of our overgrowth methods and also further contributing to the understanding of growth and relaxation mechanism.
- A novel monolithic multiple-facet MQW structure has been demonstrated by the growth on our novel patterned non-polar GaN templates, demonstrating a great potential to achieve phosphor-free non-polar white LEDs.
- Non-polar InGaN-based LEDs have been grown on our high-quality non-polar GaN templates, and optical properties in particular polarisation properties have been studied.
- Non-polar (11-20) GaN with further improved high quality has been achieved by means of developing a double overgrowth technique.

The detail of the above topics can be found from Chapter 4 to Chapter 7.

Reference

1. IEA International Energy Agency. *Electricity Information 2018: Overview. OECD* (2018).

2. IEA International Energy Agency. *Global Energy and CO2 Status Report 2018*. (2019).

3. NOAA National Centers for Environmental Information. State of the Climate: Global Climate Report for Annual 2018. (2019). Available at: https://www.ncdc.noaa.gov/sotc/global/201813. (Accessed: 5th April 2019)

4. IPCC Intergovernmental Panel on Climate Change. *Climate Change 2014: Impacts, Adaptation, and Vulnerability. Part A: Global and Sectoral Aspects. Contribution of Working Group II to the Fifth Assessment Report of the Intergovernmental Panel on Climate Change*. (2014).

5. Waide, P. & Tanishima, S. *Light's labour's lost: policies for energy-efficient lighting*. (OECD Publishing, 2016).

6. Waide, P. Phase out of incandescent lamps. *Environment* (2010). doi:10.1787/5kmh3nhp62s0-en

7. IEA International Energy Agency. Lighting - Tracking Clean Energy Progress. (2019). Available at: https://www.iea.org/tcep/buildings/lighting/. (Accessed: 5th April 2019)

8. Philips. Dubai Municipality and Philips Lighting announce launch of Dubai Lamp Initiative. (2016). Available at: http://www.newsroom.lighting.philips.com/news/2016/20161005-dubai-municipality-and-philips-lighting-announce-launch-of-dubai-lamp-initiative#. (Accessed: 5th April 2019)

9. Luminaires, P. Draft Minimum Energy Performance Standards for LED Lighting. (2016). Available at: http://www.energyrating.gov.au/document/led-meps-draft-28-july-2016.

10. Cree Inc. Cree First to Break 300 Lumens-Per-Watt Barrier. (2014). Available at: https://www.cree.com/news-media/news/article/cree-first-to-break-300-lumens-per-watt-barrier. (Accessed: 5th April 2019)

11. Murphy, T. W. Maximum spectral luminous efficacy of white light. *J. Appl. Phys.* **111**, (2012).

12. Holonyak Jr, N., Bevacqua, S. F., Holonyak, N. & Bevacqua, S. F. Coherent (visible) light emission from Ga (As1− x P x) junctions. *Appl. Phys. Lett.* **1**, 82–83 (1962).

13. Logan, R. A., White, H. G. & Wiegmann, W. Efficient green electroluminescence in nitrogen-doped gap p-n junctions. *Appl. Phys. Lett.* **13**, 139–141 (1968).

14. Groves, W. O., Herzog, A. H. & Craford, M. G. The Effect of Nitrogen Doping on GaAs1−xPx Electroluminescent Diodes. *Appl. Phys. Lett.* **19**, 184–186 (1971).

15. Craford, M. G. LEDs_Challenge_the_Incandescents_Craford.pdf. 24–29 (1992).

16. Yuan, C. A., Han, C. N., Liu, H. M. & van Driel, W. D. Solid-State Lighting Technology in a Nutshell. in *Solid State Lighting Reliability: Components to Systems* (eds. van Driel, W. D. & Fan, X. J.) 13–41 (Springer New York, 2013). doi:10.1007/978-1-4614-3067-4_2

17. Guha, S., Depuydt, J. M., Haase, M. A., Qiu, J. & Cheng, H. Degradation of II-VI based blue-green light emitters. *Appl. Phys. Lett.* **63**, 3107–3109 (1993).

18. Johnson, W. C., Parson, J. B. & Crew, M. C. Nitrogen Compounds of Gallium. III. *J. Phys. Chem.* **36**, 2651–2654 (1931).

19. Maruska, H. P. & Tietjen, J. J. The preparation and properties of vapor-deposited single-crystal-line GaN. *Appl. Phys. Lett.* **15**, 327–329 (1969).

20. Pankove, J. I., Miller, E. A. & Berkeyheiser, J. E. GaN electroluminescent diodes. in *1971 International Electron Devices Meeting* 78–78 (IRE, 1971). doi:10.1109/IEDM.1971.188400

21. Maruska, H. P., Stevenson, D. A. & Pankove, J. I. Violet luminescence of Mg-doped GaN. *Appl. Phys. Lett.* **22**, 303–305 (1973).

22. Yoshida, S., Misawa, S. & Gonda, S. Improvements on the electrical and luminescent properties of reactive molecular beam epitaxially grown GaN films by using AlN-coated sapphire substrates. *Appl. Phys. Lett.* **42**, 427–429 (1983).

23. Amano, H., Sawaki, N., Akasaki, I. & Toyoda, Y. Metalorganic vapor phase epitaxial growth of a high quality GaN film using an AlN buffer layer. *Appl. Phys. Lett.* **48**, 353–355 (1986).

24. Shuji, N. GaN Growth Using GaN Buffer Layer. *Jpn. J. Appl. Phys.* **30**, L1705 (1991).

25. Amano, H., Kito, M., Hiramatsu, K. & Akasaki, I. P-type conduction in Mg-doped GaN treated with LEEBI. *Jpn. J. Appl. Phys.* **28**, 2112–2114 (1989).

26. Nakamura, S., Mukai, T. & Senoh, M. Thermal Annealing Effects on P-Type Mg-Doped GaN Films Japanese Journal of Applied Physics. **139**, (1992).

27. Nakamura, S., Iwasa, N., Senoh, M. & Mukai, T. Hole Compensation Mechanism of P-Type GaN Films. *Jpn. J. Appl. Phys.* **31**, 1258–1266 (1992).

28. Neugebauer, J. & Van de Walle, C. G. Hydrogen in GaN: Novel Aspects of a Common Impurity. *Phys. Rev. Lett.* **75**, 4452–4455 (1995).

29. Nakamura, S., Senoh, M. & Mukai, T. P-GaN/N-InGaN/N-GaN Double-Heterostructure Blue-Light-Emitting Diodes. *Jpn. J. Appl. Phys.* **32**, L8–L11 (1993).

30. Nakamura, S., Mukai, T. & Senoh, M. Candela-class high-brightness InGaN/AlGaN double-heterostructure blue-light-emitting diodes. *Appl. Phys. Lett.* **64**, 1687–1689 (1994).

31. Nakamura, S., Senoh, M., Iwasa, N. & Nagahama, S. High-Brightness InGaN Blue, Green and Yellow Light-Emitting Diodes with Quantum Well Structures. *Jpn. J. Appl. Phys.* **34**, L797–L799 (1995).

32. Monavarian, M., Rashidi, A. & Feezell, D. A Decade of Nonpolar and Semipolar III-Nitrides: A Review of Successes and Challenges. *Phys. Status Solidi Appl. Mater. Sci.* **216**, 1–22 (2019).

33. Maruska, H. P., Anderson, L. J. & Stevenson, D. A. Microstructural Observations on Gallium Nitride Light-Emitting Diodes. *J. Electrochem. Soc.* **121**, 1202 (1974).

34. Madar, R., Michel, D., Jacob, G. & Boulou, M. Growth anisotropy in the GaN/Al2O3 system. *J. Cryst. Growth* **40**, 239–252 (1977).

35. Sasaki, T. & Zembutsu, S. Substrate-orientation dependence of GaN single-crystal films grown by metalorganic vapor-phase epitaxy. *J. Appl. Phys.* **61**, 2533–2540 (1987).

36. Lei, T., Ludwig, K. F. & Moustakas, T. D. Heteroepitaxy, polymorphism, and faulting in GaN thin films on silicon and sapphire substrates. *J. Appl. Phys.* **74**, 4430–4437 (1993).

37. Melton, W. A. & Pankove, J. I. GaN growth on sapphire. *J. Cryst. Growth* **178**, 168–173 (1997).

38. Waltereit, P. *et al.* Nitride semiconductors free of electrostatic fields for White LEDs. *Lett. to Nat.* **406**, 865–868 (2000).

39. Craven, M. D., Lim, S. H., Wu, F., Speck, J. S. & Denbaars, S. P. Structural characterization of nonpolar $(11\bar{2}0)$ a-plane GaN thin films grown on $(1\bar{1}02)$ r-plane sapphire. *Appl. Phys. Lett.* **81**, 469–471 (2002).

40. Ng, H. M. Molecular-beam epitaxy of GaN/AlxGa1-xN multiple quantum wells on R-plane $(10\bar{1}2)$ sapphire substrates. *Appl. Phys. Lett.* **80**, 4369–4371 (2002).

41. Armitage, R. & Hirayama, H. M -plane GaN grown on m -sapphire by metalorganic vapor phase epitaxy. *Appl. Phys. Lett.* **92**, 90–93 (2008).

42. Zhu, T., Martin, D. & Grandjean, N. M-plane GaN grown on m-plane sapphire

by hydride vapor phase epitaxy. *Jpn. J. Appl. Phys.* **48**, 22–25 (2009).

43. Baker, T. J., Haskell, B. A., Wu, F., Speck, J. S. & Nakamura, S. Characterization of Planar Semipolar Gallium Nitride Films on Sapphire Substrates. *Jpn. J. Appl. Phys.* **45**, L154–L157 (2006).

44. Lahourcade, L., Bellet-Amalric, E., Monroy, E., Chauvat, M. P. & Ruterana, P. Molecular beam epitaxy of semipolar AlN(1122) and GaN(1122) on m-sapphire. *J. Mater. Sci. Mater. Electron.* **19**, 805–809 (2008).

45. Schulze, F., Dadgar, A., Bläsing, J. & Krost, A. Influence of buffer layers on metalorganic vapor phase epitaxy grown GaN on Si(001). *Appl. Phys. Lett.* **84**, 4747–4749 (2004).

46. Baker, T. J. *et al.* Characterization of Planar Semipolar Gallium Nitride Films on Spinel Substrates. *Jpn. J. Appl. Phys.* **44**, L920–L922 (2005).

47. Zhou, L., Chandrasekaran, R., Moustakas, T. D. & Smith, D. J. Structural characterization of non-polar (1 1 2 0) and semi-polar (1 1 2 6) GaN films grown on r-plane sapphire. *J. Cryst. Growth* **310**, 2981–2986 (2008).

48. Craven, M. D., Waltereit, P., Wu, F., Speck, J. S. & DenBaars, S. P. Characterization of a-plane GaN/(Al,Ga)N multiple quantum wells grown via metalorganic chemical vapor deposition. *Japanese J. Appl. Physics, Part 2 Lett.* **42**, (2003).

49. Craven, M. D. *et al.* Microstructural evolution of a -plane GaN grown on a -plane SiC by metalorganic chemical vapor deposition . *Appl. Phys. Lett.* **84**, 1281–1283 (2004).

50. Zakharov, D. N. *et al.* Structural TEM study of nonpolar a-plane gallium nitride grown on $(11\bar{2}0)$4H-SiC by organometallic vapor phase epitaxy. *Physical Review B - Condensed Matter and Materials Physics* **71**, (2005).

51. Gardner, N. F., Kim, J. C., Wierer, J. J., Shen, Y. C. & Krames, M. R. Polarization anisotropy in the electroluminescence of m-plane InGaN-GaN multiple-quantum-well light-emitting diodes. *Appl. Phys. Lett.* **86**, 1–3

(2005).

52. Chakraborty, A. *et al.* Milliwatt power blue InGaN/GaN light-emitting diodes on semipolar GaN templates. *Japanese J. Appl. Physics, Part 2 Lett.* **44**, (2005).

53. Paskova, T. *et al.* Growth of GaN on a-plane sapphire: In-plane epitaxial relationships and lattice parameters. *Phys. Status Solidi Basic Res.* **240**, 318–321 (2003).

54. Murakami, H. *et al.* Growth of semi-polar InN layer on GaAs (1 1 0) surface by MOVPE. *J. Cryst. Growth* **318**, 479–482 (2011).

55. Gupta, P. *et al.* MOVPE growth of semipolar III-nitride semiconductors on CVD graphene. *J. Cryst. Growth* **372**, 105–108 (2013).

56. Dinh, D. V. *et al.* Semipolar (202¯3) nitrides grown on 3C-SiC/(001) Si substrates. *Semicond. Sci. Technol.* **30**, 0–8 (2015).

57. Kobayashi, A., Kawano, S., Kawaguchi, Y., Ohta, J. & Fujioka, H. Room temperature epitaxial growth of m -plane GaN on lattice-matched ZnO substrates. *Appl. Phys. Lett.* **90**, 1–4 (2007).

58. Ueno, K. *et al.* Room temperature growth of semipolar AlN $(1\bar{1}02)$ films on ZnO $(1\bar{1}02)$ substrates by pulsed laser deposition. *Phys. Status Solidi - Rapid Res. Lett.* **3**, 58–60 (2009).

59. Fujii, T., Kobayashi, A., Ohta, J., Oshima, M. & Fujioka, H. Structural characteristics of semipolar InN (112l) films grown on yttria stabilized zirconia substrates. *Phys. Status Solidi Appl. Mater. Sci.* **207**, 2269–2271 (2010).

60. Liu, B. *et al.* Nonpolar m-plane thin film GaN and InGaN/GaN light-emitting diodes on LiAl O2 (100) substrates. *Appl. Phys. Lett.* **91**, 1–4 (2007).

61. Tavernier, P. R., Imer, B., DenBaars, S. P. & Clarke, D. R. Growth of thick $(11\bar{2}0)$ GaN using a metal interlayer. *Appl. Phys. Lett.* **85**, 4630–4632 (2004).

62. Chakraborty, A. *et al.* Defect reduction in nonpolar a-plane GaN films using in situ SiN x nanomask. *Appl. Phys. Lett.* **89**, 3–6 (2006).

63. Nishizuka, K. *et al.* Efficient radiative recombination from «$11\bar{2}2$» -oriented InxGa1-xN multiple quantum wells fabricated by the regrowth technique. *Appl. Phys. Lett.* **85**, 3122–3124 (2004).

64. Wunderer, T. *et al.* Bright semipolar GaInN/GaN blue light emitting diode on side facets of selectively grown GaN stripes. *Appl. Phys. Lett.* **89**, (2006).

65. Yang, J., Yang, F., Kent, T. F., Mills, M. J. & Myers, R. C. Semipolar InN/AlN multiple quantum wells on {10 1¯5} faceted AlN on silicon. *Appl. Phys. Lett.* **103**, (2013).

66. Haskell, B. A. *et al.* Defect reduction in ($11\bar{2}0$) a-plane gallium nitride via lateral epitaxial overgrowth by hydride vapor-phase epitaxy. *Appl. Phys. Lett.* **83**, 644–646 (2003).

67. Chakraborty, A. *et al.* Nonpolar InGaN/GaN emitters on reduced-defect lateral epitaxially overgrown a-plane GaN with drive-current-independent electroluminescence emission peak. *Appl. Phys. Lett.* **85**, 5143–5145 (2004).

68. Haskell, B. A. *et al.* Defect reduction in ($1\bar{1}00$) m-plane gallium nitride via lateral epitaxial overgrowth by hydride vapor phase epitaxy. *Appl. Phys. Lett.* **86**, 1–3 (2005).

69. Ni, X. *et al.* Defect reduction in (11 2-0) a -plane GaN by two-stage epitaxial lateral overgrowth. *Appl. Phys. Lett.* **89**, 1–4 (2006).

70. Imer, B. M., Wu, F., Denbaars, S. P. & Speck, J. S. Improved quality ($11\bar{2}0$) a-plane GaN with sidewall lateral epitaxial overgrowth. *Appl. Phys. Lett.* **88**, 2004–2007 (2006).

71. Tanikawa, T. *et al.* Growth of non-polar ($1\,1\,\bar{2}\,0$)GaN on a patterned (1 1 0)Si substrate by selective MOVPE. *J. Cryst. Growth* **310**, 4999–5002 (2008).

72. Sawaki, N. *et al.* Growth and properties of semi-polar GaN on a patterned

silicon substrate. *J. Cryst. Growth* **311**, 2867–2874 (2009).

73. Suzuki, N. *et al.* HVPE growth of semi-polar (112̄2)GaN on GaN template (113)Si substrate. *J. Cryst. Growth* **311**, 2875–2878 (2009).

74. Ni, X. *et al.* Nonpolar m -plane GaN on patterned Si(112) substrates by metalorganic chemical vapor deposition. *Appl. Phys. Lett.* **95**, (2009).

75. Khoury, M. *et al.* Growth of semipolar (202̄1) GaN layers on patterned silicon (114) 1° off by Metal Organic Vapor Phase Epitaxy. *J. Cryst. Growth* **419**, 88–93 (2015).

76. Okada, N., Kurisu, A., Murakami, K. & Tadatomo, K. Growth of semipolar (112̄2) GaN layer by controlling anisotropic growth rates in r-plane patterned sapphire substrate. *Appl. Phys. Express* **2**, (2009).

77. Schwaiger, S. *et al.* Planar semipolar (10 1̄1) GaN on (11 2̄3) sapphire. *Appl. Phys. Lett.* **96**, 1–4 (2010).

78. Hsieh, C.-Y. *et al.* Semipolar GaN Films on Prism Stripe Patterned a -Plane Sapphire Substrates . *ECS J. Solid State Sci. Technol.* **1**, R54–R56 (2012).

79. Okada, N. & Tadatomo, K. Characterization and growth mechanism of nonpolar and semipolar GaN layers grown on patterned sapphire substrates. *Semicond. Sci. Technol.* **27**, (2012).

80. Leung, B., Wang, D., Kuo, Y. S. & Han, J. Complete orientational access for semipolar GaN devices on sapphire. *Phys. Status Solidi Basic Res.* **253**, 23–35 (2016).

81. Meisch, T., Alimoradi-Jazi, M., Klein, M. & Scholz, F. (20-21) MOVPE and HVPE GaN grown on 2" patterned sapphire substrates. *Phys. Status Solidi Curr. Top. Solid State Phys.* **11**, 537–540 (2014).

82. Fujito, K. *et al.* Bulk GaN crystals grown by HVPE. *J. Cryst. Growth* **311**, 3011–3014 (2009).

83. Zajac, M. *et al.* Basic ammonothermal growth of Gallium Nitride – State of

the art, challenges, perspectives. *Prog. Cryst. Growth Charact. Mater.* **64**, 63–74 (2018).

84. Chakraborty, A. *et al.* Demonstration of nonpolar m-plane InGaN/GaN light-emitting diodes on free-standing m-plane GaN substrates. *Japanese J. Appl. Physics, Part 2 Lett.* **44**, 118–121 (2005).

85. Schmidt, M. C. *et al.* High power and high external efficiency m-plane InGaN light emitting diodes. *Japanese J. Appl. Physics, Part 2 Lett.* **46**, 2–5 (2007).

86. Schmidt, M. C. *et al.* Demonstration of nonpolar m-plane InGaN/GaN laser diodes. *Japanese J. Appl. Physics, Part 2 Lett.* **46**, 4–6 (2007).

87. Kim, K. C. *et al.* Improved electroluminescence on nonpolar m-plane InGaN/GaN quantum wells LEDs. *Phys. Status Solidi - Rapid Res. Lett.* **1**, 125–127 (2007).

88. Okamoto, K., Tanaka, T. & Kubota, M. High-efficiency continuous-wave operation of blue-green laser diodes based on nonpolar m-plane gallium nitride. *Appl. Phys. Express* **1**, 0722011–0722013 (2008).

89. Funato, M. *et al.* Blue, green, and amber InGaN/GaN light-emitting diodes on semipolar {1122} GaN bulk substrates. *Japanese J. Appl. Physics, Part 2 Lett.* **45**, 0–4 (2006).

90. Asamizu, H. *et al.* Demonstration of 426 nm InGaN/GaN laser diodes fabricated on free-standing semipolar $(11\bar{2}2)$ gallium nitride substrates. *Appl. Phys. Express* **1**, 0911021–0911023 (2008).

91. Tyagi, A. *et al.* JJAP Express Letter High Brightness Violet InGaN / GaN Light Emitting Diodes Þ Bulk GaN Substrates on Semipolar ð10 1. **46**, 129–131 (2007).

92. Liu, J. P. *et al.* Blue light emitting diodes grown on freestanding (11-20) a - plane GaN substrates. *Appl. Phys. Lett.* **92**, (2008).

93. Enya, Y. *et al.* 531 nm Green lasing of InGaN based laser diodes on semi-

polar {20$\bar{2}$1} free-standing GaN substrates. *Appl. Phys. Express* **2**, (2009).

94. Yoshizumi, Y. *et al.* Continuous-wave operation of 520 nm green InGaN-based laser diodes on semi-polar {20$\bar{2}$1} GaN substrates. *Appl. Phys. Express* **2**, 23–26 (2009).

95. Hsu, P. S. *et al.* InGaN/GaN blue laser diode grown on semipolar (30$\bar{3}$1) free-standing GaN substrates. *Appl. Phys. Express* **3**, 4–7 (2010).

96. Koslow, I. L. *et al.* High power and high efficiency blue InGaN light emitting diodes on free-standing semipolar (30$\bar{3}$1) bulk GaN substrate. *Jpn. J. Appl. Phys.* **49**, 0–3 (2010).

97. Zhao, Y. *et al.* High optical polarization ratio from semipolar (2021) blue-green InGaN/GaN light-emitting diodes. *Appl. Phys. Lett.* **99**, (2011).

98. Huang, C. Y. *et al.* Demonstration of 505 nm laser diodes using wavelength-stable semipolar (20 2$\bar{1}$) InGaN/GaN quantum wells. *Appl. Phys. Lett.* **99**, (2011).

99. Zhang, Y. *et al.* Microstructure investigation of semi-polar (11-22) GaN overgrown on differently designed micro-rod array templates. *Appl. Phys. Lett.* **109**, 241906 (2016).

100. Bai, J. *et al.* (11-22) semipolar InGaN emitters from green to amber on overgrown GaN on micro-rod templates. *Appl. Phys. Lett.* **107**, 261103 (2015).

101. Cai, Y. *et al.* Overgrowth and characterization of (11-22) semi-polar GaN on (113) silicon with a two-step method. *Semicond. Sci. Technol.* **34**, 045012 (2019).

102. Bai, J., Jiu, L., Gong, Y. & Wang, T. Non-polar (11-20) GaN grown on sapphire with double overgrowth on micro-rod/stripe templates. *Semicond. Sci. Technol.* **33**, 125023 (2018).

103. Bockowski, M. Review: Bulk growth of gallium nitride: challenges and difficulties. *Cryst. Res. Technol.* **42**, 1162–1175 (2007).

104. POWELL, A. *et al.* GROWTH OF SiC SUBSTRATES. *Int. J. High Speed Electron. Syst.* **16**, 751–777 (2006).

105. Zhu, D., Wallis, D. J. & Humphreys, C. J. Prospects of III-nitride optoelectronics grown on Si. *Reports Prog. Phys.* **76**, (2013).

106. Jiu, L., Gong, Y. & Wang, T. Overgrowth and strain investigation of (11-20) non-polar GaN on patterned templates on sapphire. *Sci. Rep.* **8**, 1–8 (2018).

107. Cho, J., Schubert, E. F. & Kim, J. K. Efficiency droop in light-emitting diodes: Challenges and counter measures. *Laser Photonics Rev.* **7**, 408–421 (2013).

108. Iveland, J., Martinelli, L., Peretti, J., Speck, J. S. & Weisbuch, C. Direct measurement of auger electrons emitted from a semiconductor light-emitting diode under electrical injection: Identification of the dominant mechanism for efficiency droop. *Phys. Rev. Lett.* **110**, 2–6 (2013).

109. Meyaard, D. S. *et al.* Identifying the cause of the efficiency droop in GaInN light-emitting diodes by correlating the onset of high injection with the onset of the efficiency droop. *Appl. Phys. Lett.* **102**, 1–4 (2013).

110. Hader, J., Moloney, J. V. & Koch, S. W. Density-activated defect recombination as a possible explanation for the efficiency droop in GaN-based light emitters. *2011 Conf. Lasers Electro-Optics Eur. 12th Eur. Quantum Electron. Conf. CLEO Eur. 2011* 1–3 (2011). doi:10.1109/CLEOE.2011.5942578

111. Yi, Y., Xian An, C. & Chunhui, Y. Investigation of the nonthermal mechanism of efficiency rolloff in InGaN light-emitting diodes. *IEEE Trans. Electron Devices* **55**, 1771–1775 (2008).

112. Kudryk, Y. Y. & Zinovchuk, A. V. Efficiency droop in InGaN/GaN multiple quantum well light-emitting diodes with nonuniform current spreading. *Semicond. Sci. Technol.* **26**, (2011).

113. Wang, L. *et al.* Influence of carrier screening and band filling effects on efficiency droop of InGaN light emitting diodes. *Opt. Express* **19**, 14182 (2011).

Chapter 2

Background

2.1 Semiconductors

Solid state materials can be classified into three groups, which are insulators, semiconductors, and conductors. For an insulator, there are few free electrons within the material, and thus the conductivity is very low on an order of $10^{-18} – 10^{-8}$ S/cm [1]. For a conductor, such as metal, there are a large number of free electrons, and hence the conductivity is very high, typically around $10^4 – 10^6$ S/cm [1]. Semiconductors have conductivities lie between insulators and conductors.

2.1.1 Band Structure

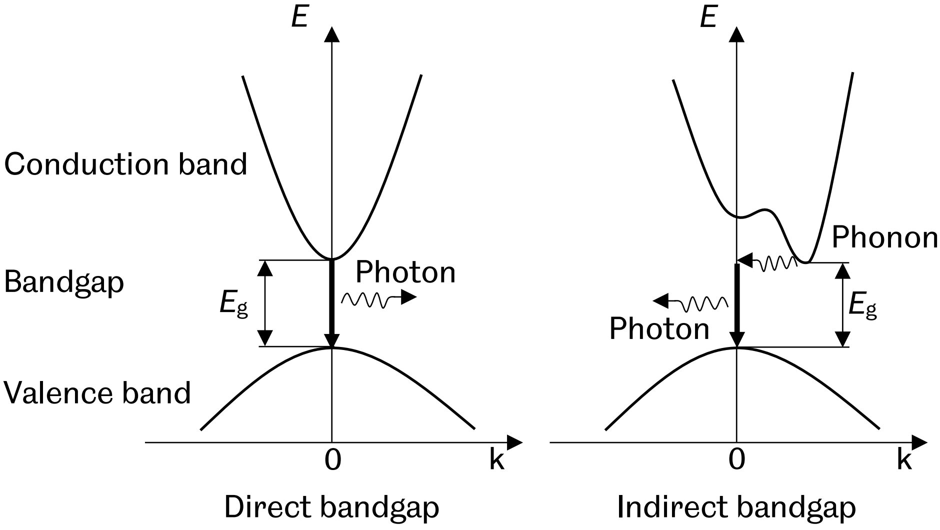

Figure 2.1. Schematic band diagram of direct bandgap and indirect bandgap.

In a semiconductor, a number of discrete energy levels are formed due to its periodic structure, allowing electrons to exist, while the energy gaps between them do not allow electrons to exist. Conduction and valence band are the two highest energy levels allowing electrons to occupy. The energy gap between them is the so-called “forbidden gap”, which is called a bandgap.

There are two types of band structure in semiconductors: direct bandgap and indirect bandgap (Fig. 2.1). In a direct bandgap semiconductor, the valence band maximum and the conduction band minimum have the same crystal momentum (k-vector). Therefore, the transition of electrons between the valence band and the conduction band is straightforward. In an indirect bandgap semiconductor, however, the conduction band minimum occurs with a different value of k. Therefore, the transition of electrons between the valence band and the conduction band requires the involvement of an additional particle in order to maintain the momentum conservation, leading to a significantly reduced probability of the radiative recombination of electrons and holes. In this case, phonons are involved in the processes, making the indirect bandgap material less attractive for the fabrication of emitters.

2.1.2 Doping

The electrical properties of a semiconductor can be adjusted by means of adding impurities and thus generating additional free electrons or holes. This intentional introduction of impurities is called doping. Depending on the element, a dopant can either be p-type (acceptor) or n-type (donor). Take III-nitride materials as an example, if a small amount of group II element such as magnesium (Mg) is doped into gallium nitride (GaN), Mg atoms will replace gallium (Ga) atoms. Valence electrons will be taken, leaving vacancies in the valence band. The Mg-doped GaN then becomes p-type semiconductor and is dominated by free holes. Similarly, if a small amount of group IV element such as silicon (Si) is doped into GaN, Si atoms can replace Ga atoms, donating additional valence electrons. The Si-doped GaN then becomes n-type semiconductor and is dominated by free electrons.

2.1.3 Recombination

The excitation of an electron from a valence band to a conduction band is always accompanied by the generation of a hole in the valence band, and thus creates an electron-hole pair (EHP). When the excited electron returns to the valence band, the annihilation of an EHP happens correspondingly, which is known as recombination. Recombination can take place through a variety of mechanisms, but there are three main types of recombination:

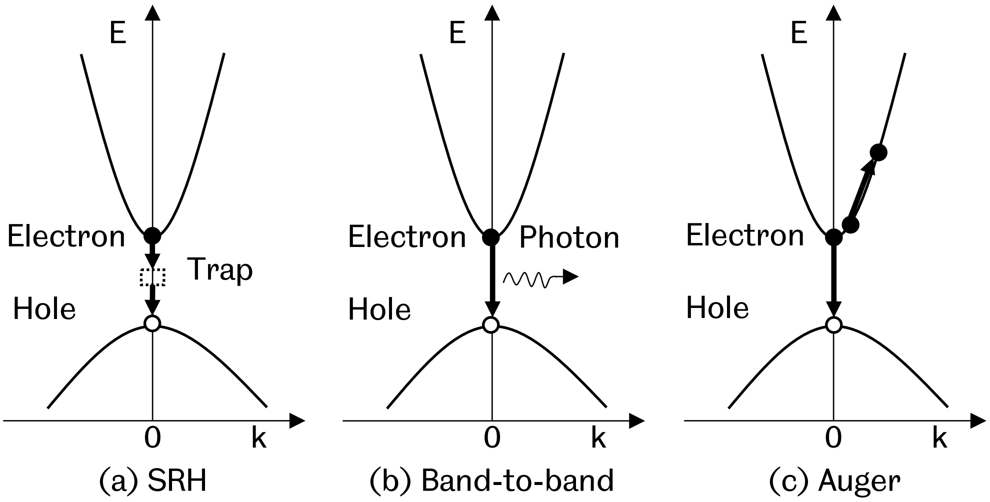

(a) SRH (b) Band-to-band (c) Auger

Figure 2.2. Three types of the recombination process. (a) SRH recombination, (b) band-to-band recombination and (c) Auger recombination.

Shockley-Read-Hall (SRH) recombination[2,3] is shown in Fig. 2.2a. This type of recombination occurs as a non-radiative recombination via electrons trapped by defects. These traps introduce a range of energy levels, which allows electrons to drop back to the valence band step-by-step. The energy required for each transition is relatively small, and therefore the process involves multiple phonons instead of a photon. The recombination rate of SRH recombination depends on carrier concentration and trap density, which can be simplified and described by:

$$R_{\mathrm{SRH}} = An \tag{2.1}$$

Where *A* is SRH recombination coefficient, and *n* is the carrier concentration. This recombination is dominant at low injection current.

Radiative recombination. This is the most important type of recombination in light emitting devices since it is directly connected to the light emission. In a radiative recombination process, an excited electron drops back to the valence band via emitting a photon. It can occur via various mechanisms including band-to-band recombination (Fig. 2.2b), excitonic recombination, and donor-acceptor recombination. In band-to-band recombination, the energy of an emitted photon is determined by the bandgap. In either an excitonic recombination or a donor-acceptor recombination, the energy of an emitted photon is reduced by the exciton-binding energy or the activation energy of the particular dopants. The recombination rate of radiative recombination can be described by:

$$R_{\mathrm{rad}} = Bn^2 \tag{2.2}$$

Where B is the radiative recombination coefficient with a typical value of 10^{-11} to 10^{-9} cm^3/s in III-nitrides[4].

Auger recombination (Fig. 2.2c). The mechanism of Auger recombination is similar to radiative recombination. However, instead of emitting a photon, when an excited electron drops back to the valence band, the energy will be used to excite another electron in the conduction band to a higher energy state leading to a hot electron. The hot electron will eventually lose its energy via emitting phonons (lattice vibration or heat), and therefore an Auger recombination process is non-radiative. The recombination rate can be described by:

$$R_{\mathrm{Aug}} = Cn^3 \tag{2.3}$$

Where C is the Auger recombination coefficient. This type of recombination is especially noteworthy at high injection current, and it is considered to be a potential cause of efficiency droop[5].

The recombination lifetime is the average time before an excited electron recombines with a hole. In a semiconductor material, the total recombination lifetime can be expressed in terms of both radiative lifetime (τ_{rad}) and non-radiative lifetime ($\tau_{\mathrm{non\text{-}rad}}$), as shown in the equation below[6]:

$$\tau^{-1} = \tau_{\mathrm{rad}}^{-1} + \tau_{\mathrm{non-rad}}^{-1} \tag{2.4}$$

Generally, the non-radiative term is more sensitive to defect density and temperature. A short recombination lifetime is also preferred since it is a decisive factor in determining the modulation bandwidth for visible light communication (VLC) applications.

2.1.4 LED Structure

Basically, a LED is a p-n junction. Due to the concentration gradient of carriers, the holes and electrons diffuse into the n-type and p-type side, then forming a depletion region between them across which a built-in electrical field. Fig. 2.3a shows a typical electric circuit for the operation of a LED consisting of a p-n junction. When the built-in electric field is sufficiently strong, the net diffusion of carriers is restricted, and an equilibrium is reached, as shown in Fig. 2.3b.

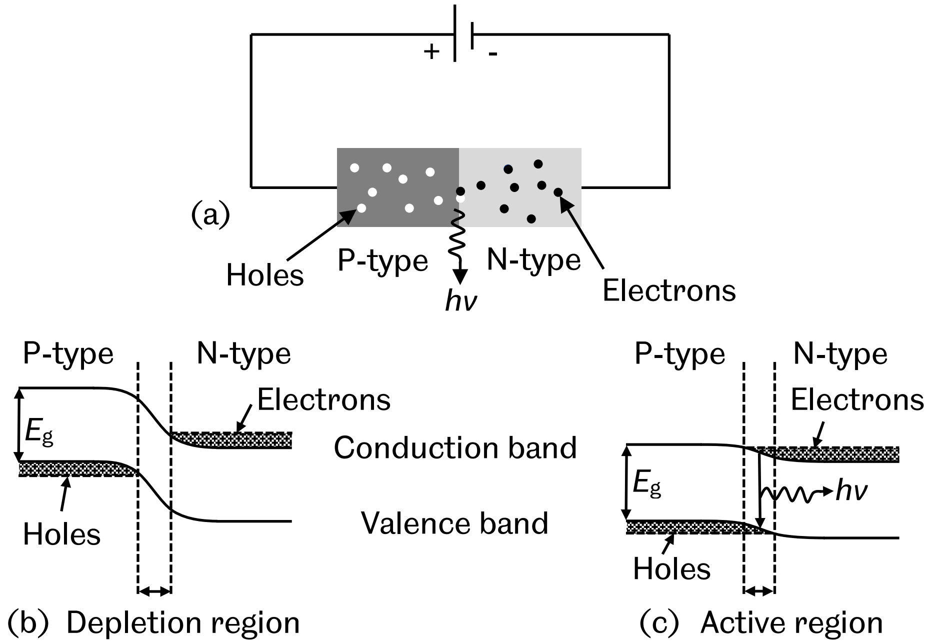

Figure 2.3. (a) schematic of a p-n junction under forward bias, (b) energy band diagram of a p-n junction under zero bias, and (c) energy band diagram of a p-n junction under forward bias.

When a forward bias is applied, the electrons and holes are injected from the n-side and p-side, respectively. This will break the equilibrium within the junction and then reduce the depletion region, allowing electrons and holes to further diffuse into the opposite region. An active region is therefore formed, where electrons and holes recombine and emitting photons, as shown in Fig. 2.3c.

2.2 III-nitride Semiconductors

Unlike the group IV elemental semiconductors such as Si and Ge, compound semiconductors are composed of at least two different elements, typically from group III and V, which is therefore called III-V semiconductors. Compound semiconductors have a good capability of forming alloys making the bandgaps to be tunable by changing alloy content. The III-nitride semiconductor family consists of GaN, indium nitride (InN), aluminium nitride (AlN) and their ternary or quaternary alloys. Compared with other III-V semiconductors, III-nitrides all exhibit a direct bandgap structure, with their bandgaps covering a wide region of the spectrum from deep UV, through the whole visible region, up to infrared (Fig. 2.4). This gives III-nitrides a huge advantage over other III-V semiconductors and makes them potentially the best candidates for optoelectronic devices.

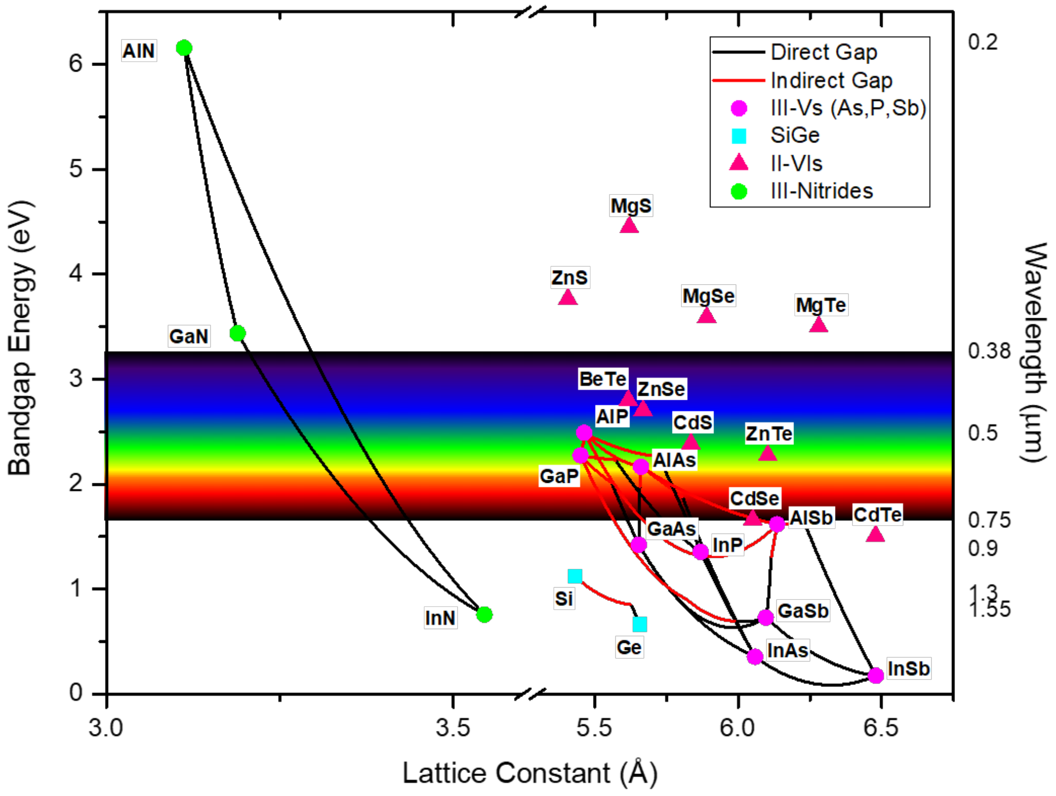

Figure 2.4. Bandgap at room temperature and emission wavelength as a function of the lattice constant of various compound semiconductors. Reproduced with permission[7].

2.2.1 Crystal Structure of III-nitride

III-nitride materials have three different types of crystalline structures: wurtzite, zinc-blende and rock salt. The rock salt form can exist only under high pressures (> 37 GPa), and thus it is not practically useful at ambient environment[8]. The cubic zinc-blende structure can be grown on a cubic substrate such as GaAs, but it always has a tendency to convert into a wurtzite structure which is more thermodynamically stable. The wurtzite structure, being the most stable form of III-nitrides, is therefore the most widely used crystal structure in III-nitrides. It is also the only structure used in the research presented in this thesis.

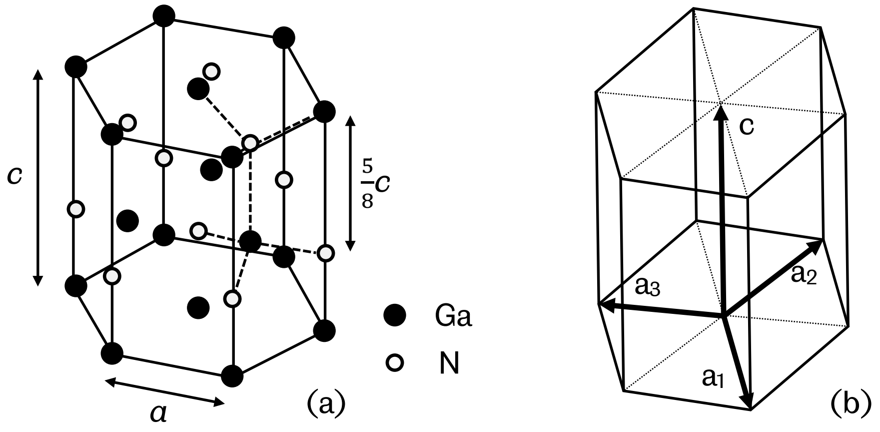

Figure 2.5. (a) atom configuration of GaN wurtzite structure and (b) coordinate system of Miller indices in a hexagonal unit cell.

As shown in Fig. 2.5a, the wurtzite structure of III-nitride exhibits an ABABAB hexagonal-close-packed (HCP) configuration. Two HCP sublattices, each with Ga or N atom, are interpenetrating each other with an offset of 5/8 of the cell height. Within a single unit cell, the distance between two adjacent atoms within the same basal plane is defined as in-plane lattice constant a, and the distance between two basal planes (cell height) is defined as out-of-plane lattice constant c. Table 2.1 lists the lattice constants and the bond parameters of III-nitrides[9].

III-nitrides	Lattice constant a (Å)	Lattice constant c (Å)	Bond length (Å)	Bond energy (eV/bond)
GaN	3.1893	5.1851	1.94	2.20
AlN	3.112	4.982	1.89	2.88
InN	3.5446	5.4034	2.15	1.93

Table 2.1. Crystal parameters of wurtzite structure III-nitrides.

In order to precisely describe planes and directions of the lattice, Miller indices h, k, l, and ℓ are introduced. As shown in Fig. 2.5b, h, k, i denote the intercept reciprocals of a plane along the axes a_1, a_2, a_3 in the basal plane, while ℓ denotes the intercept reciprocal of a plane along the c axis, which is perpendicular to the basal plane. This plane is therefore denoted by ($hkil$). If the round brackets are replaced by square brackets, [$hkil$], they represent a direction instead of a plane. Indices h, k, i, are 120 degrees to each other, and they follow the relation below:

$$h + k = -i \tag{2.5}$$

Hence, a plane can also be denoted by three-indices ($hk\ell$) as i is redundant.

Due to the lack of symmetry along the c-axis, the wurtzite III-nitride crystals have two different crystallographic polarities. The structure demonstrated in Fig. 2.5a is a typical Ga-polar GaN structure, where the surface of the material is terminated with group III atoms. If the position of Ga and N atoms is turned upside-down, the surface of the material is then terminated with N atoms and therefore become N-polar GaN. In the Miller index system, the Ga-polar and N-polar plane are denoted as (0001) and (000-1) plane, respectively. In practice, most GaN grown on sapphire by MOCVD is Ga-polar GaN. Normally, Ga-polar GaN exhibits a smooth surface while N-polar GaN has a rough surface full of hexagonal hillocks (Fig. 2.6). The polarity also has an impact on many other aspects including chemical reactivity, impurity incorporation (doping), defect generation and direction of internal polarisation.

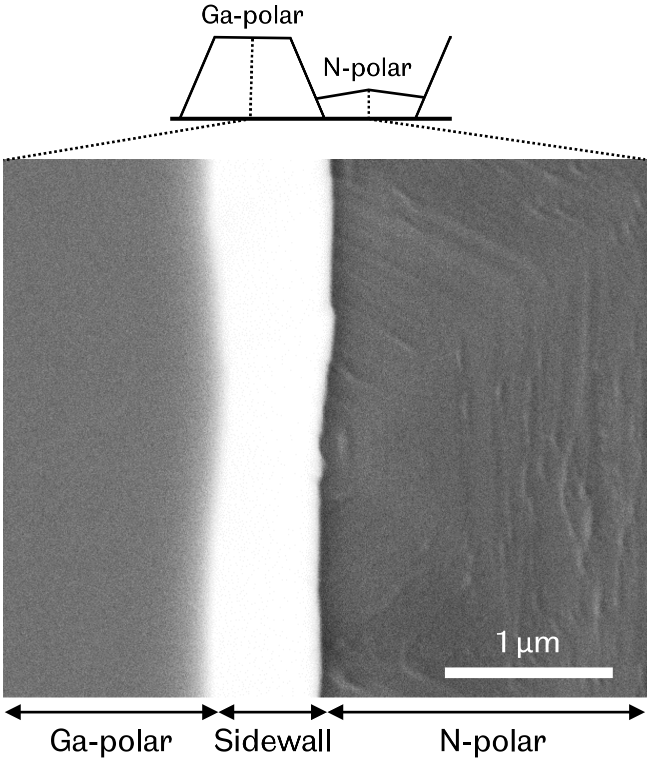

Figure 2.6. SEM image of top surfaces of N-polar and Ga-polar GaN.

2.2.2 Alloys and Tunable Bandgap

For III-nitride ternaries, the lattice constants have a linear relation with the alloy composition, which can be described by Vegard's law:

$$a_{\mathrm{A}_x\mathrm{Ga}_{(1-x)}\mathrm{N}} = xa_{\mathrm{AN}} + (1-x)a_{\mathrm{GaN}} \tag{2.6}$$

Where a_{AN} is the lattice constant of AlN or InN, a_{GaN} is the lattice constant of GaN, and x is the mole fraction of Al or In.

Similar to the lattice constants, the bandgap energies of ternary alloys also have a strong dependence on the alloy composition. However, in most cases, the relation cannot be accurately described by a linear interpolation. It can be expressed by an empirical expression, which takes a bowing parameter into account:

$$E_{\mathrm{g},\mathrm{A}_x\mathrm{Ga}_{(1-x)}\mathrm{N}} = xE_{\mathrm{g,AN}} + (1-x)E_{\mathrm{g,GaN}} - bx(1-x) \tag{2.7}$$

Where $E_{\mathrm{g,AN}}$ is the bandgap of AlN or InN, $E_{\mathrm{g,GaN}}$ is the bandgap of GaN, and b is the bowing parameter related to the curvature and strain state of the alloy.

III-nitrides	Bandgap (eV)	Corresponding Wavelength (nm)
GaN	3.42	363
AlN	6.2	200
InN	0.78	1590

Table 2.2. Bandgaps of III-nitrides and their corresponding emission wavelength.

Table 2.2 lists bandgap and the corresponding emission wavelength of III-nitrides[9]. Among which, AlN and GaN are wide bandgap semiconductors with bandgaps corresponding to deep ultraviolet (DUV) and UV spectrum, respectively, while InN has a narrower bandgap corresponding to infrared emission. Therefore, the bandgap energies of III-nitride ternaries can be continually tuned through alloying with a range from 6.2 eV (200 nm) to 0.78 eV (1590 nm), which also include the full spectrum of visible light (380-740 nm).

2.2.3 Electrical and Chemical Properties

Table 2.3 lists some basic electrical and thermal properties of GaN in comparison with the other two major kinds of semiconductors. Electron mobility is a parameter that describes how fast electrons can move within a semiconductor material under the influence of an electric field. Electron mobility depends on scattering, such as phonons (lattice vibration), impurities and defects. Therefore, it is also a good indicator of crystal quality. Since the quality of GaN epilayer varies a lot depending on the substrate, growth technique and growth condition, electron mobility reported so far is inconsistent in the literature. Generally, the electron mobility in a high-quality GaN epilayer is around 1000 $cm^2V^{-1}s^{-1}$. Currently, the highest experimental data of electron mobility of GaN reported is 1245 $cm^2V^{-1}s^{-1}$ in freestanding GaN[10]. Compared with GaAs and Si, GaN exhibits a very high breakdown voltage. GaN also has excellent thermal conductivity, making it especially suitable to be used in high-power, high-frequency electronic devices in high-temperature environment.

Material	Electron mobility ($cm^2V^{-1}s^{-1}$)	Breakdown field ($MV \cdot cm^{-1}$)	Thermal conductivity ($W \cdot cm^{-1}K^{-1}$)	Melting point (°C)
GaN	1245[10]	3.3[11]	2.3[9]	2500[12]
GaAs	9400[13]	0.4[14]	0.55[13]	1238[15]
Si	1400[16]	0.3[17]	1.56[18]	1414[15]

Table 2.3. Electrical and thermal properties of common semiconductor materials at 300K.

GaN also exhibits exceptional chemical and thermal stability, and therefore the etching and processing of GaN are very difficult. Furthermore, the chemical stability of GaN is strongly dependent on the polarity and crystal quality. Ga-polar GaN is inert and cannot be etched in most common acidic and alkaline solutions[19]. However, N-polar GaN and surface defects on Ga-polar GaN can be attacked by various etchants, including phosphoric acid (H_3PO_4) and potassium hydroxide (KOH). These etchants are therefore often used to determine the polarity of III-nitrides.

2.2.4 Internal Polarisations

Wurtzite c-plane III-nitrides exhibit strong internal polarisation. The origin of the polarisation comes from different electronegativities of group III and N atoms. As a result, III-N bonds are partly ionised, leading to an intrinsic dipole moment. In a symmetric crystal structure such as zinc-blende GaN, the dipole moments are cancelled out, resulting in a zero moment macroscopically. However, due to the lack of inversion symmetry, such cancellation in wurtzite GaN is incomplete and therefore leads to a net dipole moment pointing to [000-1] direction. This polarisation exists independent of strain state and is termed as spontaneous polarisation (Fig. 2.7a). In unstrained III-nitrides, the spontaneous polarisation of GaN, InN, and AlN are -0.029, -0.032 and -0.081 C/m^2, respectively[20]. The spontaneous polarisation of III-nitrides ternaries can be estimated by Vegard's interpolation:

$$\boldsymbol{P}_{\mathrm{sp,A}_x\mathrm{Ga}_{(1-x)}\mathrm{N}} = x\boldsymbol{P}_{\mathrm{sp,AN}} + (1-x)\boldsymbol{P}_{\mathrm{sp,GaN}} \tag{2.8}$$

Where $\boldsymbol{P}_{\mathrm{pz,AN}}$ is the spontaneous polarisation of AlN or InN, $\boldsymbol{P}_{\mathrm{pz,GaN}}$ is the spontaneous polarisation of GaN, and x is the mole fraction of Al or In.

Upon the existence of strain, group III and N atoms are shifted from their equilibrium position and result in a new polarisation field. This polarisation is termed as piezoelectric polarisation. In a wurtzite c-plane III-nitride material, assuming that $\varepsilon_{\mathrm{xx}}$ and $\varepsilon_{\mathrm{yy}}$ represent the isotropic in-plane strains and $\varepsilon_{\mathrm{zz}}$ is the out-of-plane strain along the c-axis, the strain can be expressed by:

$$\varepsilon_{\mathrm{xx}} = \varepsilon_{\mathrm{yy}} = \frac{(a-a_0)}{a_0} \tag{2.9}$$

$$\varepsilon_{\mathrm{zz}} = \frac{(c-c_0)}{c_0} \tag{2.10}$$

Where a and c are the strained lattice constants, and a_0 and c_0 are the lattice constants at equilibrium. The piezoelectric polarisation can then be estimated by equation:

$$\boldsymbol{P}_{\mathrm{pz}} = e_{31}(\varepsilon_{xx} + \varepsilon_{yy}) + e_{33}\varepsilon_{zz} \tag{2.11}$$

Where e_{31} and e_{33} are the piezoelectric constants (Fig. 2.7b)[20].

The total polarisation, which is the sum of spontaneous polarisation and piezoelectric polarisation, can then be expressed by:

$$\boldsymbol{P} = \boldsymbol{P}_{\mathrm{sp}} + \boldsymbol{P}_{\mathrm{pz}} \tag{2.12}$$

In a bulk material, spontaneous polarisation induced electric field can be counteracted by the free carriers accumulated at the material surface, and therefore result in a zero macroscopic electrostatic field across the material. Additionally, a bulk layer normally has the thickness way above the critical thickness, and therefore the strain is usually relaxed through buffer layers or the formation of dislocations and cracks, resulting in a relatively small piezoelectric field. However, in a heterostructure such as AlGaN/GaN and InGaN/GaN QW, due to their differences in spontaneous polarisation, an electrostatic field will exist across the QW structure. In addition, since QW is a thin layer sandwiched between two relatively thick barriers, the QW will be forced to have the same lattice constants as the barriers, and therefore give rise to a stronger piezoelectric field.

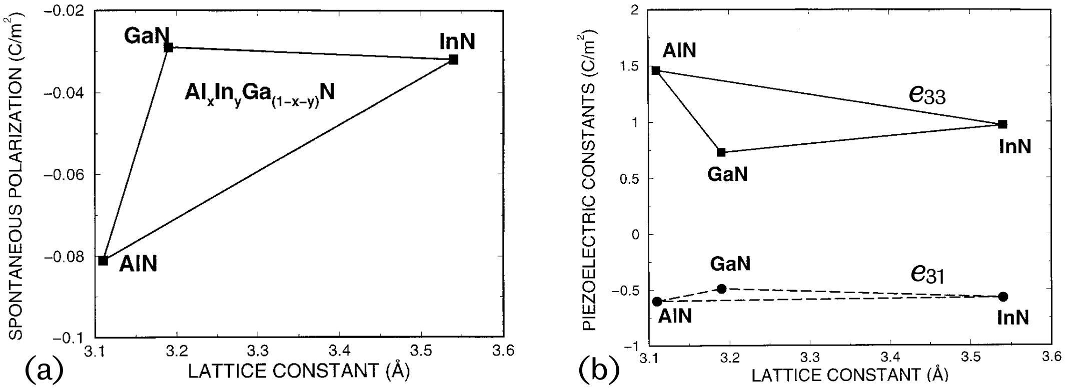

Figure 2.7. (a) spontaneous polarisations of III-nitrides as a function of lattice constant and spontaneous polarisations in III-nitride alloys according to a Vegard-like rule. (b) Piezoelectric coupling constants e_{31} (dash line) and e_{33} (solid line) of III-nitrides as a function of lattice constants. Triangles represent III-nitride alloys according to a Vegard-like rule. Reproduced with permission[21].

Figure 2.7 summaries spontaneous polarisation and piezoelectric constants of III-nitrides and their alloys as a function of lattice constants. AlN has a spontaneous polarisation nearly three times higher than GaN, and a lattice constant slightly smaller than GaN. Therefore, for an AlGaN/GaN QW, the AlGaN layer is under tensile strain, resulting in a piezoelectric polarisation point to [000-1], which adds up with dominant spontaneous polarisation. InN has almost the same spontaneous polarisation as GaN, but the lattice constant is much larger.

Therefore, in an InGaN/GaN QW, the piezoelectric polarisation is dominant and point to [0001] direction, which is opposite to the spontaneous polarisation direction.

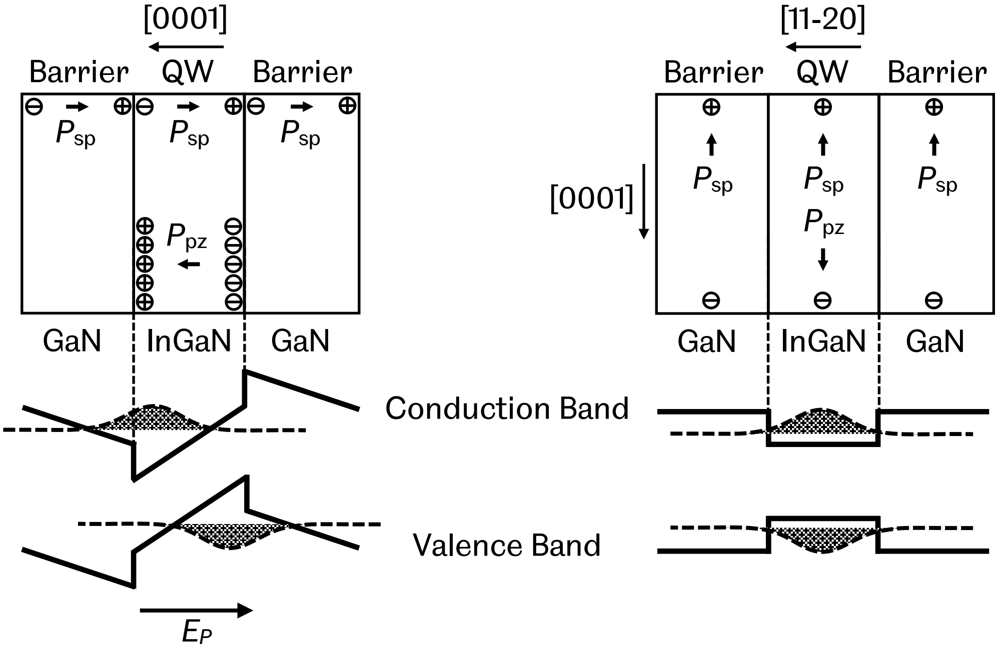

Figure 2.8. Schematic of polarisation orientation and band structure of (a) a polar c-plane InGaN/GaN QW, and (b) a non-polar a-plane InGaN/GaN QW.

Figure 2.8a illustrates the polarisation and the distorted band structure of a typical c-plane InGaN/GaN QW structure. The total polarisation pointing to the growth direction causes charges to accumulate at the interface between the InGaN QW and the GaN barrier, generating a strong electric field with reversed direction across the QW structure. As a result of the built-in electric field, the electrons and holes are pulled towards opposite directions, leading to a spatial separation of electrons and holes. The band structure is distorted, and the conduction band minimum and valence band maximum, as well as electron and hole wavefunctions, are separated. These effects caused by the electric field are termed as the quantum confined Stark effect (QCSE).

The effects of the QCSE are manifold. Firstly, the distortion in band structure lowers the band energy of bandgap and therefore causes an endogenic redshift in the emission wavelength. The red shift is supposed to be beneficial for obtaining a longer emission wavelength. However, as the carrier density increases with the increasing injection current, the redshift will be gradually screened out, which in turn leads to a blueshift and poor wavelength stability. Second, the reduced overlap of electron and hole wavefunction increases the radiative recombination lifetime, thus reducing the internal quantum efficiency (IQE). The increased recombination lifetime also limits the maximum modulation bandwidth for VLC applications.

The QCSE also affects In composition in InGaN QWs. Increasing In composition is crucial for achieving emission with a longer wavelength, such as green and yellow. However, increasing In composition also increases the strain in InGaN QWs, which in turn leads to a stronger QCSE, further reducing the overlap of electron and hole wavefunctions. This is a major cause of the low efficiency in conventional III-nitride LEDs with long emission wavelength.

2.3 Semi-polar and non-polar III-nitrides

Many approaches have been proposed to combat polarisation induced QCSE, mainly through strain relaxation to reduce piezoelectric fields or through the screening effect to directly shield QWs from QCSE. However, these approaches are not the ultimate solution to eliminate the polarisation induced QCSE. The most promising approach is to grow GaN along either semi-polar or non-polar orientation.

2.3.1 Semi-polar and Non-polar planes

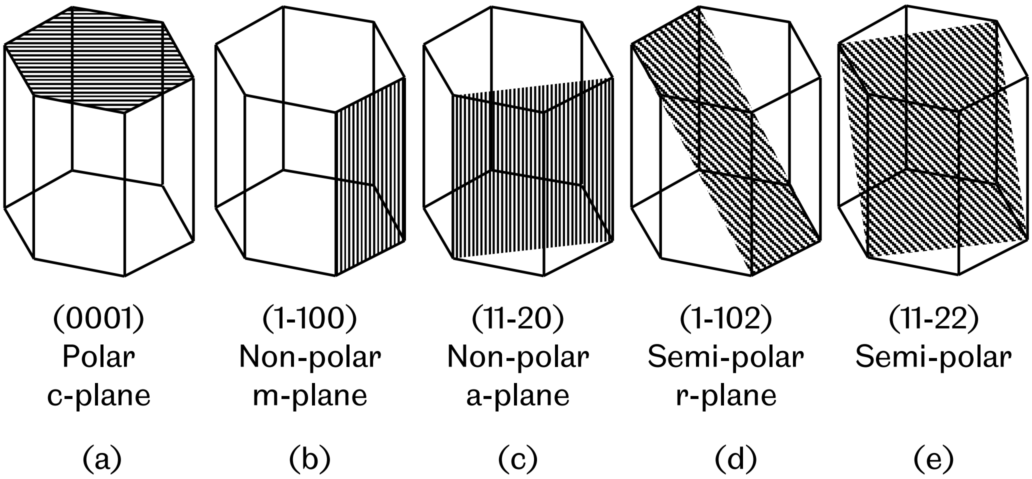

Figure 2.9. Five common planes in hexagonal crystal structures.

Figure 2.9 shows five common planes in a hexagonal crystal structure. In addition to the most widely used polar plane, i.e. (0001) c-plane, (1-100) m-plane and (11-20) a-plane are non-polar planes that are perpendicular to the c-plane, and (1-102) r-plane and (11-22) plane are semi-polar planes which have inclined angles between 0° and 90° with respect to the c-plane.

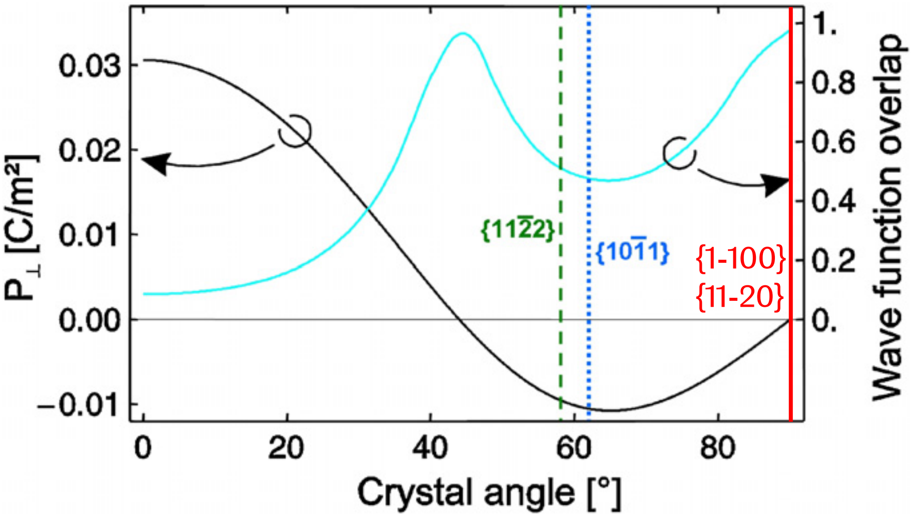

Figure 2.10. Piezoelectric polarisation and wavefunction overlap of electrons and holes in a 3 nm strained $In_{0.25}GaN$ QW as a function of inclined angle with respect to the c-plane. Reproduced with permission[22].

As indicated in Fig. 2.10, in contrast to the polar c-plane, the piezoelectric polarisation in an InGaN QW decreases with increasing inclination angle from 0°. The polarisation completely vanishes at around 45° and then starts to increase with a reversed direction before completely vanishing again at 90°. For semi-polar planes such as (11-22) and (10-11), the internal fields are significantly reduced but not zero. However, in non-polar planes such as (1-100) and (11-20), the electric field is zero. The research presented in this thesis focuses on the study of non-polar (11-20) a-plane GaN.

2.3.2 Epitaxy of Semi-polar and Non-polar III-nitrides

The major growth technique for the epitaxial growth of III-nitrides is metal organic chemical vapour deposition (MOCVD), along with molecular beam epitaxy (MBE) mainly for nanostructures and hydride vapour phase epitaxy (HVPE) for GaN or AlN bulk materials, which are not within the research scope in this thesis.

III-nitride samples used in this thesis were grown using MOCVD. For the growth of III-nitrides, metal organic sources, including trimethylgallium (TMG), trimethylindium (TMI), trimethylaluminum (TMA), and ammonia (NH_3) are used as precursors. The basic reaction of GaN growth in MOCVD can be described by:

$$\mathrm{Ga(CH_3)_3 + NH_3 \rightarrow GaN + 3CH_4} \qquad (2.13)$$

As we discussed in Chapter 1, due to the high price, small wafer size and limited availability of free-standing GaN, foreign substrates are still being widely used in researches and for commercial purposes. Sapphire is the most common foreign substrate for III-nitride epitaxy. Various crystal orientations including c-plane, a-plane, m-plane and r-plane are available. In the growth of c-plane GaN, c-plane sapphire is used. The physical in-plane lattice constant difference between GaN and sapphire is ~33%. However, c-plane GaN grown on c-plane sapphire has a 30° rotation around the c-axis, and the actual epitaxial relationship is (0001) GaN || (0001) sapphire and [2-1-10] GaN || [1-100] sapphire. This rotated epitaxial relationship leads the lattice mismatch down to ~16%.

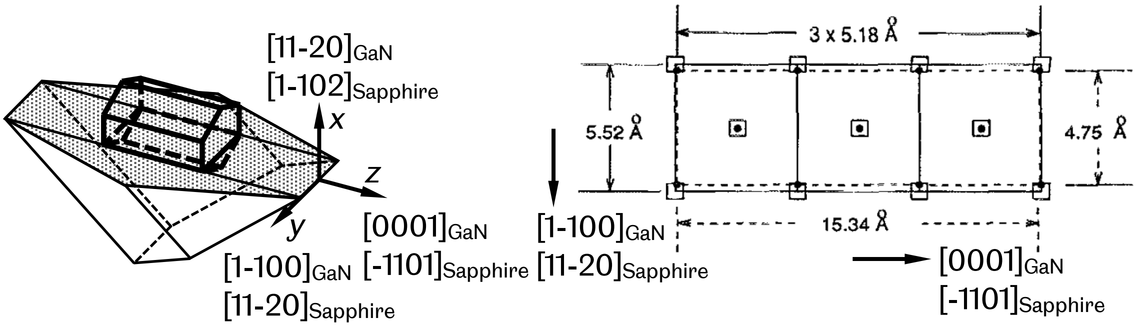

Figure 2.11. Schematic diagram of (a) epitaxial relationship of (11-20) a-plane GaN grown on (1-102) r-plane sapphire, and (b) projection of (11-20) a-plane and (1-102) r-plane sapphire atom position. The dots are Al atoms and dashed lines represent sapphire unit cell. The squares are Ga atoms and solid lines represent GaN unit cell. (b) is reproduced with permission[23].

In this thesis, (1-102) r-plane sapphire substrates are used to grow non-polar (11-20) a-plane GaN. Figure 2.11a illustrates the epitaxial relationship, which is (11-20) GaN || (1-102) sapphire, [0001] GaN || [-1101] sapphire and [1-100] GaN || [11-20] sapphire. The lattice mismatch is only 1% along the [0001] GaN direction, while it is ~16% along the [1-100] GaN direction (Fig. 2.11b). Such large mismatch will generate a large number of defects if directly grown on sapphire. Therefore, additional growth techniques are required to improve crystal quality.

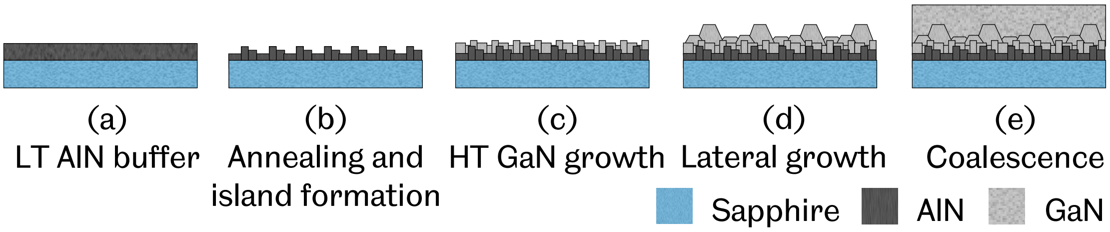

Figure 2.12. GaN growth mechanism of the traditional two-step method using an LT AlN buffer layer.

One traditional way to reduce defect density in heteroepitaxial growth is the well-known two-step growth method[24]. The mechanism of this method is illustrated in Fig. 2.12. Initially, a low temperature (LT) GaN or AlN nucleation layer with a thickness of 25 nm is grown on a nitridated sapphire substrate at ~550°C. The thin nucleation layer is then annealed at ~1000°C to be recrystallised, forming polycrystalline islands. These islands then act as nucleation sites and provide growth centres for high temperature (HT) GaN to be grown at a temperate above 1000°C. The GaN continues to grow laterally, then turns to a quasi-2D growth and finally coalesce, forming a high-quality GaN layer with a smooth surface.

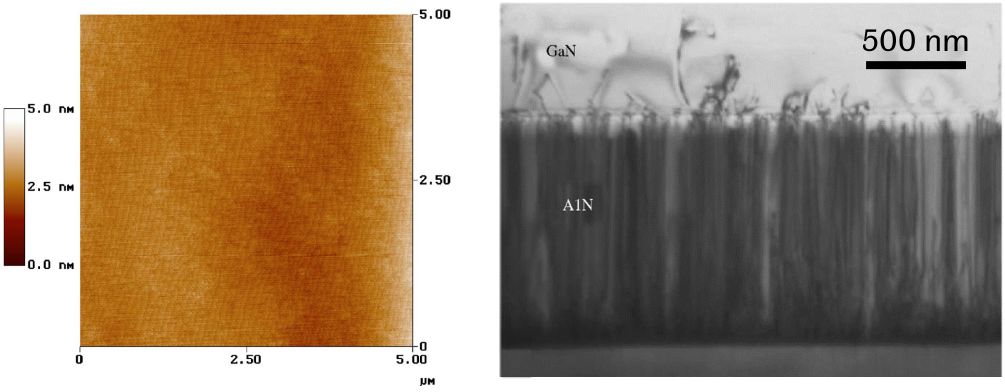

(a) (b)

Figure 2.13. (a) AFM image of a typical HT AlN buffer layer, (b) TEM image of GaN grown on HT AlN buffer layer, taken around the [11-20] zone axis, g = [1-100]. Reproduced with permission[25,26].

A different defect reduction technique utilising an HT AlN buffer layer was developed by our Sheffield group to further improve the crystal quality[25]. In this method, an HT AlN buffer layer is grown at 1200°C to form an atomically flat surface. Figure 2.13a shows a typical 5×5 μm^2 AFM image of our HT AlN buffer layer with a root-mean-square roughness of ~2 Å. The defects are then blocked by the high density of V-shape pits generated at the interface between the AlN buffer and the GaN layer, resulting in a massive reduction in dislocation density in the overlying GaN layer, as shown in the Fig. 2.13b. This HT AlN buffer provides an excellent template for GaN growth, which has been used for semi-polar and non-polar GaN growth on m-plane and r-plane sapphire.

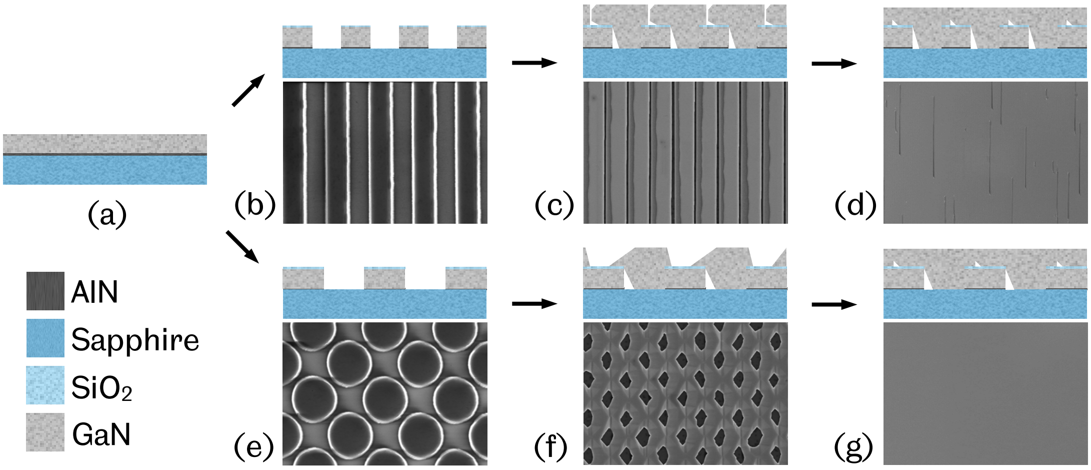

Figure 2.14. Schematic illustration of overgrowth process and corresponding SEM images of (a) an as-grown template, (b) - (d) non-polar (11-20) GaN overgrown on a stripe patterned as-grown GaN template, (e) – (f) non-polar (11-20) GaN overgrown on a micro-rod patterned as-grown GaN template.

Further improvement of crystal quality can be achieved by epitaxial lateral overgrowth (ELOG) or techniques evolved from ELOG such as sidewall lateral epitaxial overgrowth (SLEO). In these techniques, an ex-situ fabrication process is required to fabricate patterned substrates or templates for overgrowth. Figure 2.14 illustrates two different types of non-polar a-plane GaN templates used in this thesis and their corresponding overgrowth process. Initially, an as-grown a-plane GaN template is grown by using HT AlN buffer technique. The as-grown template is then fabricated into micro-stripes or micro-rods templates using SiO_2 masks by photolithography. Only the exposed sidewalls provide growth faces for the overgrowth of GaN. During the overgrowth, SiO_2 masks will force GaN to grow laterally, and therefore effectively block defects that propagate vertically such as dislocations. Eventually, GaN will grow over the SiO_2 masks and coalesce laterally, forming a smooth a-plane surface. More details regarding the fabrication of templates will be included in Chapter 3, and the details of defects reduction mechanism of overgrowth will be discussed in Chapter 7.

2.3.3 Defects in Semi-polar and Non-polar III-nitrides

In addition to dislocations, which is the major defects for c-plane GaN, stacking faults are also equally important for semi-polar and non-polar GaN. Generally, defects can be classified into four categories according to their dimensionality:

- 0D – point defects, including vacancies, interstitials and substitutional impurities
- 1D – line defects, which are associated with the displacement of atoms along a line, such as dislocations.
- 2D – planar defects, which are associated with misalignment of atoms within a plane, such as stacking faults.
- 3D – volume defects, which are macroscopic and associated with a volume of atoms, including pits, voids and cracks.

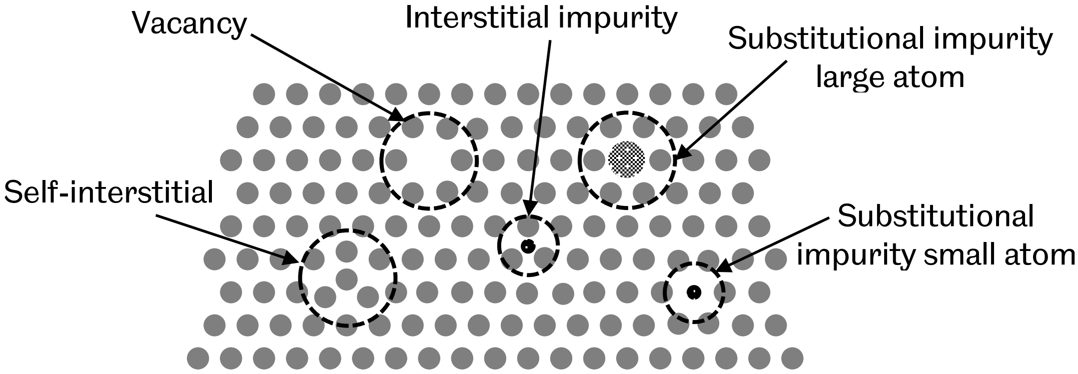

Figure 2.15. Schematic illustration of some common types of point defects.

Figure 2.15 shows three main types of point defects: vacancies, interstitials and substitutional atoms. A vacancy is an unoccupied lattice site where an atom is missing. An interstitial is an atom which occupies a non-lattice site locating between regular atoms. If an external impurity atom replaces a regular atom, it is called a substitutional atom. Point defects have a significant impact on the electrical and optical properties of semiconductor materials. In III-nitrides, two most common effects of point defects are "unintentional n-type doping", which is attributed to N vacancies, and Ga vacancies leading to the well-known "yellow-band emission".

A dislocation is a line defect and can be regarded as the boundary line between displaced and undisplaced regions within the crystal. Dislocations can be characterised by two parameters, the Burgers vector ***b***, which describes the magnitude and the direction of the displacement associated with the dislocation, and the dislocation line, which points along the direction of dislocation. Figure 2.16 shows two main types of dislocations: edge dislocations, which has a dislocation line perpendicular to the Burgers vector, and screw dislocations, which has the paralleled dislocation line and Burgers vector. In many cases, dislocations are not purely edge nor screw dislocations but an intermediate of both, which are labelled as mixed dislocations.

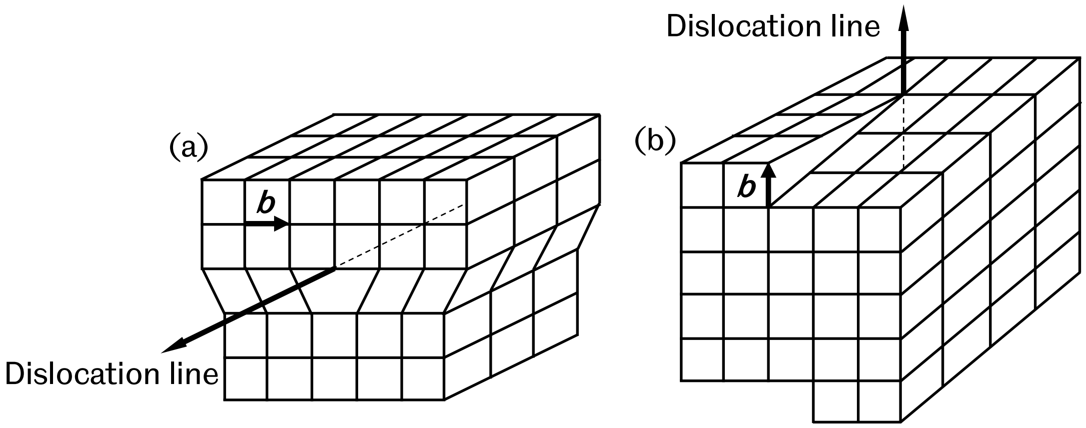

Figure 2.16. Schematic illustration of (a) edge dislocation and (b) screw dislocation.

In a crystal, if the Burger vector of a dislocation has the same magnitude as the translation vector of the lattice, the motion of the dislocation leaves regions with the perfect crystal structure, and therefore it is called a perfect dislocation. In III-nitrides, there are three types of perfect dislocations: a-type (edge) dislocation, with a Burgers vector of ***b*** = 1/3<11-20>, c-type (screw) dislocation, with ***b*** = <0001>, and a+c type (mixed) dislocation, with ***b*** = 1/3<11-23>. Since the total energy can be lower, these perfect dislocations tend to split in two, creating partial dislocations associated with the formation of the imperfect crystal structure (stacking faults). Typical partial dislocations often observed in semi-polar and non-polar III-nitrides include Shockley partial dislocation, with ***b*** = 1/3<1-100>, Frank partial dislocation, with ***b*** = 1/2<0001>, and Frank-Shockley partial dislocation, with ***b*** = 1/6<20-23>.

If no defect reduction technique is employed, the dislocation density in semi-polar and non-polar GaN can be as high as $\sim 10^{10}$ cm^{-2} [27]. These dislocations then act as electron scattering and non-radiative recombination centres, which adversely impact the electrical and optical properties of the material. Dislocations are also found to be associated with the generation of 3D defects such as surface pits[28].

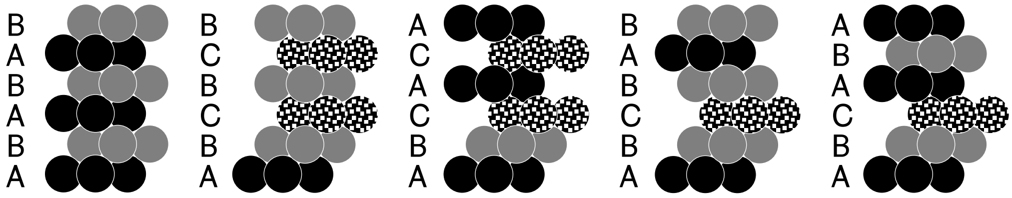

Normal stack (a) I_1-type BSF (b) I_2-type BSF (c) I_3-type BSF (d) E-type BSF (e)

Figure 2.17. Schematic illustration of the stacking sequence of a normal stack and different types of BSF in wurtzite III-nitrides.

Stacking faults (SFs) are a type of planar defects which characterise the disrupted stacking sequences. In wurtzite structure III-nitrides, the normal stacking sequence of basal planes is ABABAB (Fig. 2.17a). In some occasions, the sequence is interrupted by the substitution or insertion of a layer in C configuration, resulting in an abnormal stacking sequence such as ABCBCB. This is so-called basal stacking faults (BSFs).

Figure. 2.17 shows that BSF consists of three types of intrinsic BSFs, namely I_1, I_2, and I_3, and an extrinsic E-type BSF. Intrinsic BSFs are formed by substituting an A or B layer with a wrong C layer, while an extrinsic BSF is the insertion of a C layer. Most of these BSFs are associated with partial dislocations. An I_1-type BSF is associated with Frank-Shockley partial dislocation and is the most common BSF observed in semi-polar and non-polar III-nitrides due to its low formation energy. The formation of an I_1-type BSF involves the removal or insertion of an additional basal plane. Therefore, it can only be formed during the growth but not through strain relaxation. An I_2-type BSF is bounded with Shockley partial dislocations. It can be formed directly by a shear of the basal plane and so it can be formed during strain relaxation. An I_3-type BSF is formed by a single stacking error and has no association with any partial dislocations. An E-type BSF is associated with Frank partial dislocations and is rarely observed in practice as it has the highest formation energy.

Reference

1. Sze, S. M. & Lee, M.-K. *Semiconductor Devices: Physics and Technology. Physics of Semiconductor Devices: Second Edition* (JOHN WILEY & SONS, INC., 2016).

2. Hall, R. N. Electron-Hole Recombination in Germanium. *Phys. Rev.* **87**, 387–387 (1952).

3. Shockley, W. & Read, W. T. Statistics of the Recombinations of Holes and Electrons. *Phys. Rev.* **87**, 835–842 (1952).

4. Morkoç, H. *Nitride Semiconductor Devices*. (Wiley-VCH Verlag GmbH & Co. KGaA, 2013). doi:10.1002/9783527649006

5. Iveland, J., Martinelli, L., Peretti, J., Speck, J. S. & Weisbuch, C. Direct measurement of auger electrons emitted from a semiconductor light-emitting diode under electrical injection: Identification of the dominant mechanism for efficiency droop. *Phys. Rev. Lett.* **110**, 2–6 (2013).

6. Wang, T. Topical Review: Development of overgrown semi-polar GaN for high efficiency green/yellow emission. *Semicond. Sci. Technol.* **31**, 093003 (2016).

7. Farrer, I. Lecture Notes from EEE6212 Semiconductor Materials. (University of Sheffield, 2019). Data from Montgomery, K. "Semiconductor Band Parameters" available at: https://web.archive.org/web/20160928024026/www.kmontgomery.net/resources/semiconductor-band-parameters. (Accessed: 13th November 2019)

8. Xia, H., Xia, Q. & Ruoff, A. L. High-pressure structure of gallium nitride: Wurtzite-to-rocksalt phase transition. *Phys. Rev. B* **47**, 12925–12928 (1993).

9. Morkoç, H. *Handbook of Nitride Semiconductors and Devices Vol. 1: Materials Properties, Physics and Growth*. (WILEY-VCH Verlag GmbH & Co. KGaA, 2008).

10. Look, D. C. & Sizelove, J. R. Predicted maximum mobility in bulk GaN. *Appl. Phys. Lett.* **79**, 1133–1135 (2001).

11. Chow, T. P. & Ghezzo, M. SiC POWER DEVICES. in *III-Nitride, SiC, and Diamond Materials for Electronic Devices* (eds. Gaskill, D. K., Brandt, C. D. & Nemanich, R. J.) **423**, 9 (Materials Research Society, 1996).

12. Porowski, S. Growth and properties of single crystalline GaN substrates and homoepitaxial layers. *Mater. Sci. Eng. B* **44**, 407–413 (1997).

13. Blakemore, J. S. Semiconducting and other major properties of gallium arsenide. *J. Appl. Phys.* **53**, (1982).

14. Kyuregyan, A. S. & Yurkov, S. N. Room-temperature avalanche breakdown voltages of p-n# 3 junctions made of Si, Ge, SiC, GaAs, GaP, and InP. *Sov. Physics--Semiconductors(English Transl.* **23**, 1126–1131 (1989).

15. Lide, D. R. et al. *CRC Handbook of Chemistry and Physics*. (CRC Press, 2004).

16. Norton, P., Braggins, T. & Levinstein, H. Impurity and lattice scattering parameters as determined from Hall and mobility analysis in n-type silicon. *Phys. Rev. B* **8**, 5632–5653 (1973).

17. Sze, S. M. & Ng, K. K. *Physics of Semiconductor Devices*. (John Wiley & Sons, Inc, 2007).

18. Slack, G. A. & Glassbrenner, C. J. Thermal conductivity of Si and Ge from 3K to the melting point. *Phys. Rev.* **1431**, (1964).

19. Zhuang, D. & Edgar, J. H. Wet etching of GaN, AlN, and SiC: A review. *Mater. Sci. Eng. R Reports* **48**, 1–46 (2005).

20. Bernardini, F., Fiorentini, V. & Vanderbilt, D. Spontaneous polarization and piezoelectric constants of III-V nitrides. *Phys. Rev. B* **56**, R10024–R10027 (1997).

21. Bernardini, F. & Fiorentini, V. Spontaneous versus Piezoelectric Polarization

in \III-V Nitrides. *Phys. Stat. Sol.* **216**, 391 (1999).

22. Scholz, F. Semipolar GaN grown on foreign substrates: A review. *Semicond. Sci. Technol.* **27**, (2012).

23. Lei, T., Ludwig, K. F. & Moustakas, T. D. Heteroepitaxy, polymorphism, and faulting in GaN thin films on silicon and sapphire substrates. *J. Appl. Phys.* **74**, 4430–4437 (1993).

24. Amano, H., Sawaki, N., Akasaki, I. & Toyoda, Y. Metalorganic vapor phase epitaxial growth of a high quality GaN film using an AlN buffer layer. *Appl. Phys. Lett.* **48**, 353–355 (1986).

25. Bai, J. *et al.* Optical properties of AlGaN/GaN multiple quantum well structure by using a high-temperature AlN buffer on sapphire substrate. *J. Appl. Phys.* **99**, 0–4 (2006).

26. Bai, J., Wang, T., Parbrook, P. J., Ross, I. M. & Cullis, A. G. V-shaped pits formed at the GaN/AlN interface. *J. Cryst. Growth* **289**, 63–67 (2006).

27. Craven, M. D., Lim, S. H., Wu, F., Speck, J. S. & Denbaars, S. P. Structural characterization of nonpolar $(11\bar{2}0)$ a-plane GaN thin films grown on $(1\bar{1}02)$ r-plane sapphire. *Appl. Phys. Lett.* **81**, 469–471 (2002).

28. Gao, Z. Y. *et al.* Different structural origins for different sized surface pits observed on a-plane GaN film. *Sci. China Technol. Sci.* **59**, 156–161 (2016).

Chapter 3

Experimental Techniques

Techniques employed in the research are presented in this chapter, including techniques for the fabrication of templates, metal organic chemical vapour deposition (MOCVD) for the growth of III-nitrides, and characterisation techniques for the assessment of samples. In this chapter, the principles behind each technique are provided in detail.

3.1 Fabrication Technique

3.1.1 Sample Treatment

Sample Cleaning

As a standard procedure, a cleaning process is employed to remove any residual dust, particles or contaminants on an epiwafer surface prior to any further fabrication and overgrowth. The standard cleaning process includes:

i. Immerse a wafer in ultrasonic bath wafers in n-butyl acetate (nBA), acetone, and isopropyl alcohol (IPA).
ii. Rinse wafers under flowing deionised water to remove solvent residual.
iii. Blow wafers with dry nitrogen to avoid water stains and the bake at 100 °C to completely remove adsorbed moisture.

In some occasions, oxygen plasma is employed to ash contaminants, in particular removing a residual photoresist and polymer. Solutions of acid or alkali, including potassium hydroxide (KOH), hydrochloride (HCl) and aqua regia (A.R.), are also used to remove stubborn contaminants and improve the adhesion of deposition films (Fig 3.1.).

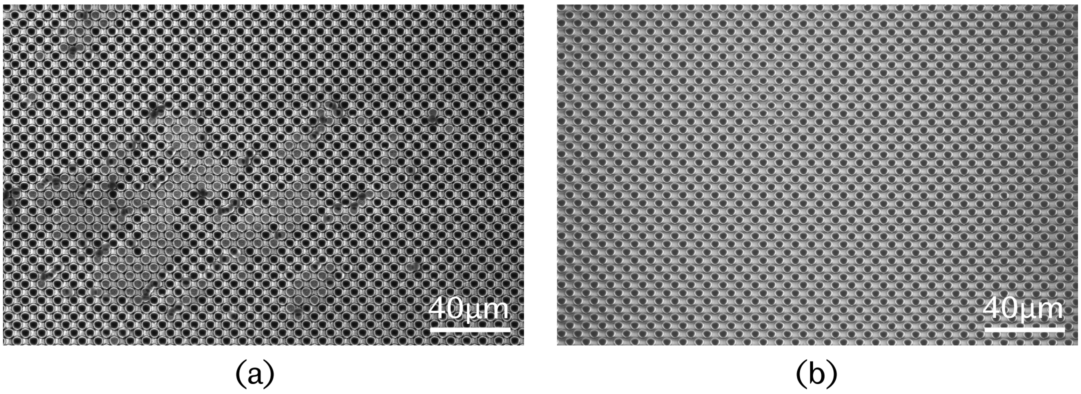

(a) (b)

Figure 3.1. SEM top view image of (a) a micro-rod template shows stripping of SiO_2 mask after 45 minutes of etching in 10% KOH (b) a micro-rod template treated with A.R. for 10 minutes before SiO_2 deposition, shows no sign of SiO_2 mask stripping after 2 hours etching in 10% KOH.

Photo-Enhanced Chemical Etching

In this work, photo-enhanced chemical (PEC) etching is adopted as a surface treatment for patterned template prior to the overgrowth process. As discussed in section 2.2.3, the wet etching of GaN is highly polarity dependent. Therefore, the PEC treatment takes advantage of this polarity selective property in order to create desired growth facets and encourage the growth along the defect-free [0001] direction (Fig. 3.2a).

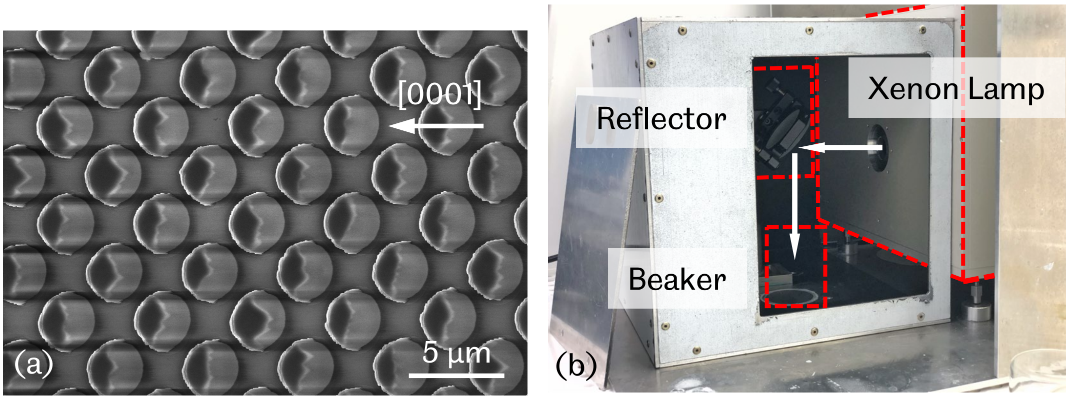

Figure 3.2. (a) SEM image of PEC etched micro-rod array. The shadow areas are the unetched GaN remains underneath the SiO_2 masks, and (b) the custom-built PEC etching system used in this work.

Figure 3.2b shows our home-made PEC etching set-up. The illumination source used is a 450 W xenon arc lamp with a power density of 1.5 W/cm^2. An aluminium coated ultraviolet (UV) reflector is used, which allows the UV light to be reflected and illuminate a sample vertically, which immersed in 10% KOH aqueous electrolyte contained by a beaker. The etch rate of GaN can be influenced by multiple factors including crystal orientation, shape of pattern, power and time of dry etching, etc. In the case of this study, a typical etch time for 2.5 μm micro-rod non-polar GaN template is 60 minutes and the estimated lateral etch rate along the [000-1] direction is 20 nm/min.

During the etching, the whole set-up is sealed in a metal box in order to confine any scattered UV light. As the xenon lamp emits photons with energy higher than the band gap of GaN, electron-hole pairs are therefore generated. The excited electrons are then consumed by the electrolyte, leaving photogenerated holes which can assist in the oxidation of GaN. The etch rate of GaN is therefore improved. The reaction of GaN with KOH can be denoted as[1]:

$$2\mathrm{GaN} + 3\mathrm{H_2O} \xrightarrow{\mathrm{KOH}} \mathrm{Ga_2O_3} + 2\mathrm{NH_3} \qquad (3.1)$$

Where KOH works as both a catalyst for the reaction and a solvent for the reaction product Ga_2O_3.

3.1.2 Thin-film Deposition

Plasma Enhanced Chemical Vapour Deposition

Plasma Enhanced Chemical Vapour Deposition (PECVD) is a powerful tool for deposition of dielectric films such as SiO_2 or SiN by using plasma. As shown in Fig. 3.3a, during film deposition, reactant gases are fed into a reaction chamber, which contains a sample heated to 300 °C. The gases are then ionised by radio frequency (RF) in between of two paralleled electrodes, thus creating plasmas. Upon landing on the sample, the gas mixture, which contains atoms, molecules, ions and radicals, will generate precursors near the sample surface. These precursors then diffuse into the sample, forming the required thin film through surface reaction. In comparison with conventional CVD, the utilisation of plasma in PECVD allows dielectric films with higher quality to be deposited at a much lower temperature.

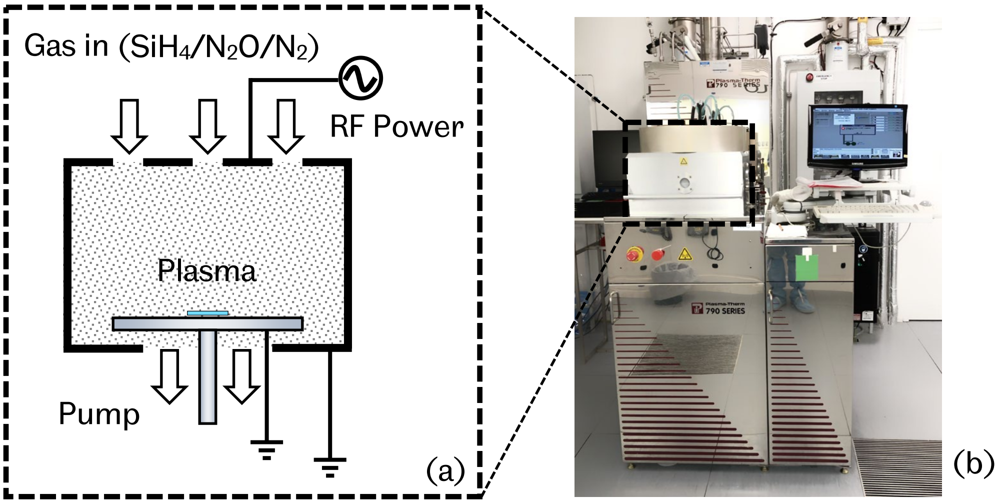

Figure 3.3. (a) schematic illustration of PECVD, and (b) the Plasma-Therm 790 PECVD system.

In this work, a Plasma-Therm 790 PECVD system (Fig. 3.3b) is employed to deposit the SiO_2 films. The reactant gases for SiO_2 deposition include SiH_4, N_2O and N_2, with flow rates of 160 sccm, 900 sccm and 240 sccm, respectively. The pressure within the chamber is 900 mTorr. At 25W RF power, the deposition rate is approximately 40 nm/minute. Typical thickness of the SiO_2 layer used in this work varies between 150 nm to 520 nm.

Thermal Evaporation

Thermal evaporation is a type of physical vapour deposition (PVD) commonly used for deposition of metallic thin films. In this work, an Edward E306A coating system (Fig. 3.4) is employed to deposit nickel (Ni) mask for dry etching. Before deposition, the source material is inserted into a tungsten evaporation coil and fitted onto a coil holder within the chamber. The target sample is placed on the base of the chamber below the evaporation coil. A quartz crystal monitor (QCM) with an accuracy of 0.1 nm/s is fitted beside the sample to monitor deposition thickness. The chamber is then sealed by using a bell jar.

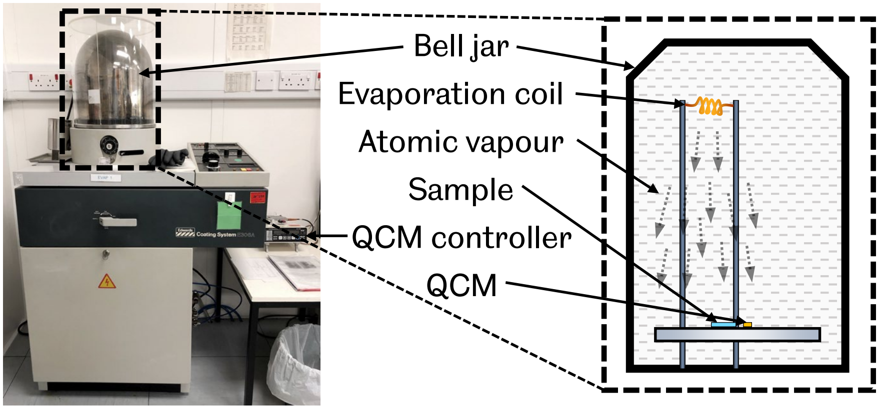

Figure 3.4. The Edward E306A coating system and the schematic illustration.

Typically, a high vacuum environment with a pressure of 2×10^{-6} Torr is required for thermal evaporation. Such pressure is normally achieved by a two-step pumping process using a combination of a rotary pump and a diffusion pump. Once the target vacuum is reached, the coil will be heated up by a large current flow (typically 20 to 35 A), melting and evaporating an atomic vapour from the source material.

3.1.3 Photolithography

Photolithography is a standard technique used for device fabrication. Generally, short wavelength light such as UV is utilised to transfer a geometric pattern from a pre-designed photomask to a photosensitive medium, which is termed photoresist. Due to the photosensitivity of such medium, photolithography must be carried out in a yellow room, where short wavelength light is filtered out to prevent a premature reaction from taking place in photoresists. A photolithography process can be roughly divided into three steps: coating, exposure, and developing.

Coating

Before the deposition of photoresist, a sample is cleaned and baked following the steps stated in section 3.1.1. The sample is then placed on a spinner stage and held by vacuum in a spin coater. A small amount of photoresist is then applied to the centre of the sample. The sample, along with the spinner stage, is then spun at high speed to spread the photoresist evenly, forming a uniform thin layer of photoresist. The photoresist coated sample is then prebaked at 100 °C for 1 minute to remove excess solvent and solidify the photoresist.

In this work, an EMS Model 4000 spin coater is employed to deposit photoresist. As most of our samples used in photolithography has a SiO_2 layer deposited on the top surface, a special adhesion promoter, hexamethyldisilazane (HMDS), is applied before the deposition of photoresist. Such a promoter can form a hydrophobic layer and stop aqueous developer solution from penetrating the interface of sample surface and photoresist. Two types of photoresist are used in this work, which are SPR-350 and ethylene carbonate (EC) diluted BPRS-200. SPR-350 is used in the most regular cases, while diluted BPRS-200 has larger freedom in controlling a pattern size therefore is used wherever fine-tuning is required. The dilution ratio of BPRS-200 and EC solvent is 10:4. Under a typical spin condition, which is 4000 RPM and 30 seconds, the thickness of the deposited photoresist is ~ 1 μm for both types.

Exposure

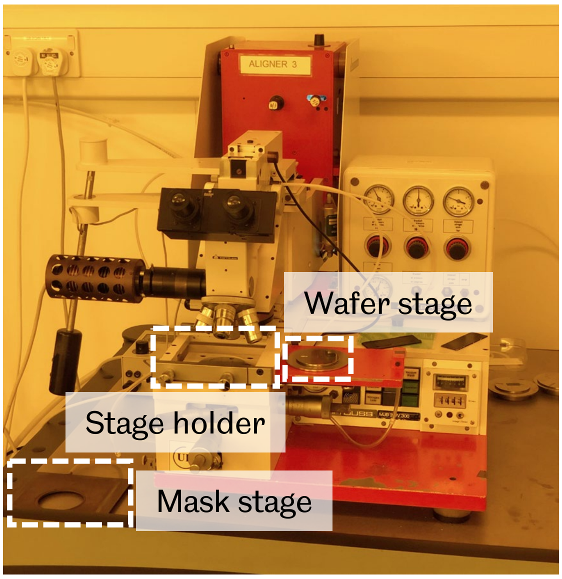

Figure 3.5. The Karl Suss MJB3 UV400 Mask Aligner in a yellow room.

A photomask is a quartz plate coated with patterned chrome on one side. The pattern has opaque regions which block light and has transparency regions that allow light to reach a sample underneath. During exposure processes, the pre-baked sample is loaded into a mask aligner. The photomask is mounted on a fixed mask holder, while the sample is held by vacuum on a movable sample stage, which can tune the relative position between the sample and the photomask (Fig. 3.5). Once the alignment is completed, the sample is brought to contact with the photomask, and the pattern is transferred onto the photoresist under UV illumination. With a positive photoresist, hydrophilic products are generated in the exposed areas. These areas are therefore become soluble in a developer. With a negative photoresist, insoluble polymers are formed in the exposed area. In this work, both SPR-350 and BPRS-200 photoresists are positive type. A Karl Suss MJB3 UV400 Mask Aligner is employed. The aligner uses a UV lamp with 365 and 405 nm wavelength as illumination source and features a print resolution of 0.8 μm under optimum condition.

Developing

A developing process is the last step of photolithography, in which the photoresist is partly removed by a corresponding developer. Depending on the type of photoresist and developer, the area left after developing could be either exposed or unexposed area. As both SPR-350 and BPRS-200 are positive, the corresponding developer MF-26A is a tetramethylammonium hydroxide (TMAH) based developer, leading the exposed area to be removed[2]. The developer is usually diluted in water with a ratio of 2:1, and a typical developing time is 60 seconds. However, the developer concentration and the developing time can be tuned for different purposes.

3.1.4 Dry Etching

Reactive-Ion Etching

Reactive-ion etching (RIE) is a dry etching technique which utilises chemically reactive plasmas to etch part of materials from a sample. The plasma generation mechanism is similar to that of a PECVD, namely, RF in between two paralleled electrodes to generate the plasma of reactant gases. However, instead of reacting and forming thin films, in RIE, the reactant gases react and etch the part of the sample. As illustrated in Fig. 3.6, the wall of the reaction chamber is grounded, which electrically isolate from a sample platter. As the electric field between two electrodes accelerates electrons vertically, charges are built up on the sample platter. These charges will drive reactive ions towards the sample, hence promoting the chemical reaction and ion bombardment.

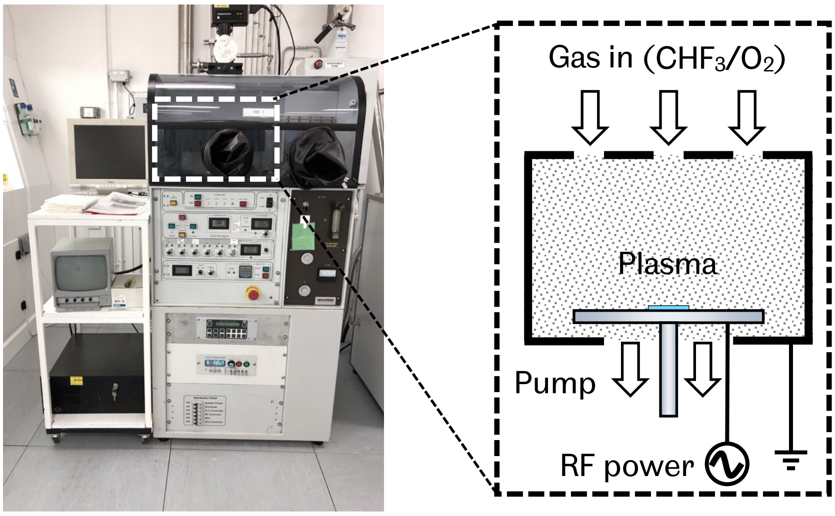

Figure 3.6. Plasma-Therm Shuttlelock RIE system and schematic illustration.

The RIE system used in this work is a Plasma-Therm Shuttlelock RIE, which is employed mainly for etching SiO_2 masks. The plasma is generated under a low pressure of 35 mTorr, with a 13.56 MHz RF power at 150 W. The etch rate is ~ 40 nm/minute. The etchant gases for SiO_2 etching are CHF_3 and O_2, with a flow rate of 35 and 5 sccm, respectively. During etching processes, fluorocarbon polymers are formed on the sample surface. These polymers can improve the anisotropy of the etching, as they can adhere to the sidewall and stop isotropic chemical reaction but not the vertical bombardment. However, the existence of an excessive amount of polymer can lower the etch rate and result in an incomplete etching with a large amount of SiO_2 grass-like residue. Therefore, a small amount of O_2 is added to prevent the formation of polymers[3].

Inductively Coupled Plasma RIE

Inductively coupled plasma (ICP) RIE is an enhanced version of the RIE technique. In ICP, the plasma is no longer generated solely by RF applied between two electrodes. Instead, a standalone RF coil is utilised to create a time-varying electromagnetic field and ionise reactant gases through inductive coupling (Fig. 3.7). An RF power is still applied to the lower electrode in order to attract and accelerate reactive ions towards the sample platter. Such a mechanism allows the independent control of plasma density and vertical ion bombardment hence enables better control of etching condition.

The ICP system used in this work is an Oxford Instruments Plasmalab System 100 (Fig. 3.7), which is employed mainly for GaN etching. Both the RIE and the ICP RF generators have a frequency of 13.56 MHz. Our typical etching conditions are the ICP power at 450 W and the RIE RF power are at 80 W. The etchant gases for GaN etching are Cl_2, which provides chemical reaction, and Ar, which supplies ions for physical bombardment. The flow rate is 15 sccm for Cl_2 and 4 sccm for Ar.

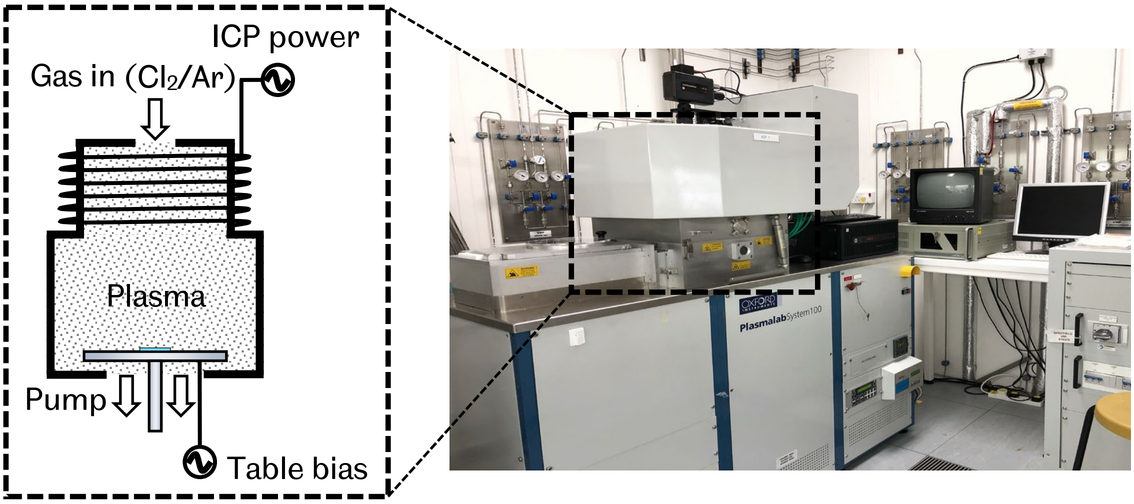

Figure 3.7. Schematic illustration of ICP and the Oxford Instrument Plasmalab System 100 ICP.

The etch depth and rate can be monitored using an interferometry endpoint system. In this system, a laser spot is focused on the sample surface, and the intensity of the reflected laser light is measured. As the sample is etched, due to the change of the interference cycle, a periodic oscillation will occur in the intensity of the reflected light. The etch depth and rate can then be estimated from this interference ripple. Theoretically, by knowing the laser wavelength, layer thickness, refractive index and reflectivity, a model of such oscillation can be calculated. However, in practice, as the samples etched in ICP almost always have microstructures fabricated on their surface, the real laser output is far from the theoretical model. Therefore, the real etch depth is studied empirically by matching the number of oscillation peaks and the measured thickness from structural characterisation. Under a typical condition, the empirical etch rate of GaN is 120 nm/minute and 60 nm/minute for AlN.

3.1.5 Template Fabrication

In this work, all the techniques mentioned above are utilised mainly for the fabrication of patterned template for overgrowth. The pattern can be micro-holes, micro-stripes or micro-rods with different sizes and configurations.

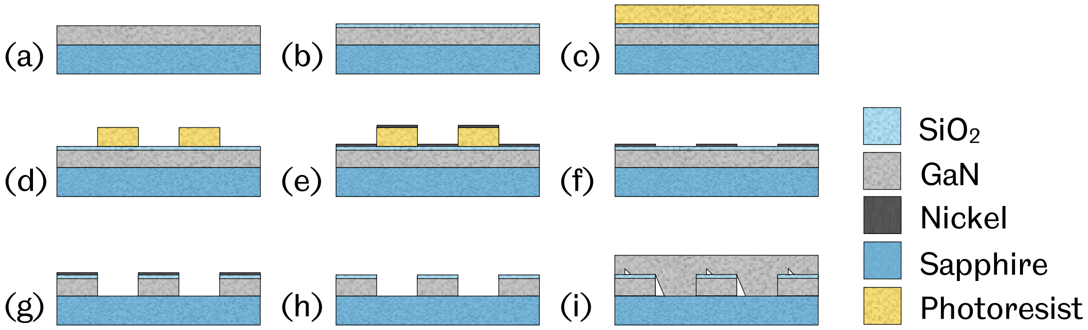

Figure 3.8. Schematic diagram of the fabrication procedure of a typical 2.5 μm micro-rod GaN template for overgrowth. Some structures (such as AlN buffer layer) are omitted in the diagram to avoid redundant details.

Figure 3.8 demonstrates our typical fabrication procedures of micro-rod GaN templates. As shown in Fig. 3.8a, the fabrication starts with an as-grown GaN template, which is grown using high AlN buffer technique[4]. The GaN layer thickness is ~ 1 μm (the 150 nm AlN buffer layer is not shown in Fig. 3.8). A layer of SiO_2 with a thickness of 150 nm serving as a mask is then deposited onto the as-grown template (Fig. 3.8b). A layer of HMDS promoter is then spin-coated, followed by a layer of photoresist, which is then patterned by using photolithography (Fig. 3.8c-d). The patterned template is then loaded into a thermal evaporator for depositing a layer of Ni with a thickness of ~60 nm (Fig. 3.8e). After a lift-off process, a Ni patterned template is completed for further dry etching (Fig. 3.8f). The template is then etched by RIE to remove exposed SiO_2 and then etched GaN down to sapphire by ICP, forming a micro-rod array structure with exposed sidewalls as growth planes (Fig. 3.8g-h). The Ni layer is then removed by aqua regia, leaving GaN micro-rods with SiO_2 blocking cap on top. The template is then treated with KOH PEC etching and put back into MOCVD for overgrowth (Fig. 3.8i).

3.2 Metal Organic Chemical Vapour Deposition

As discussed in chapter 2, all samples used in this thesis were grown using a Thomas Swan single chamber 3 x 2" vertical close-coupled showerhead (CCS) metal organic chemical vapour deposition (MOCVD) system. As shown in Fig. 3.9, the main body of the MOCVD system consists of two control panels, a gas delivery cabinet, a metal organic (MO) bubbler cabinet, a reactor cabinet, an in-situ monitor system, a load-lock chamber and an electrical distribution system. Apart from the main body, there are carrier gas purifiers, two cooling water systems as well as an exhaust system including an ammonia scrubber (not shown).

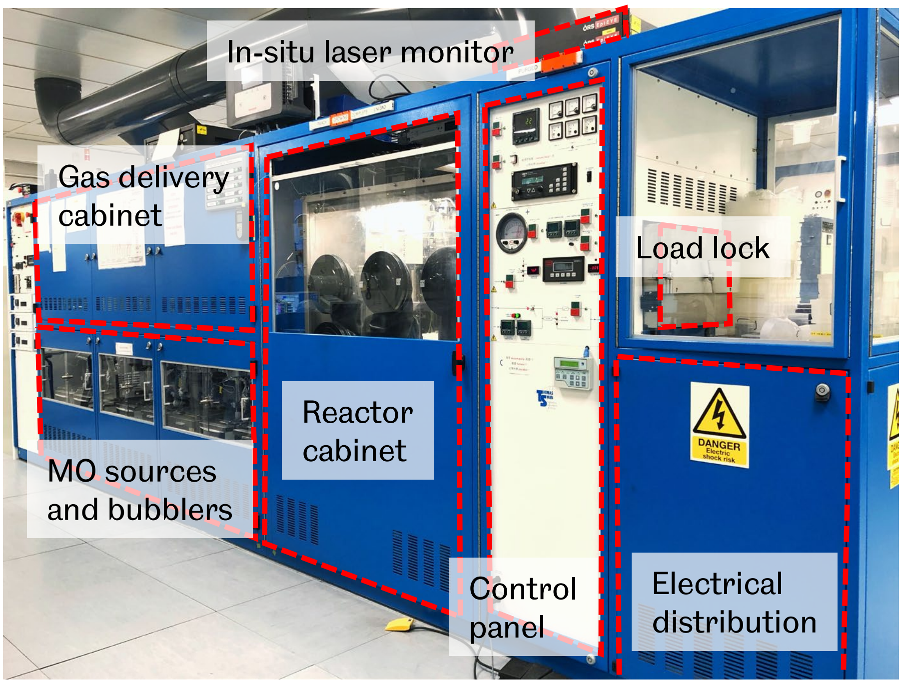

Figure 3.9. A Thomas Swan single chamber 3 x 2" vertical CCS MOCVD.

H_2 and N_2 are used as the carrier gases. Purification is therefore required for both types of carries gases before sending into the MOCVD system. While H_2 is purified by a heated palladium (Pd) membrane through permeation at 300 °C, N_2 is purified by chemical gettering to remove moisture, oxygen and CO_2[5]. As a result, H_2 has a much better purity and therefore is more frequently used as a carrier gas. N_2 is only used in InGaN quantum well (QW) growth as the H_2 ambient is detrimental to In incorporation.

Commonly used precursors include metal organic sources for group III elements, such as trimethylgallium (TMG), trimethylindium (TMI), and trimethylaluminum (TMA), ammonia (NH_3) for N element, disilane (Si_2H_6) for n-type doping and magnesocene (Cp_2Mg) for p-type doping. Figure 3.10 schematically demonstrates a gas circuit of the MOCVD gas delivery system. As shown in the figure, hydrides, including NH_3 and Si_2H_6, are directly supplied from cylinders outside the system. The NH_3 is N7.0 (99.99999%) ultra-pure grade, which is also known as "white ammonia"[6]. Two separate gas lines are used to carry group V precursor and group III precursors, respectively, in order to prevent any pre-reaction. MO stored in a bubbler can either be liquid or solid. Generally, TMG, TMA and TMI are liquid state source, while Cp2Mg is solid. However, TMI is also available in solid state. The bubblers are kept in water baths to maintain a constant temperature. When a MO source is required for the growth, a carrier gas will be flowed into the bottom of the bubblers and then bring MO content into the main gas lines.

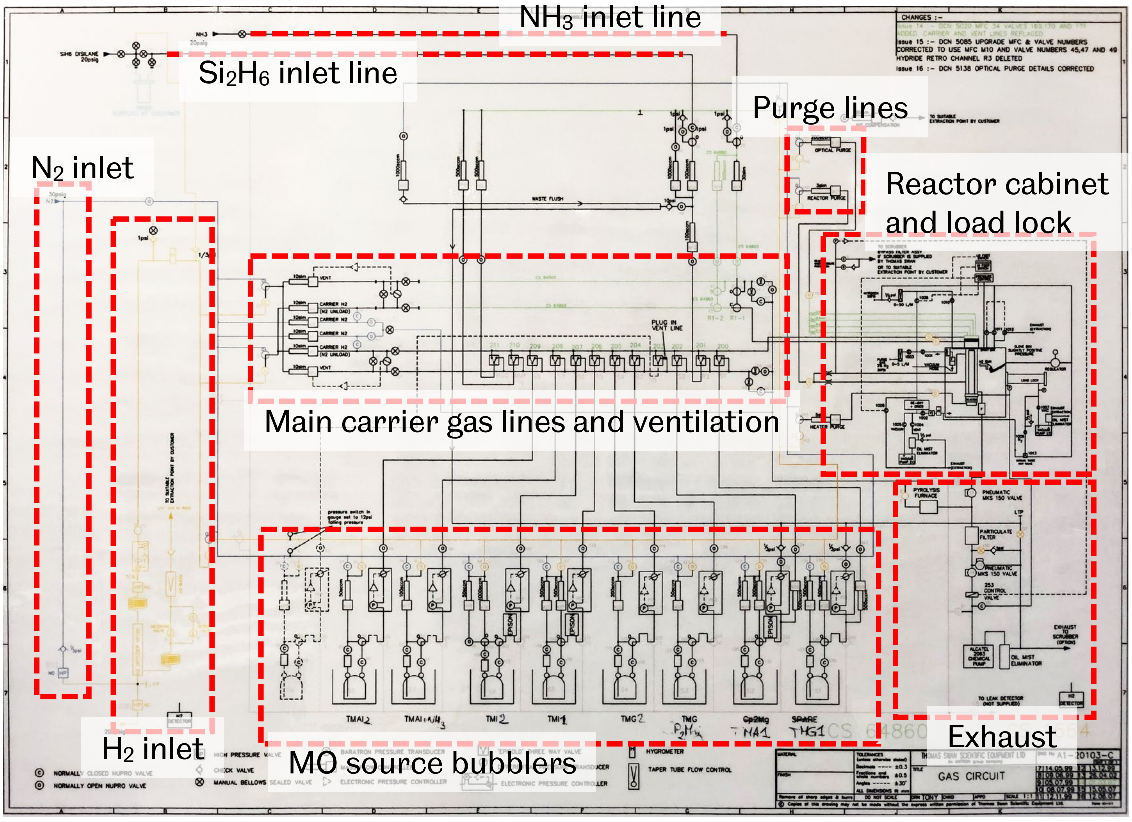

Figure 3.10. Schematic gas circuit of MOCVD gas delivery system.

During the growth, the MO and hydride precursors are fed into the growth chamber through a showerhead. Both the showerhead and stainless-steel chamber wall are water-cooled to prevent thermal damage during any high-temperature growth processes. The reactor is completely sealed and isolated from the outside environment by a double O-ring mechanism. Wafers stay on a SiC coated susceptor just below the showerhead and above a heater. The spacing between the showerhead 1.1 cm. The susceptor has three 2-inch pockets, which allow three samples to be grown simultaneously in a single growth run. The heating system consists of three zones, where each zone can be controlled independently in order to achieve a very good uniformity in temperature across the whole susceptor. At the centre of the heater, a thermocouple is mounted. An in-situ interferometry monitoring system is installed on top of the reactor to provide real-time feedback during growth. The monitoring system features three different lasers with wavelengths of 405 nm, 635 nm and 950 nm.

3.3 Characterisation Technique

3.3.1 Nomarski Microscopy

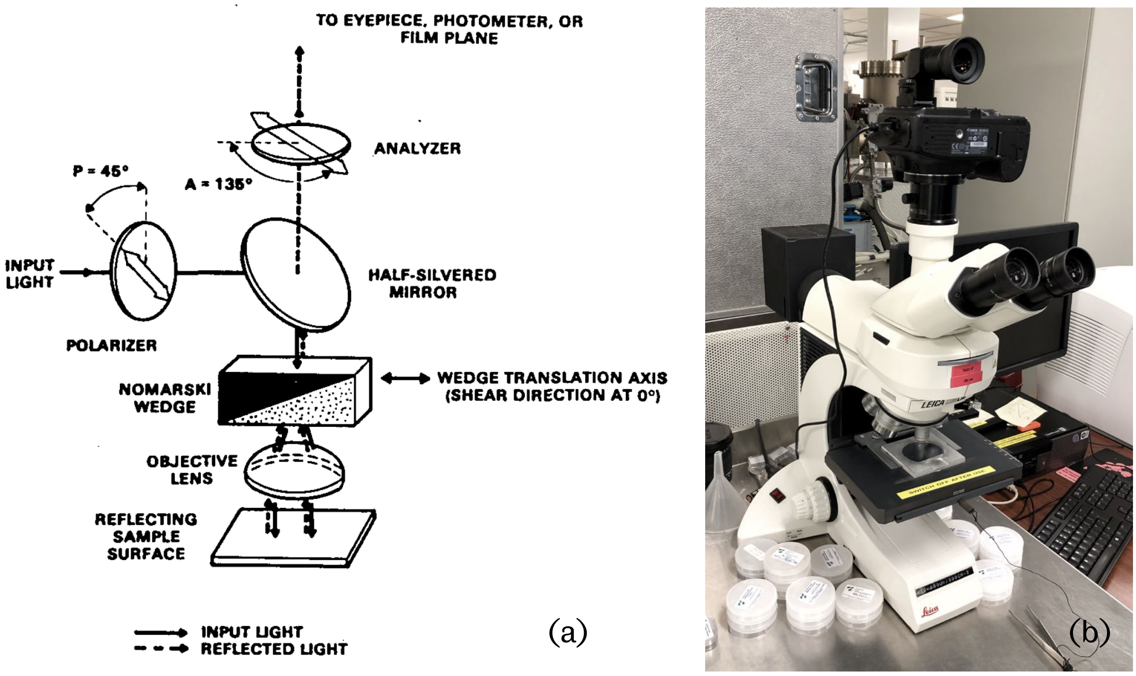

Figure 3.11. (a) schematic illustration of a Nomarski microscope, and (b) the Leica DMLM microscope. (a) reproduced with permission[7].

Nomarski microscopy, also known as differential interference contrast (DIC) microscopy, is an advanced optical microscopy. In addition to having general microscopy functions, which uses a set of lenses to magnify images of a testing object, DIC features the function of an optical interferometer, which uses the optical path difference of two beams of coherent light to improve image contrast and extract invisible information, such as the difference in thickness or refractive index. It is especially suitable for the characterisation of III-nitrides, as the III-nitride epilayers, as well as the sapphire substrate, are all transparent.

Figure 3.11a illustrates the working principle of a DIC. After unpolarised light enters the DIC, it becomes linearly polarised at 45°. The polarised light is then reflected by a semi-transparent mirror into a birefringent Nomarski prism and separated into two rays that are orthogonal to each other. The two rays are then focused by a condenser then projected onto a sample. As the two rays are almost identical but with different polarisation, the sample is now effectively illuminated by two rays of coherent light. The two light spots on the sample surface are separated by a shear component and overlap each other with an offset. If the illuminated area has a varied thickness or refractive index, the rays will experience different optical path lengths. These differences are then carried by the phases of two rays, which are then reflected back to the Nomarski prism and recombined into one ray of light with 135° linear polarisation. The interference between two rays during the recombination brightens or darkens the image according to the difference in the optical paths, hence revealing invisible features and improving the contrast. In this work, the DIC employed is a Leica DMLM microscope (Fig. 3.11b).

3.3.2 X-ray Diffraction

X-ray diffraction (XRD) is one of the major structural characterisation techniques for evaluating crystal structure. XRD has been widely used in semiconductor researches for the investigation of crystal quality, lattice parameters, alloy composition, layer thickness and strain state.

Principle

The principle of XRD can be understood by Bragg's diffraction. As shown in Fig. 3.12, in a crystal, atoms are arranged in a highly ordered structure forming crystal lattices. When X-rays are incident on the crystal, the crystal structure can act as a 3D grating, scattering incident X-rays from lattice planes. The X-rays scattered from the lower planes traverses extra path lengths. Since the wavelength of the X-ray is of the same order as the crystal interplanar distance (~ 1 Å), constructive interference will occur at a certain angle where the extra path length equal to an integer multiple of the wavelength. Such a relation can be expressed by Bragg's law:

$$2d \sin\theta = n\lambda \tag{3.2}$$

Where d is the interplanar distance, ϑ is the scattering angle, n is the order of diffraction, and λ is the X-ray wavelength. The interplanar distance, as well as the crystal structure, can therefore be probed by changing the scattering angle.

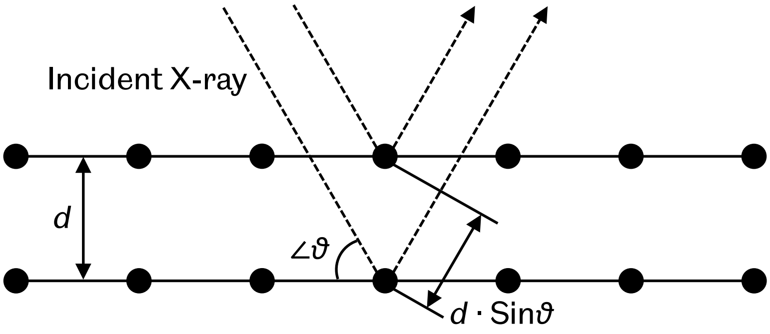

Figure 3.12. Schematic illustration X-ray diffraction and Bragg's law in a crystal structure.

X-ray diffractometer

In this work, the XRD characterisation is conducted by using a Bruker D8 X-ray diffractometer. As shown in Fig. 3.13, the diffractometer consists of three main modules: primary beam (i.e. incident beam) module, sample positioning module, and secondary beam (i.e. scattered beam) module. The X-ray is generated by an X-ray tube. In the X-ray tube, electrons are produced by a hot cathode through thermionic effect. As a high voltage is applied across the tube, the electrons are accelerated in the vacuum and become an electron beam. A piece of metal (anode) is then irradiated by a high-energy electron beam thus generating X-ray. In the case of Bruker D8, the anode is made up of copper (Cu) to generate Cu Kα X-ray radiation with a wavelength of 1.5418 Å. A typical current and acceleration voltage is 40 mA and 40 kV, respectively. The generated X-ray is then guided into the primary optics, which consists of a Goebel mirror, a divergence slit, a monochromator and a Soller slit. The X-ray is therefore filtered and collimated, becoming an X-ray beam with a symmetrical and narrow wavelength distribution. The X-ray is then directed to the sample stage, which is controlled by a goniometer. As the sample rotates in a scan, the X-ray scattered from the sample will be retrieved by the secondary optics, which serves the same purpose as the primary optics. The intensity of the diffracted X-ray is then recorded by the detector.

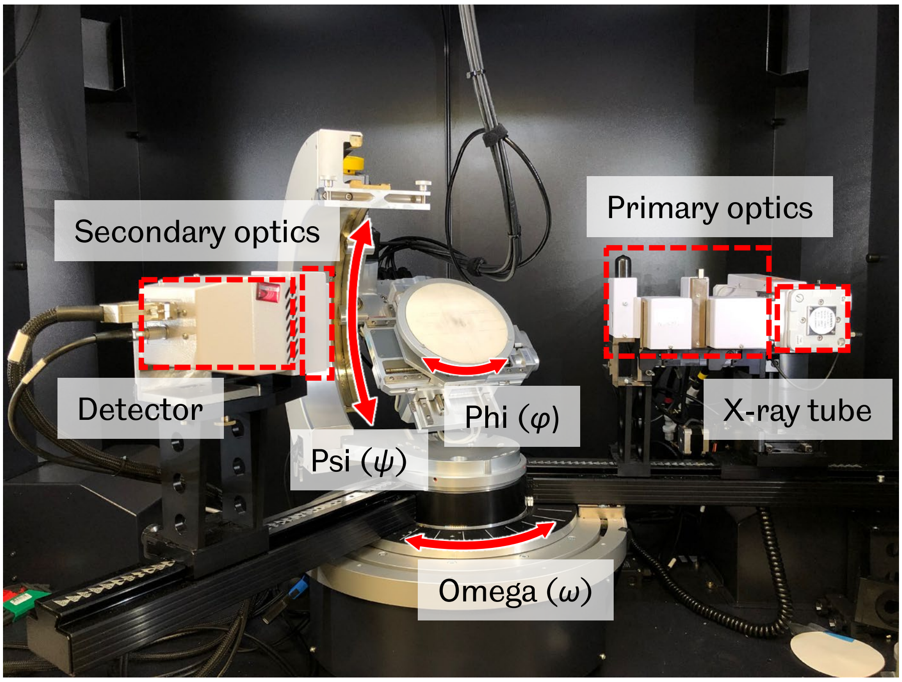

Figure 3.13. Schematic of the Bruker D8 X-ray diffractometer.

Scan Types

XRD scans have multiple types with various diffraction geometries. The Ewald sphere is often used to understand different scan types and geometries. As shown in Fig. 3.14, the Ewald sphere is constructed in reciprocal space, where each reciprocal lattice point represents a set of crystal planes as well as their corresponding diffraction spots. The scattering vector $\boldsymbol{S}$, which is the vector difference between the diffracted ($\boldsymbol{k}_h$) and incident ($\boldsymbol{k}_0$) beam vectors, is the effective "probe" for the investigation of crystal planes. During a scan, whenever the vector $\boldsymbol{S}$ lands on a diffraction spot, it means that the corresponding planes are being probed by the scan.

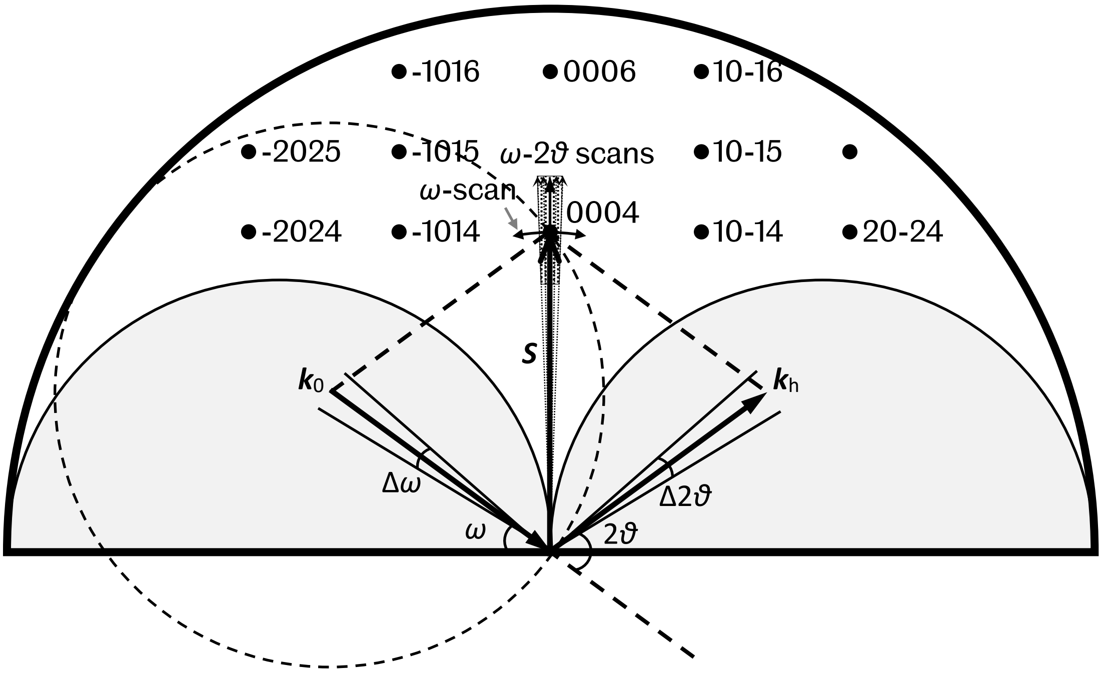

Figure 3.14. An Ewald sphere of a c-plane GaN epilayer in reciprocal space. The length of the diffracted ($\boldsymbol{k}_\mathrm{h}$) and incident ($\boldsymbol{k}_0$) beam vectors equals to $1/\lambda$. Some diffraction spots are omitted to reduce redundant details. The vectors of ω-scan and ω-2ϑ scan are shown around the (0004) spot. The dotted inverted trapezoid area represents an on-axis RSM composed by multiple ω-2ϑ scans. Adapted with permission[8].

The Ewald sphere in Fig. 3.14 described the accessible reciprocal lattice points of symmetric and asymmetric scans (Fig. 3.15a-b) of a c-plane GaN sample at a certain azimuth angle (the projection of incident X-ray beam on the sample surface is perpendicular to the m-plane.). The two grey semicircle areas represent inaccessible regions where either the incident or the diffracted beam is blocked by the sample itself. To access these areas, as well as other reciprocal lattice points which are not included in Fig. 3.14, the sample can be rotated by 90° in φ with a ψ offset added to give a skew symmetry scan (Fig. 3.15c). In some extreme cases, planes perpendicular to the sample surface can also be accessed, by using a very small grazing incident angle, or by cleaving the sample and using zero incident angle. These methods are called in-plane diffraction or edge symmetry scan (Fig. 3.15d).

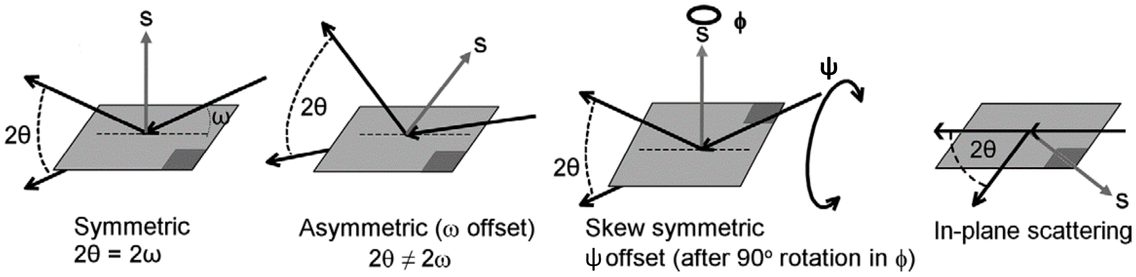

Figure 3.15. Common diffraction geometries of XRD scans. Reproduced with permission[8].

In this work, three types of scans are frequently used, which are ω-scan, ω-2ϑ scan, and reciprocal space mapping (RSM).

ω-scan, also termed as x-ray rocking curve (XRC) measurement, is an effective method to determine crystal quality. In ω-scan, the source and detector remain stationary, while the sample rocks about the ω-axis. In reciprocal space, the direction of the scattering vector $\boldsymbol{S}$ changes, while the length of the scattering vector remains unchanged (Fig. 3.14). When the diffraction spot is scanned by the arc, the broadening of the spot is measured. As the broadening is directly related to the dislocations, surface mosaicity and wafer curvature, the crystal quality is therefore determined.

ω-2ϑ scan is an effective method to probe paralleled crystal planes of different material with different lattice parameters. It is therefore very useful in the characterisation of layer structures as well as alloy compositions. In ω-2ϑ scan, the detector rotates twice as much as the sample, i.e. $\Delta 2\vartheta = 2\Delta\omega$. In reciprocal space, the length of scattering vector $\boldsymbol{S}$ changes, while the direction remains unchanged (Fig. 3.14). Therefore, multiple diffraction spots along a line can be included in a single ω-2ϑ scan.

If a series of ω-2ϑ scan with successive ω-offset are measured, these scans can then be combined into a map (Fig. 3.14). This process is termed as RSM. The output of RSM is a 3D map of diffraction intensity projected into a 2D area in reciprocal space, which contains all the information of multiple ω-scans and ω-2ϑ scans in that area. Therefore, RSM is very useful in the determination of strain state and crystal quality.

3.3.3 Scanning Electron Microscopy

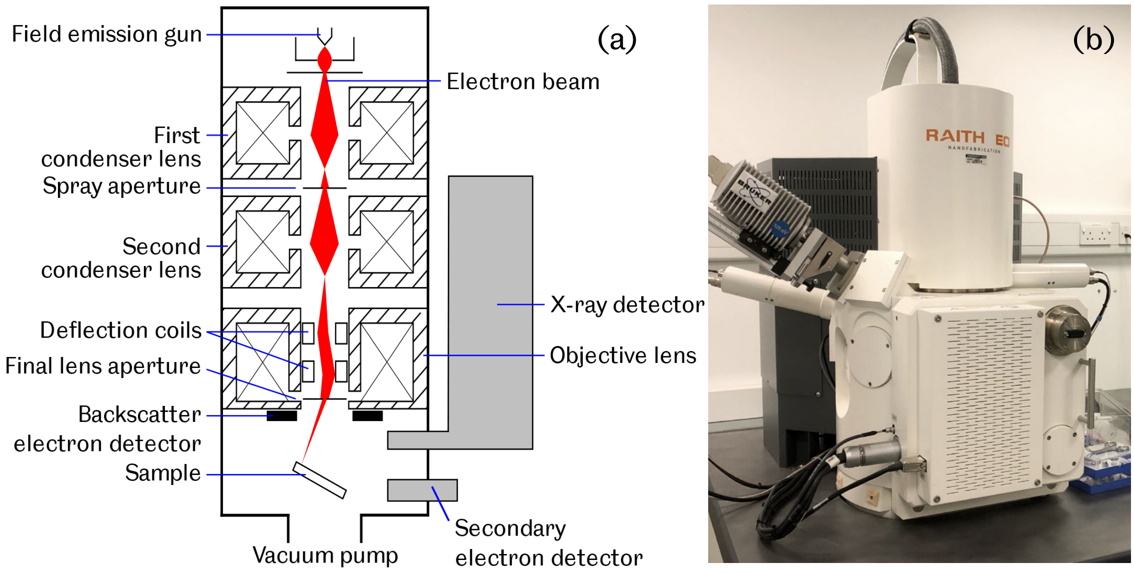

Figure 3.16. (a) schematic diagram of a typical FEG-SEM, and (b) a Raith 150 EBL based SEM system. (a) adapted with permission[9].

Scanning electron microscopy (SEM) is employed to investigate sub-micron structures and nanofeatures involved in this work. As SEM uses an electron beam instead of visible light as the illumination source, it can produce images with a high resolution far beyond the limitation of a normal optical microscope. As shown in Fig. 3.16a, SEM operates under a high vacuum environment. A field emission gun (FEG) is utilised to generate an electron beam by applying a strong electrostatic field and thus removing electrons from the emitter. The generated electron beam then passes through a series of magnetic condensers and be focused onto a sample. A set of deflection coils are used to control the beam. The SEM system used in this work is reconfigured from a Raith 150 electron-beam lithography (EBL) system (Fig. 3.16b).

The electrons generated by SEM are termed as primary electrons. When the primary electrons penetrate the surface of a sample and interact with the sample, they lose energy through a variety of mechanism. The lost energy is then converted into other forms and produces various signals, among which, four types of signal are commonly assessed to characterise the sample, which are:

- Backscattered electrons (BSE). These are the electrons reflected back from a sample due to elastic scattering. As they have high energy and move fast along a straight line, the BSE detector is therefore placed directly above the sample. Additionally, since the scattering is strongly determined by the size of nuclei, BSE is commonly used to reveal and improve the contrast of different elemental compositions.

- Secondary electrons (SE). These are electrons generated by primary electrons from a sample surface. Consequently, SE is very useful in revealing the surface morphology and topography. As SE have low energy and travel slowly, a positively charged SE detector is usually used to capture them.
- X-ray emission. In some cases, the electrons generated by primary electrons are from the inner shell of atoms. Due to the absence of these electrons, holes are created and soon be filled by other electrons from the high energy outer shell, leading to X-ray emission. Since each element has a unique electron configuration corresponding to a unique signature emission spectrum, the X-ray emission can therefore be used to identify elemental composition through energy-dispersive X-ray (EDX) analysis.
- Light emission. This is also known as cathodoluminescence (CL), which is very useful in the study of optical properties. It can be used to perform CL measurement on a nanometre scale, which is similar to PL but with a high spatial resolution

3.3.4 Transmission Electron Microscopy

Unlike SEM, which is based on scattered or re-emitted signals, TEM uses transmitted electrons to perform microstructure investigation. Prior to the TEM measurement, the thickness of a sample must be reduced down to <100 nm by mechanical lapping/polishing and then ion milling in order to allow electrons to pass through the specimen. TEM has two basic operation modes. In a diffraction mode, the diffraction patterns are collected, which can be used to identify crystal orientation, structure, and defects. In an imaging mode, selected electron signals are collected. These signals can either from the transmitted (bright field), or scattered electrons (dark field).

In this work, bright field imaging is used to investigate crystal defects in epilayers. As defects can greatly intensify the scattering of electrons, dark spots or dark lines will be generated around the defects in bright field images, giving a visualised output of defects. Additionally, as most defects are crystal orientation dependent, the type of defects can also be distinguished by changing the measurement angles. The system used in this work is a Philips EM 430 TEM, which features an acceleration voltage of 50 to 300 kV, 800,000x magnification, and a point resolution down to 3Å.

3.3.5 Photoluminescence

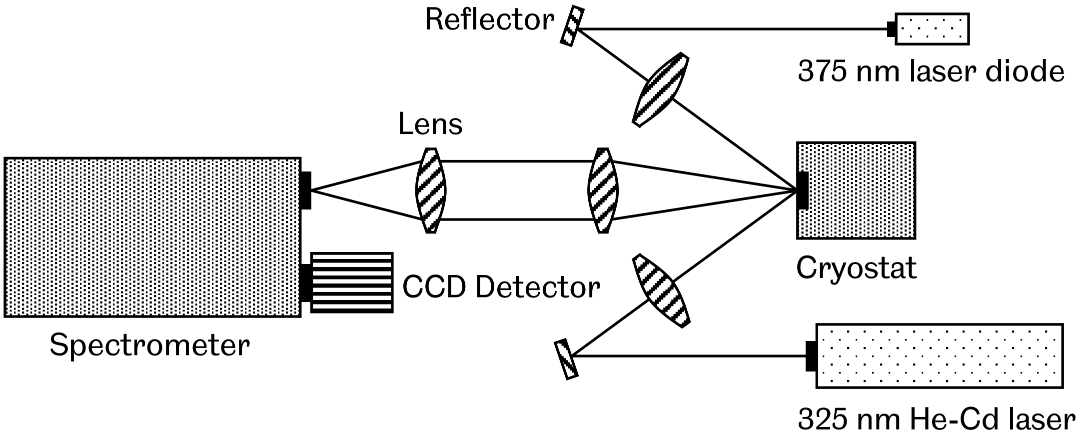

Figure 3.17 Schematic illustration of the custom-built PL system.

Photoluminescence (PL) is one of the most powerful techniques for optical characterisation. In this work, a home-made PL system is employed to characterise the optical properties of III-nitrides (Fig. 3.17). The system features two excitation sources, a Kimmon 325 nm He-Cd laser, and a Vortran Stradus 375 nm laser diode. The reflector used is an optimised Aluminium coated mirror with a high reflectivity of >99% at the wavelength between 300 nm to 550 nm. The laser beam focused on a sample surface has a spot diameter of ~200 µm. The sample is held in a stage within a helium (He) closed loop cryostat, which allows the sample temperature to be adjusted from 10K to 300K, enabling the measurement of low-temperature and temperature-dependent PL. A pair of lenses are used to collect and focus the PL emission into a Horiba SPEX 500M spectrometer, which utilises a blazed holographic grating for optical dispersion. The dispersed emission signal is then collected by a Horiba Syncerity thermoelectrically (TE) cooled charge-coupled device (CCD) detector.

3.3.6 Confocal Microscopy

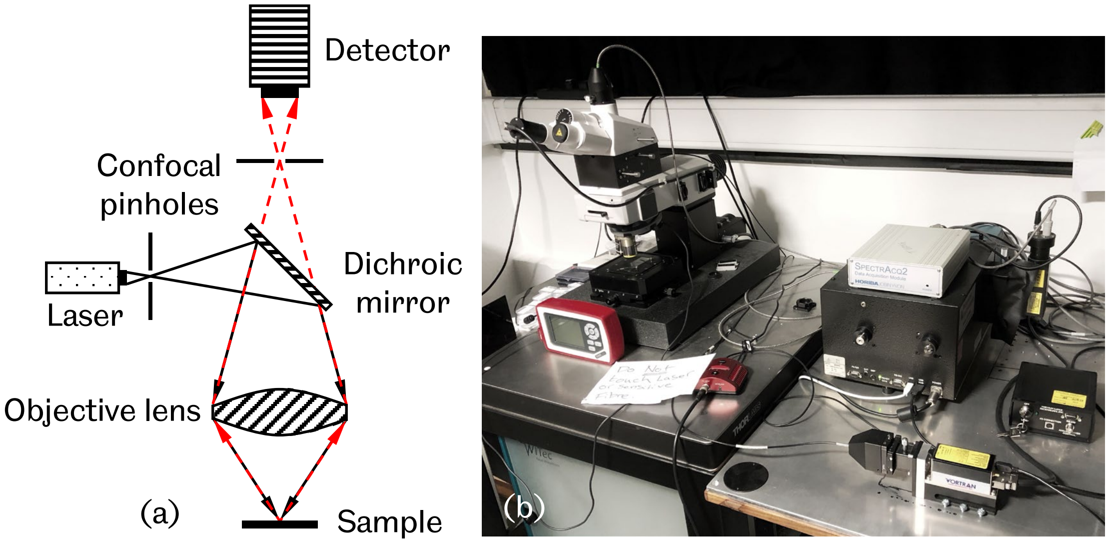

Figure 3.18. (a) schematic illustration of a confocal microscope, and (b) the WITec 300R confocal microscopy system.

Confocal microscopy is an optical characterisation technique that utilities two confocal pinholes to measure a tiny spot area of a sample. The implication of the term "confocal" is that both illumination and detection are focused to the same spot. As shown in Fig. 3.18a, a laser beam is focused by a source pinhole aperture in order to generate a diffraction-limited light spot with perfectly round shape. The light spot is then focused by an objective lens onto a focal plane where a sample is illuminated. The reflection and the emission are then collected by the same objective lens, pass through the dichroic mirror and finally focused onto a detector pinhole aperture. As a result, any emission from the out-of-focus plane or scattering can be removed. Confocal microscopy is therefore a very useful technique for performing PL mapping with a high spatial resolution.

Figure 3.18b shows our WITec 300R confocal microscopy system employed in this work. The excitation source is a Vortran Stradus 375 nm diode laser. The emission signal is dispersed by a Princeton Instruments Acton SP2300 monochromator before recorded by a TE-cooled Andor Newton CCD. The lateral resolution of the system, $\text{FWHM}_{\text{lateral}}$, is given by Rayleigh criterion[10]:

$$\text{FWHM}_{\text{lateral}} = 0.37\frac{\lambda^*}{\text{NA}} \tag{3.3}$$

Where NA is the numerical aperture of the objective lens, which is 0.95 in this case, and:

$$\lambda^{*} \approx \sqrt{2}\frac{\lambda_{\mathrm{exc}}\lambda_{\mathrm{em}}}{\sqrt{\lambda_{\mathrm{exc}}^{2}+\lambda_{\mathrm{em}}^{2}}} \qquad (3.4)$$

λ^* is the mean wavelength of the system, which takes both excitation wavelength λ_{exc} and emission wavelength λ_{em} into account. For example, for the measurement of an InGaN/GaN QW structure at 420 nm gives an approximate lateral resolution of 154 nm.

Reference

1. Zhuang, D. & Edgar, J. H. Wet etching of GaN, AlN, and SiC: A review. *Mater. Sci. Eng. R Reports* **48**, 1–46 (2005).

2. The Dow Chemical Company. Material Safety Data Sheet MEGAPOSIT^{TM} MF^{TM} -26A DEVELOPER. (2012).

3. Takahashi, K., Hori, M. & Goto, T. Fluorocarbon radicals and surface reactions in fluorocarbon high density etching plasma. II. H 2 addition to electron cyclotron resonance plasma employing CHF 3. *J. Vac. Sci. Technol. A Vacuum, Surfaces, Film.* **14**, 2011–2019 (1996).

4. Bai, J. *et al.* Optical properties of AlGaN/GaN multiple quantum well structure by using a high-temperature AlN buffer on sapphire substrate. *J. Appl. Phys.* **99**, 0–4 (2006).

5. Matheson. Complete Purification Solutions with NANOCHEM® Purifiers. (2013). Available at: https://www.mathesongas.com/pdfs/products/NANOCHEMPurificationSolutions.pdf. (Accessed: 20th May 2019)

6. Air Products. Ammonia (NH3). (2015). Available at: http://www.airproducts.com/~/media/downloads/a/ammonia-nh3/data-sheets/en-led-ammonia-white-datasheet.pdf?productType=Gases&productLevel1=Specialty-Gases&productLevel2=Silicon-Semiconductors&productLevel3=Ammonia-NH3. (Accessed: 20th May 2019)

7. Hartman, J. S., Gordon, R. L. & Lessor, D. L. Quantitative surface topography determination by Nomarski reflection microscopy 2: Microscope modification, calibration, and planar sample experiments. *Appl. Opt.* **19**, 2998 (2008).

8. Moram, M. A. & Vickers, M. E. X-ray diffraction of III-nitrides. *Reports Prog.*

Phys. **72**, (2009).

9. MarcoTolo. File:Schema MEB (en).svg. (2015). Available at: https://commons.wikimedia.org/wiki/File:Schema_MEB_(en).svg. (Accessed: 20th May 2019)

10. Wihelm, S., Grobler, B., Gluch, M. & Heinz, H. Confocal Laser Scanning Microscopy Principles. *ZEISS Jena* (2000). Available at: http://zeiss-campus.magnet.fsu.edu/referencelibrary/pdfs/ZeissConfocalPrinciples.pdf. (Accessed: 20th May 2019)

Chapter 4

Overgrowth and Strain Investigation of (11-20) Non-polar GaN on Patterned Templates on Sapphire

---

Non-polar (11-20) GaN with significantly improved crystal quality has been achieved by means of overgrowth on regularly arrayed micro-rod templates on sapphire in comparison with standard non-polar GaN grown without any patterning processes on sapphire. Our overgrown GaN shows massively reduced linewidth of X-ray rocking curves with typical values of 270 arcsec along the [0001] direction and 380 arcsec along the [1-100] direction, which are among the best reports. Detailed X-ray measurements have been performed in order to investigate strain relaxation and in-plane strain distribution. The study has been compared with the standard non-polar GaN grown without any patterning processes and an extra non-polar GaN sample overgrown on a standard stripe-patterned template. The standard non-polar GaN grown without involving any patterning processes typically exhibit highly anisotropic in-plane strain distribution, while the overgrown GaN on our regularly arrayed micro-rod templates shows a highly isotropic in-plane strain distribution. Between them is the overgrown non-polar GaN on the stripe-patterned template. The results presented demonstrate the major advantages of using our regularly arrayed micro-rod templates for the overgrowth of non-polar GaN, leading to both high crystal quality and isotropic in-plane strain distribution, which is important for the further growth of any device structures.

4.1 Introduction

There is a significantly increasing demand on III-nitride based power electronics and radio-frequency (RF) devices required for 5G mobile communications, as GaN exhibits major advantages in fabricating high power, high frequency and high temperature devices due to its intrinsically high breakdown voltage, high saturation electron velocity and excellent mechanical hardness[1,2]. So far, the development of III-nitride electronics is built on AlGaN/GaN heterostructure field transistors (HFETs) grown on *c-plane* GaN surface[3,4]. This polar orientation poses strong polarisation at the interface between AlGaN and GaN, leading to a high sheet carrier density of up to $10^{13}/\text{cm}^2$ obtained without modulation doping as a result of spontaneous and piezoelectric polarisation[5,6]. On the one hand, this is the major advantage for III-nitride electronics grown on *c-plane* GaN surface. On the other hand, such polarisation generally leads to a depletion-mode transistor as a consequence, while it is ideal to obtain enhancement-mode devices in practical applications due to safety requirements. Any change in strain would also affect the electrical performance of such HFETs, for instance, SiN deposition required for surface passivation, which could potentially lead to degradation in performance or even reliability issues[7-9]. Furthermore, the sheet carrier density of a two-dimensional electron gas (2DEG) formed at the interface between GaN and AlGaN sensitively depends on the polarisation, and thus cannot be simply tuned in a controllable manner as required.

Based on the well-established experience built on the growth and fabrication of AlGaAs/GaAs high electron mobility transistors (HEMTs), a simple but promising solution is to grow an AlGaN/GaN heterostructure with modulation doping along a non-polar direction, where the polarisation can be eliminated and thus the sheet carrier density of 2DEG can be tuned simply through optimising the doping level in AlGaN barrier[6].

However, the crystal quality of current non-polar GaN grown on either sapphire or silicon is far from satisfactory. Typically, non-polar GaN grown on sapphire without any extra processes exhibits a high density of defects (a dislocation density of above $10^{10}/\text{cm}^2$ and a stacking fault density of above $10^6/\text{cm}$)[10,11].

Therefore, it is crucial to develop a new method for the growth of non-polar GaN on sapphire or silicon substrates, the industry-compatible substrates.

Previously, we developed a cost-effective approach for the overgrowth of (11-22) semi-polar GaN on *m-plane* sapphire by using regularly arrayed micro-rod templates, leading to substantial improvement on crystal quality. By using the semi-polar GaN templates, we have achieved high performance light emitting diodes (LEDs) with longer emission wavelengths such as green and amber[12-15]. We further extend this approach to the overgrowth of non-polar (11-20) GaN on *r-plane* sapphire, aiming to significantly improve the overall performance of non-polar GaN including crystal quality and strain situation that is a typical issue for GaN grown on large lattice-mismatched substrates. The strain issues of non-polar GaN grown on any foreign substrates such as sapphire or silicon are much more complicated than those of its *c-plane* counterpart. Non-polar GaN grown on large lattice-mismatched substrates intrinsically exhibits a strongly anisotropic in-plane strain distribution due to the absence of six-fold-symmetry. In return this anisotropic in-plane strain distribution leads to anisotropy in electrical performance and also challenges in device fabrication[16]. Furthermore, it is much more complicated to precisely determine the lattice parameters of non-polar GaN than its *c-plane* counterpart[17-21]. The strain of any overgrown non-polar GaN also depends on the patterned templates employed for conducting the overgrowth, as any residual voids left as a consequence of overgrowth processes lead to strain relaxation. This offers a great opportunity to redistribute strain or even eliminate strain.

In this work, we present a detailed study of strain relaxation of our (11-20) non-polar GaN with high crystal quality which has been achieved by means of overgrowth on our regularly arrayed micro-rod templates. Detailed X-ray measurements along symmetric and skew-symmetric directions have been employed for the study. For comparison, we have also performed overgrowth of non-polar GaN on a standard stripe-patterned template which is typically used for GaN overgrowth and then have studied its strain relaxation as well. Our results indicate that the overgrown GaN on our regularly arrayed micro-rod templates exhibits a highly isotropic in-plane strain distribution, while standard non-polar

GaN grown without any patterning processes on sapphire exhibits a strongly anisotropic in-plane strain distribution. Between them is the overgrown GaN on the stripe-patterned template in terms of in-plane strain distribution. We have also presented the evolution of the surface morphology and the crystal quality of the overgrown non-polar GaN on our regularly arrayed micro-rod templates. Of course, the results presented have also confirmed significantly improved crystal quality of the (11-20) non-polar GaN overgrown on our regularly arrayed micro-rod templates.

4.2 Template Fabrication and Overgrowth

A single (11-20) non-polar GaN layer with a thickness of 1 μm is initially grown on *r-plane* sapphire using our high temperature AlN buffer approach by a low-pressure metalorganic vapour phase epitaxial (MOVPE) technique[22], labelled as "as-grown" template. Subsequently, a 150 nm SiO_2 film is deposited on the as-grown template by using a standard plasma enhanced chemical vapour deposition (PECVD) technique, and then the SiO_2 film is fabricated into regularly arrayed micro-rods with a micro-rod diameter of 2.5 μm by means of a standard photolithography technique and then dry etching processes using a reactive ion etching (RIE). The regularly arrayed SiO_2 micro-rods are served as a second mask to finally etch the GaN layer underneath into regularly arrayed GaN micro-rods by using a standard inductively coupled etching (ICP) system. The GaN etching is performed down to the sapphire substrate. Each SiO2 micro mask formed remains on top of each GaN micro-rod.

Figure 4.1 shows a typical scanning electron microscopy (SEM) image of our regularly micro-rod array template which exhibits a chess-board configuration. The diameter of each micro-rod is 2.5 μm. It is well-known that the overgrowth of semi- or non- polar GaN along the [0001] direction, i.e., c direction, leads to being defect-free, while the overgrowth along the opposite direction (i.e., -c direction) allows defects to effectively penetrate to any overlying layers[13-15]. Therefore, it is essential to ensure that the growth along the c direction is dominant and that the growth along the -c direction can be effectively suppressed. This can be achieved by optimising growth conditions such as increasing growth temperatures. Our unique pattern configuration is expected to not only enhance improvement in crystal quality, but also help compensate the intrinsically anisotropic growth rate of non-polar GaN, leading to quick coalescence and then a smooth surface.

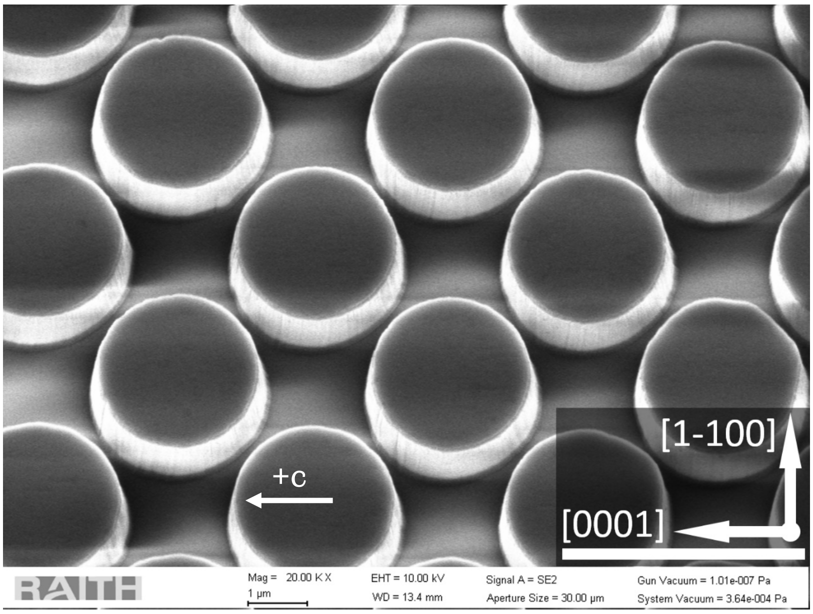

Figure 4.1. Plane-view SEM image of our regularly arrayed micro-rod array template. Scale bar: 4 µm.

For the fabrication of a standard stripe-patterned template[23,24], (11-20) non-polar GaN stripes with a width of 1.5 µm and a spacing of 1.5 µm between stripes are formed. These parallel stripes formed orientate along the [1-100] direction, which is perpendicular to the c direction of (11-20) non-polar GaN. Similarly, the etching is also performed down to the sapphire substrate, and the formed SiO_2 strip mask remains on top of each GaN stripe.

In each case, prior to any overgrowth the patterned GaN templates further undergo photo-enhanced chemical (PEC) etching using 10% potassium hydroxide (KOH) in order to partially remove GaN from the [000-1] direction which is nitrogen-face, while the Ga-face GaN from the [0001] direction, i.e., c direction, remains almost un-etched. The PEC etching does not etch SiO_2 masks. As a result, the GaN micro-rods are finally formed into a mushroom configuration as shown in Figure 4.2. By using the micro-rod arrays with a mushroom configuration, the overgrowth along the [000-1] direction can be effectively suppressed, thus reducing the penetration of defects significantly. Therefore, it is expected that this mushroom configuration leads to further improvement in crystal quality. Finally, the regularly arrayed micro-rod template is reloaded into the MOVPE chamber for overgrowth. For the present study, the overgrowth has been performed on the regularly arrayed micro-rod templates under identical conditions except growth temperatures. The overgrown samples are grown at 1100 °C, 1120 °C and 1140 °C, labelled as A, B and C, respectively. For comparison, the overgrowth on the standard stripe-patterned template has also been conducted under identical conditions at 1100 °C, denoted as D.

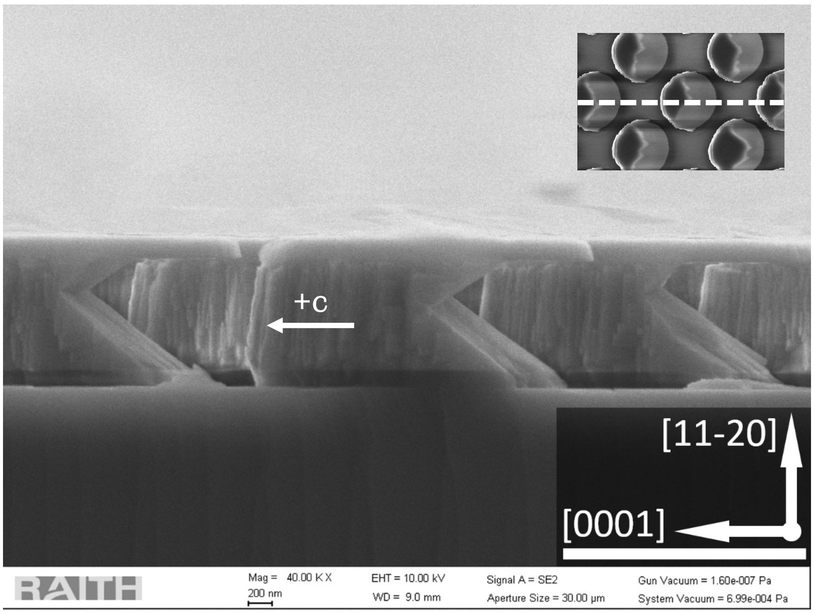

Figure 4.2. Cross-sectional SEM image of our micro-rod with a “mushroom” configuration. Scale bar: 2 µm. Inset: cross-sectional cutting configuration.

4.3 Result and Discussion

Figure 4.3 shows the plane-view SEM images of the overgrown GaN on our micro-rod template as a function of overgrowth time from 1000 to 8000 seconds, demonstrating its surface evolution and its coalesce processes. Figure 4.3a indicates that the overgrowth initiates mainly along the [0001] direction (i.e., c direction) and partially along the [1-100] and [-1100] directions, while the overgrowth along the [000-1] direction (i.e., -c direction) has been effectively suppressed.

During the first 1000 seconds, the overgrown GaN exhibits a truncated triangular prism around each micro-rod. These truncated triangular prisms have partly merged with each other, indicating that the first coalescence starts to occur before 1000 seconds. The first coalescence process completes before 2000 seconds as shown in Fig. 4.3b, where the gap between the micro-rods have been completely filled due to lateral overgrowth, and the vertical overgrowth has become dominant. The second coalescence happens once the lateral growth starts to extend to above the SiO2 masks. During this process, multiple semi-polar facets are generated as shown in Fig. 4.3c. Figure 4.3d to 4.3f show that full coalescence can be gradually completed after 5000 seconds, finally forming a smooth surface.

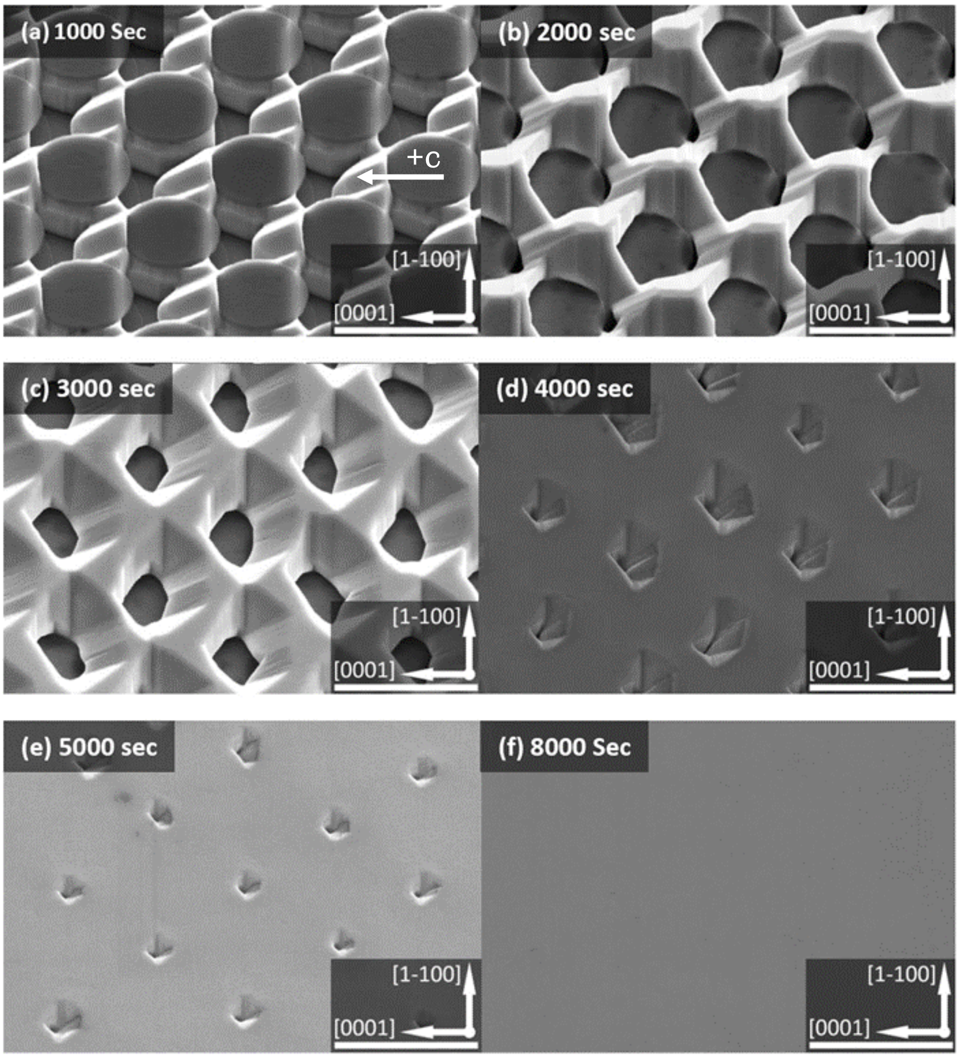

Figure 4.3. Plane-view SEM images of the nonpolar GaN overgrown on our regularly arrayed micro-rod array template as a function of growth time from 1000 to 8000 seconds. Scale bar: 4 µm.

High resolution X-ray diffraction measurements have been performed on all the samples as a function of azimuth angle in order to evaluate the crystal quality of non-polar GaN. Due to the anisotropic nature of non-polar GaN, it is necessary to measure the full width at half maximum (FWHM) of an XRD rocking curve as a function of azimuth angle. The azimuth angle is defined as 0° when the projection of an incident x-ray beam on a non-polar (11-20) GaN surface is parallel to the c direction of (11-20) GaN, while it is defined as 90° when the projection of the incident x-ray beam is along the [1-100] direction, i.e., m direction.

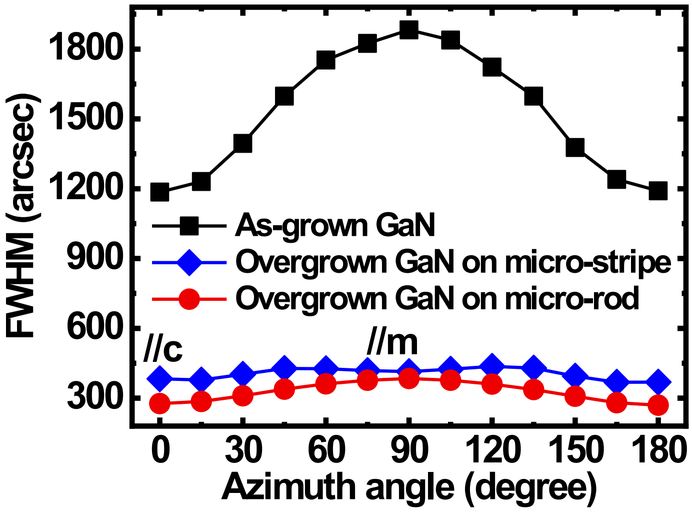

Figure 4.4. FWHM of the (11–20) on-axis XRD rocking curves as a function of azimuth angle for the as-grown sample, the overgrown GaN on our regularly arrayed micro-rod template, and the overgrown GaN on the standard stripe-pattern template.

Figure 4.4 shows the FWHMs of the on-axis XRD rocking curves of the two overgrown samples (one on our regularly micro-rod array template and another on the standard stripe-patterned template) as a function of azimuth angle from 0° to 180°. For comparison, Figure 4.4 also includes the data of the as-grown template. For any non-polar (11-20) GaN, the smallest FWHM typically appears at the 0° azimuth angle, while the largest FWHM is normally at the 90° azimuth angle.

Figure 4.4 shows that the as-grown GaN template typically exhibits very large FWHMs along both the [0001] and the [1-100] directions, which are 1180 and 1880 arcsec, respectively. In remarkable contrast, the overgrown GaN on our regularly arrayed micro-rod template exhibit a massive reduction in FWHM of XRD rocking curve, which has been down to 270 arcsec along the [0001] direction and 380 arcsec along the [1-100] direction, respectively. These values are the best report for (11-20) non-polar GaN on sapphire so far, demonstrating significant improvement in crystal quality. Our detailed transmission electron microscopy measurements indicate that the dislocation density has been reduced from ~10^{11}/cm^2 for the as-grown template to ~6 × 10^8/cm^2 for our overgrown sample.

The overgrown sample with a similar thickness on the standard stripe-patterned template shows broader FWHMs of XRD rocking curves than those of the overgrown samples on our regularly arrayed micro-rod templates. They are 380 arcsec along the [0001] direction and of 420 arcsec along the [1-100] direction, respectively. The above data demonstrate the advantage of using our regularly arrayed micro-rod template for the overgrowth of (11-20) non-polar GaN on *r-plane* sapphire.

In order to study strain distribution, x-ray reciprocal space mapping (RSM) measurements have been carried out on all the samples. The RSM has been measured on an asymmetric plane, i.e., the (11-22) plane, where the lattice constants for both the in-plane and the out-of-plane can be measured simultaneously.

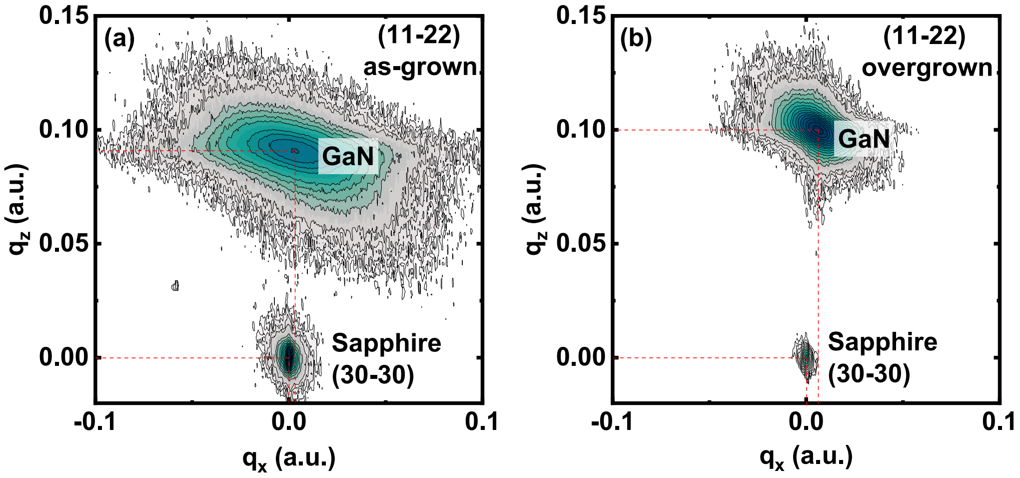

Figure 4.5. RSM of (a) the as-grown sample, and (b) the overgrown sample on our regularly arrayed micro-rod template.

Figure 4.5 shows the typical (11-22) RSM of the as-grown sample and the overgrown sample on our regularly arrayed micro-rod template, where the sapphire substrate is used as a reference. The sapphire substrate is 430 μm thick and is much thicker than any epitaxial layers. The coordinates of q_x and q_z represent the interplanar spacing along the in-plane [0001] direction and the out-of-plane [11-20] direction, which are proportional to $1/c$ and $1/a$, respectively. c represents the in-plane lattice constant, while a is the lattice constant along the vertical direction. Figure 4.5 indicates that the overgrown GaN exhibits smaller c and a in comparison with an unstrained case, demonstrating that the overgrown GaN suffers from compressive strain along the [0001] direction. However, it is not enough to only use the data obtained along the [0001] direction to investigate the anisotropy of the in-plane strain distribution of (11-20) non-polar GaN. The RSM data along the m direction which is perpendicular to the [0001] direction is also necessary. Unfortunately, due to the absence of the XRD peak of *r-plane* sapphire along this particular direction, there is not a sapphire reference for this direction.

Alternatively, the in-plane strain of (11-20) GaN can be studied by means of performing XRD measurements in a *ω/2ϑ* mode, where multiple symmetric and skew-symmetric reflections can be obtained. Unlike *c-plane* GaN, due to reduced symmetry (11-20) GaN exhibits anisotropic biaxial strain which results in an orthorhombic distortion. This leads to a great challenge in precisely determining lattice constants[17-21]. Therefore, an approach developed by Laskar *et al.* can be used to accurately determine the lattice constants, where they take the distortion into account and then use the least-square method for error-minimization[21]. In our case, we first measure the interplanar spacing (labelled as *d*hkl) of a number of planes of non-polar GaN, which are (11-20), (2-1-10), (11-22), (10-12), (20-20), (21-30), (21-32) planes, respectively. Equation 4.1 given below is then used to determine the lattice parameters in a strained state[21]:

$$\left[\frac{4}{3}(h^2+k^2+hk)\right]\frac{1}{a^2}-\left[\frac{4}{3\sqrt{3}}(2h^2+2k^2+5hk)\right]\frac{\delta}{a^2}+(l^2)\frac{1}{c^2}=\frac{1}{d_{hkl}^2} \qquad (4.1)$$

where a and c are the lattice constants; δ is the offset of basis angle γ; h, l, k are the Miller indices.

Once the lattice parameters are obtained, the strain can then be calculated using a group of equations below:

$$\varepsilon_{xx} = \varepsilon_{11-20} = \frac{a_s - a_0}{a_0} \tag{4.2}$$

$$\varepsilon_{zz} = \varepsilon_{0001} = \frac{c_s - c_0}{c_0} \tag{4.3}$$

$$\varepsilon_{yy} = \varepsilon_{1-100} = \frac{m_s - m_0}{m_0} \tag{4.4}$$

where ε_{xx} is the out-of-plane strain along the [11-20] direction (i.e., the growth direction), ε_{zz} and ε_{yy} are the in-plane strain along the [0001] direction (i.e., the *c* direction) and the [1-100] (i.e., the *m* direction which is perpendicular to the *c* direction), respectively. a_s is the lattice constant in a strained state along the vertical direction, while c_s and m_s are the in-plane lattice constants along the *c* direction and the *m* direction in a strained state, respectively. a_0, c_0 and m_0 represent the corresponding lattice constants in a fully relaxed state.

Lattice Parameters (Å)			**Elastic Stiffness Constants (GPa)**			
a_0	c_0	m_0	C_{11}	C_{12}	C_{13}	C_{33}
3.1893	5.1851	2.7620	390	145	106	398

Table 4.1. Lattice constants and elastic stiffness coefficients of GaN in an unstrained state.

The stress along the growth direction σ_{xx} is naturally zero. The stress along the *c* direction and the *m* direction, labelled as σ_{zz}, and σ_{yy}, respectively, can be expressed by:

$$\sigma_{zz} = C_{13}\varepsilon_{xx} + C_{13}\varepsilon_{yy} + C_{33}\varepsilon_{zz} \tag{4.5}$$

$$\sigma_{yy} = C_{12}\varepsilon_{xx} + C_{11}\varepsilon_{yy} + C_{13}\varepsilon_{zz} \tag{4.6}$$

where C_{ij} are the elastic stiffness coefficients. All the parameters used for the present study are listed in Table 4.1[25,26].

Table 4.2 shows all the strain related data which are obtained based on the discussion above and our detailed XRD measurements. The "+" and "-" signs in Table 4.2 indicate tensile and compressive strain, respectively.

Sample	a_s (Å)	c_s (Å)	m_s (Å)	γ (deg)	ε_{11-20} (%)	ε_{0001} (%)	ε_{1-100} (%)	σ_{zz} (GPa)	σ_{yy} (GPa)
A	3.1926	5.1769	2.7579	119.87	+0.102	−0.158	−0.150	−0.6810	−0.6051
B	3.1926	5.1769	2.7578	119.87	+0.103	−0.158	−0.152	−0.6813	−0.6123
C	3.1928	5.1764	2.7575	119.86	+0.109	−0.169	−0.164	−0.7297	−0.6602
D	3.1944	5.1810	2.7571	119.83	+0.160	−0.080	−0.178	−0.3371	−0.5472
ASG	3.1935	5.1799	2.7540	119.79	+0.132	−0.101	−0.291	−0.5704	−1.0487

Table 4.2. Lattice constants, interplanar spacing, distorted angle, strain and stress of all the (11–20) GaN samples. ASG represents as-grown sample.

The lattice constants *a* and *c* obtained are in good agreement with the RSM measurements discussed above. Table 4.2 also demonstrates that all the samples generally exhibit compressive in-plane strain along both the [0001] and [1-100] direction, while the strain along the out-of-plane direction is tensile. This agrees with the previous report based on a fact that the unit cell of *r-plane* sapphire is smaller than that of *a-plane* GaN (i.e., non-polar GaN) grown on sapphire[27].

For the as-grown template, the strain along the [1-100] direction is nearly three times higher than that along the [0001] direction, showing strong anisotropy. This anisotropic strain caused is due to the remarkable contrast of the lattice mismatch between *r-plane* sapphire and *a-plane* GaN along the [1-100] and [0001] directions, which are 16% and 1%, respectively. For the overgrown GaN on the stripe-patterned template, Table 4.2 shows that the strain along the [1-100] is almost twice as that along the [0001] direction, indicating that the in-plane strain is still highly anisotropic. This can be simply understood from the overgrowth process: the overgrowth initiates from the sidewalls of stripes, then advances along the [0001] direction only and finally leads to coalescence with the formation of voids underneath but not along the [1-100] direction due to the stripe configuration. Consequently, the overgrowth along the [0001] direction is free to proceed till coalescence, while the growth along the [1-100] direction is confined as a result of the stripes which orientate along the [1-100] direction throughout the whole overgrowth process. Therefore, strain relaxation can easily occur along the [0001] direction, but it does not effectively take place along the [1-100] direction.

Table 4.2 shows that all the overgrown GaN samples (i.e., Sample A, B and C) on our regularly arrayed micro-rod templates exhibit isotropic in-plane strain. This is due to our micro-rod pattern, as the overgrown GaN can laterally proceed along all the in-plane directions, although the growth rates are different. Finally, the coalescence is completed with forming voids along all the directions. Therefore, such a growth mode leads to strain relaxation along all the directions, thus forming an isotropic in-plane distribution.

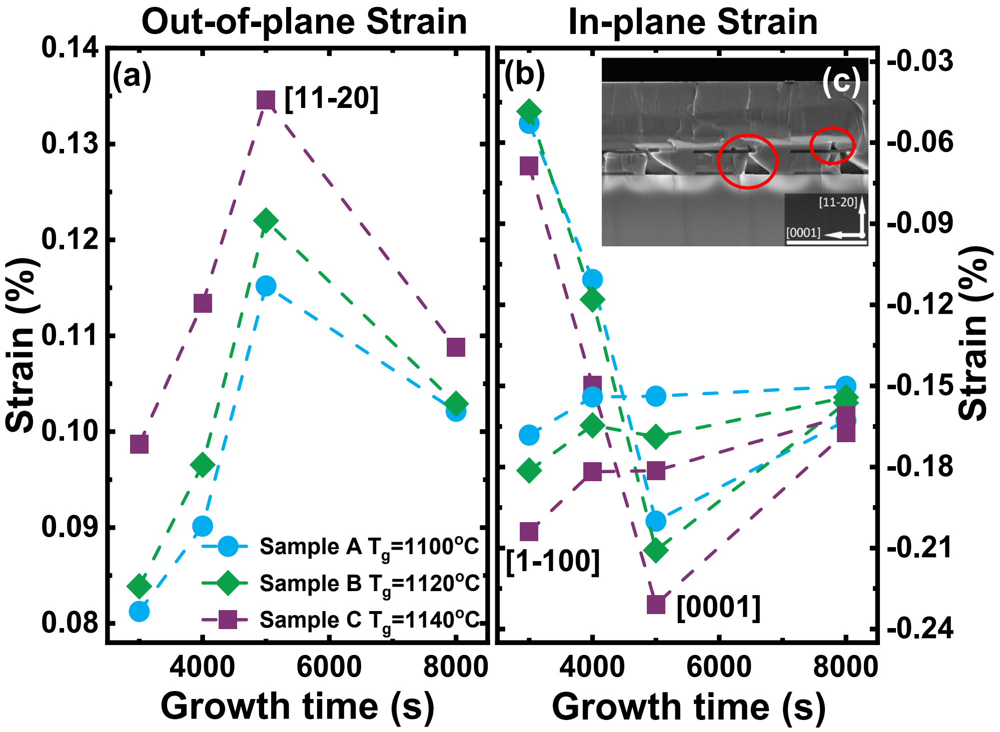

Figure 4.6. (a) Out-of-plane strain evolution of Sample A, B and C as a function of overgrowth time; (b) in-plane strain evolution of Sample A, B and C as a function of overgrowth time. Inset: Cross-sectional SEM image of a fully coalesced sample overgrown on our regularly arrayed micro-rod template. The red circles highlight two kinds of voids. Scale bar: 2 μm.

Figure 4.6 shows the strain of our overgrown GaN samples on the regularly arrayed micro-rod templates grown at different temperatures as a function of overgrowth time, demonstrating how the strain evolves corresponding to the overgrowth evolution as shown in Fig. 4.3. Figure 4.6 shows that the strain along all the directions generally increases with increasing growth temperature. This is consistent with the fact that thermal strain increases with increasing growth temperature.

Figure 4.6 also indicates that the strain increases with increasing overgrowth time of up to 5000 seconds, where the growth process evolves from initial growth from the sidewalls to almost full coalescence, confirmed from Fig. 4.3. Further increasing overgrowth time leads to the completion of the formation of two kinds of voids (Inset shows a cross-sectional SEM image, demonstrating one kind of voids formed between micro-rods and another kind of voids formed on top of each SiO_2 mask). Consequently, the strain gradually reduces after 5000 seconds.

4.4 Summary

In conclusion, by means of overgrowth on regularly arrayed micro-rod templates (11-20) non-polar GaN with significantly improved crystal quality has been obtained, leading to the record low FWHM of XRD rocking curves achieved on *r-plane* sapphire. A systematic study of strain relaxation and in-plane strain distribution has been carried out by performing detailed X-ray measurements along symmetric and skew-symmetric directions. These results have been compared with the standard non-polar GaN grown on *r-plane* sapphire without involving any patterning processes and the overgrown sample on the widely used stripe-pattern template. This comparison demonstrates that the as-grown sample exhibits a highly anisotropic in-plane distribution, while the overgrown GaN on our regularly arrayed micro-rod template shows an isotropic in-plane distribution. Between them is the overgrown sample on the standard stripe-patterned template.

Reference

1. Asif Khan, M., Kuznia, J. N., Bhattarai, A. R. & Olson, D. T. Metal semiconductor field effect transistor based on single crystal GaN. Appl. Phys. Lett. 62, 1786–1787 (1993).

2. Wu, Y. F. et al. Very high breakdown voltage and large transconductance realized on GaN heterojunction field effect transistors. Appl. Phys. Lett. 69, 1438–1440 (1996).

3. Yoshida, S., Ishii, H., Li, J., Wang, D. & Ichikawa, M. A high-power AlGaN/GaN heterojunction field-effect transistor. Solid. State. Electron. 47, 589–592 (2003).

4. Uemoto, Y. et al. 8300V blocking voltage AlGaN/GaN power HFET with thick poly-AIN passivation. Tech. Dig. - Int. Electron Devices Meet. 861–864 (2007).

5. Bernardini, F., Fiorentini, V. & Vanderbilt, D. Spontaneous polarization and piezoelectric constants of III-V nitrides. Phys. Rev. B 56, R10024–R10027 (1997).

6. Paskova, T. Development and prospects of nitride materials and devices with non-polar surfaces. Phys. Status Solidi B 245, 1011–1025 (2008).

7. Oku, T., Kamo, Y. & Totsuka, M. AlGaN/GaN HEMTs passivated by Cat-CVD SiN Film. Thin Solid Films 516, 545–547 (2008).

8. Chang, C. Y. et al. Effect of gate orientation on dc characteristics of Si-doped, non-polar AlGaN/GaN metal-oxide semiconductor high electron mobility transistors. Appl. Phys. Lett. 95, 082110 (2009).

9. Ishida, M., Kuroda, M., Ueda, T. & Tanaka, T. Non-polar AlGaN/GaN HFETs with a normally off operation. Semicond. Sci. Technol. 27, 024019 (2012).

10. Zakharov, D. N. et al. Structural TEM study of non-polar *a-plane* gallium nitride grown on $(11\bar{2}0)$4H-SiC by organometallic vapor phase epitaxy. Phys. Rev. B 71, 235334 (2005).

11. Smalc-Koziorowska, J., Tsiakatouras, G., Lotsari, A., Georgakilas, A. & Dimitrakopulos, G. P. The defect character of GaN growth on *r-plane* sapphire. J. Appl. Phys. 107, 073525 (2010).

12. Bai, J. et al. (11-22) semipolar InGaN emitters from green to amber on overgrown GaN on micro-rod templates. Appl. Phys. Lett. 107, 261103 (2015).

13. Wang, T. Topical Review: Development of overgrown semi-polar GaN for high efficiency green/yellow emission. Semicond. Sci. Technol. 31, 093003 (2016).

14. Zhang, Y. et al. Defect reduction in overgrown semi-polar (11-22) GaN on a regularly arrayed micro-rod array template. AIP Adv. 6, 025201 (2016).

15. Zhang, Y. et al. Microstructure investigation of semi-polar (11-22) GaN overgrown on differently designed micro-rod array templates. Appl. Phys. Lett. 109, 241906 (2016).

16. Roder, C. et al. Stress and wafer bending of *a-plane* GaN layers on *r-plane* sapphire substrates. J. Appl. Phys. 100, 103511 (2006).

17. Tsuda, M. et al. Anisotropically biaxial strain in *a-plane* AlGaN on GaN grown on *r-plane* sapphire. Jpn. J. Appl. Physics 45, 2509–2513 (2006).

18. Darakchieva, V. et al. Anisotropic strain and phonon deformation potentials in GaN. Phys. Rev. B 75, 195217 (2007).

19. Zhao, G. et al. Anisotropically biaxial strain in non-polar (11-20) plane InxGa1−xN/GaN layers investigated by X-ray reciprocal space mapping. Sci. Rep. 7, 4497 (2017).

20. Darakchieva, V. et al. Lattice parameters of GaN layers grown on *a-plane* sapphire: Effect of in-plane strain anisotropy. Appl. Phys. Lett. 82, 703–705 (2003).

21. Laskar, M. R. et al. Distorted wurtzite unit cells: Determination of lattice parameters of non-polar *a-plane* AlGaN and estimation of solid phase Al content. J. Appl. Phys. 109, 013107 (2011).

22. Ranalli, F. et al. Non-polar AlN and GaN/AlN on *r-plane* sapphire. Phys. Status Solidi C 6, S780 (2009).

23. Imer, B. M., Wu, F., Denbaars, S. P. & Speck, J. S. Improved quality (11-20) *a-plane* GaN with sidewall lateral epitaxial overgrowth. Appl. Phys. Lett. 88, 061908 (2006).

24. Jiang, T., Xu, S. R., Zhang, J. C., Xie, Y. & Hao, Y. Spatially resolved and orientation dependent Raman mapping of epitaxial lateral overgrowth non-polar *a-plane* GaN on *r-plane* sapphire. Sci. Rep. 6, 19955 (2016).

25. Vurgaftman, I. & Meyer, J. R. Band parameters for nitrogen-containing semiconductors. J. Appl. Phys. 94, 3675–3696 (2003).

26. Morkoç, H. Handbook of Nitride Semiconductors and Devices: Materials Properties, Physics and Growth 1, 15 (Wiley-VHC, 2009).

27. Morkoç, H. Nitride Semiconductors and Devices 97 (Springer, 1999)

Chapter 5

Monolithic Multiple Colour Emission from InGaN Grown on Patterned Non-polar GaN

A novel overgrowth approach has been developed in order to create a multiple-facet structure consisting of only semi-polar and non-polar GaN facets without involving any c-plane facets, allowing the major drawbacks of utilising c-plane GaN for the growth of III-nitride optoelectronics to be eliminated. Such a multiple-facet structure can be achieved by means of overgrowth on non-polar GaN micro-rod arrays on r-plane sapphire. InGaN multiple quantum wells (MQWs) are then grown on the multiple-facet templates. Due to the different efficiencies of indium incorporation on semi-polar and non-polar GaN facets, multiple-colour InGaN/GaN MQWs have been obtained. Photoluminescence (PL) measurements have demonstrated that the multiple-colour emissions with a tunable intensity ratio of different wavelength emissions can be achieved simply through controlling the overgrowth conditions. Detailed cathodoluminescence measurements and excitation-power dependent PL measurements have been performed, further validating the approach of employing the multiple facet templates for the growth of multiple colour InGaN/GaN MQWs. It is worth highlighting that the approach potentially paves the way for the growth of monolithic phosphor-free white emitters in the future.

5.1 Introduction

The last two decades have seen tremendous progress in developing III-nitride semiconductor visible light emitters for solid-state lighting. III-nitrides all exhibit direct bandgaps, covering the whole visible spectral region from deep ultraviolet to infrared (from 6.2 eV for AlN through 3.5 eV for GaN to 0.7 eV for InN).

Therefore, in principle, III-nitrides can be fabricated into white light emitters without involving any other material systems. However, the state-of-the-art achieved so far is still based on the well-known "blue light emitting diodes (LEDs) + yellow phosphor" approach, where the blue emission from InGaN/GaN-based LEDs grown on c-plane substrates radiatively pumps yttrium aluminium garnet (YAG) phosphors to provide yellow emission leading to the generation of white light[1–4]. It is worth highlighting that this approach suffers a number of drawbacks, such as the self-absorption of phosphors leading to additional limits on the overall efficiency, the issue on quenching and stability of phosphors as a result of heat generated, etc[5–7]. Furthermore, another fundamental issue of this approach is due to the very slow response time of phosphors, typically on the order of microseconds, significantly limiting a modulation bandwidth down to the 1 MHz level for visible light communication (Li-Fi) applications[8].

It is expected that an ultimate lighting source for general illumination would be a phosphor-free white LED, which requires both the highest efficiency and the best colour rendering index. It is also required that both colour quality and optical efficiency remain unchanged with increasing injection current. Phosphor-free white LEDs developed so far are primarily grown on c-plane substrates, i.e., by introducing InGaN multiple quantum wells (MQWs) with different indium composition as an active region[9–12]. However, due to the well-known polarisation induced quantum confined Stark effect (QCSE), it is difficult to achieve a phosphor-free white LED with high optical efficiency on a c-plane substrate[13]. Another great challenge in developing a monolithic white LED is due to the fundamental limitation in incorporating high indium content into GaN on c-plane substrates, while InGaN with high indium content is crucial for achieving green or yellow emission, the major components for phosphor-free white LEDs. The QCSE issue also leads to an increase in carrier recombination lifetime, thus significantly reducing the modulation bandwidth if such a white LED is used for Li-Fi. This becomes even worse for longer wavelength such as green or yellow emission.

In summary, it is extremely difficult to achieve phosphor-free white LEDs with desired performance on c-plane substrates. Monolithic multi-colour emissions have been reported by means of employing three dimensional (3D) GaN structures including GaN hexagonal annular structures[14–16]. However, these structures still involve the utilization of c-plane GaN[9,10,14–18]. Therefore, the fundamental issues still exist.

In order to resolve these challenges, we need to design a new structure with multiple facets consisting of semi-polar and non-polar facets only, but without involving any c-plane facets. Such requirements cannot be met by using current III-nitride emitters.

It is well-known that a significant reduction in QCSE can be achieved by means of the growth of InGaN LEDs on semi-polar or non-polar GaN, leading to significantly enhanced internal quantum efficiency[19,20]. As a consequence, this also greatly reduces a carrier recombination lifetime, thus effectively increasing a modulation bandwidth for Li-Fi. Second, indium incorporation efficiency can be significantly enhanced if InGaN is grown on semi-polar GaN such as (11–22) GaN in comparison with its c-plane counterparts, which is crucial for the growth of longer wavelength such as yellow/amber/red LEDs[20–22]. Thirdly, non-polar GaN generally leads to reduced indium incorporation efficiency (if InGaN is grown on its top) in comparison with its c-plane counterpart. Therefore, under identical growth conditions, InGaN MQWs grown on semi-polar and non-polar facets will exhibit different wavelength emissions in a single chip if the wafer consists of semi-polar and non-polar facets, potentially obtaining white lighting without any concerns about the drawbacks resulting from the growth on c-plane facets. In order to address this issue, we are proposing a multiple-facet structure which consists of only non-polar GaN facet and semi-polar GaN facets in a single chip, where the InGaN MQWs grown on the non-polar GaN surface is used as a short wavelength emitting region and the InGaN MQWs on the semi-polar GaN surface as a long wavelength emitting region. This potentially leads to monolithic multiple-colour lighting but without involving any growth on a c-plane surface.

Two major challenges need to be overcome in order to achieve the above idea. One is due to the crystalline quality of current semi-polar or non-polar GaN on sapphire or silicon which is far from satisfactory. Another is how to achieve a multiple facet structure without forming c-plane GaN facets.

In this work, we present a novel overgrowth approach to create a multiple-facet structure consisting of only semi-polar and non-polar GaN facets without involving any c-plane facets by means of overgrowth on non-polar GaN micro-rod arrays on r-plane sapphire. Such overgrowth on the micro-rod arrayed templates on sapphire substrates provides an effective approach to achieving significantly improved crystal quality. For details, please refer to ref.[23]. The dislocation density of our non-polar GaN overgrown on micro-rod arrayed templates has been substantially reduced down to $6 \times 10^8/cm^2$ from a typical dislocation density of $10^{11}/cm^2$ for non-polar GaN directly grown on sapphire without involving overgrowth. As a validation purpose, InGaN MQWs are then grown on the multiple-facet structure. Both photoluminescence (PL) and cathodoluminescence (CL) measurements have demonstrated multiple-colour emissions with a tuneable intensity ratio of different wavelength emissions which can be achieved simply through controlling overgrowth time.

5.2 Template Fabrication and Overgrowth

Standard non-polar (11–20) GaN is initially grown on r-plane sapphire by means of a standard metalorganic vapour phase epitaxial (MOVPE) technique using our high temperature AlN buffer approach[24]. A SiO_2 film with a thickness of 150 nm is then deposited on the as-grown non-polar GaN using a standard plasma enhanced chemical vapour deposition (PECVD) technique. Subsequently, by means of a standard photolithography approach and then a reactive ion etching (RIE) technique, the SiO_2 film is fabricated into regularly arrayed micro-rods with a micro-rod diameter of 2.5 μm. The regularly arrayed SiO_2 micro-rod arrays are then used as a second mask to finally etch the GaN layer underneath into regular GaN micro-rod arrays by using a standard inductively coupled etching (ICP) system. The GaN etching is performed down to the sapphire substrate. Each SiO_2 micro mask formed remains on top of each GaN micro-rod. Further details of the fabrication procedure can be found elsewhere[23]. Figure 5.1a shows a plan-view scanning electron microscopy (SEM) image of our regularly arrayed micro-rod template in a chessboard configuration, demonstrating that the diameter of micro-rods is 2.5 μm.

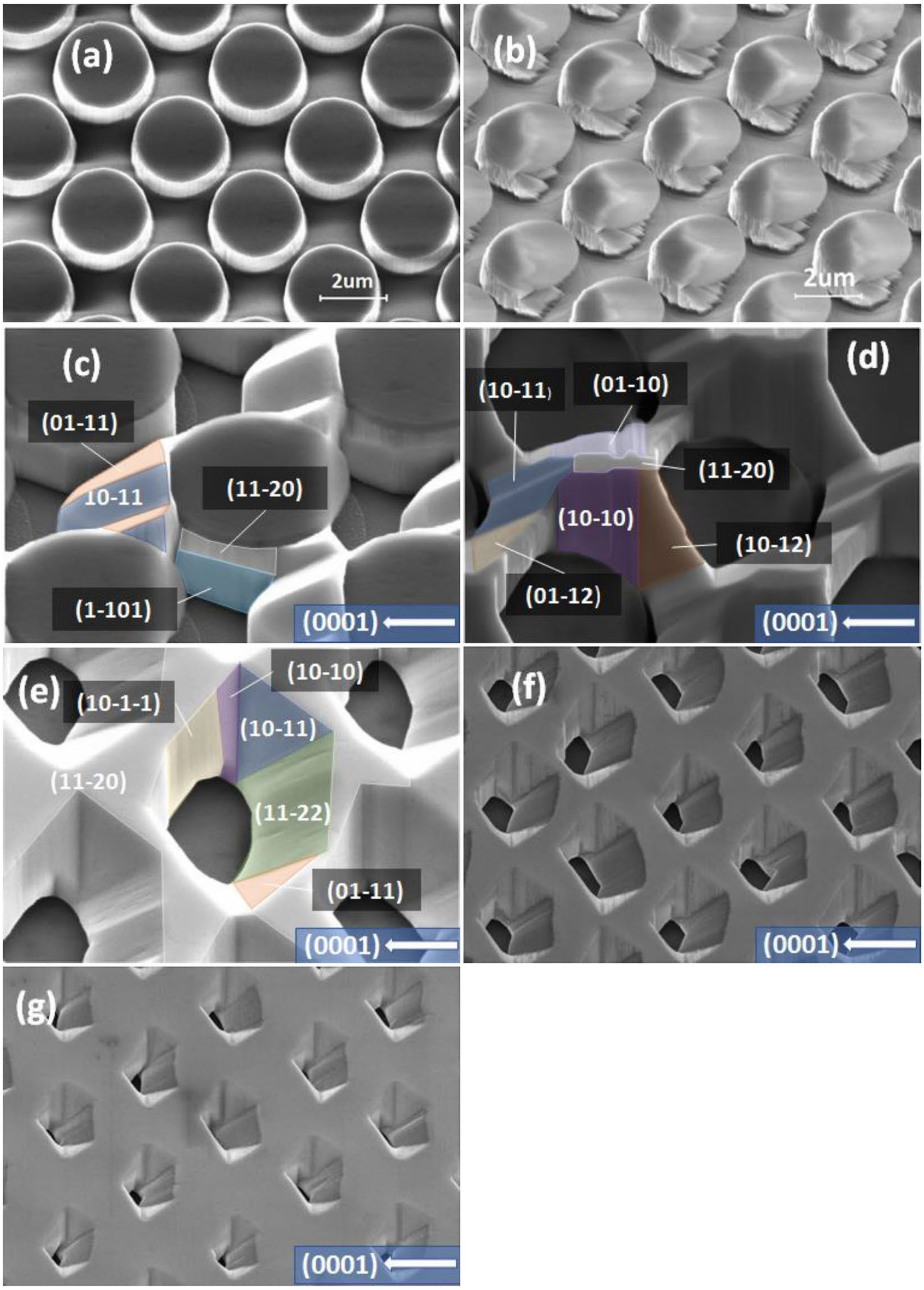

Figure 5.1. (a) Plan-view SEM image of our non-polar GaN micro-rod arrays; (b) Plan-view SEM image of our non-polar GaN micro-rod arrays with a "mushroom" configuration; (c–g) Plan-view SEM images of overgrown GaN on the non-polar GaN micro-rod arrays with a "mushroom" configuration as a function of overgrowth time of 1000, 2000, 3000, 3500 and 4000 seconds, respectively, where multiple semi-polar and non-polar facets have been marked.

The micro-rod template further undergoes an ultraviolet light assisted photochemical etching process in a 10% KOH solution under illumination of a Xenon lamp with a power density of 1.5 W/cm^2, forming a "mushroom" configuration as shown in Fig. 5.1b. Specifically, the side of each micro-rod that faces in the <000–1> direction is etched, while this process does not etch the SiO_2 masks at all. This process does not etch GaN surfaces facing in the <0001> direction, either, but does effectively etch GaN facing in the <000–1> direction. With such a "mushroom" configuration, lateral growth along the <000–1> direction (i.e., -c orientation) can be effectively suppressed. This not only effectively reduces defects but also helps to form semi-polar facets. Such a regularly arrayed micro-rod template was originally designed for overgrowth of (11–20) non-polar GaN with a step-change in crystal quality[23]. Finally, the non-polar GaN micro-rod array template is reloaded into the MOVPE chamber for further overgrowth.

Figure 5.1c–g show the SEM images of an evolution of overgrown non-polar (11–20) GaN on the above micro-rod arrays as a function of overgrowth time of 1000, 2000, 3000, 3500 and 4000 sec, respectively, demonstrating the formation of a multiple facet structure consisting of semi-polar and non-polar GaN facets. It can be observed that lateral growth from the <0001> direction can be observed during the first coalescence process (0–2000 seconds), while lateral growth along the <000–1> orientation is suppressed as a result of the "mushroom" configuration. In the meantime, multiple semi-polar facets naturally form during the first coalescence process. During the second coalescence process (2000–4000 seconds), where the lateral growth of GaN extends above the SiO_2 masks, multiple GaN facets including non-polar (11–20), semi-polar (11–22), (01–11), (10–11) and (1–101) facets labelled in Fig. 5.1e have been formed. Please note that there are no c-plane facets formed on such a micro-rod arrayed non-polar GaN template.

With increasing overgrowth time, the area of non-polar (11–20) facet which is the top surface starts to increase. When the overgrowth time reaches 4000 sec, the template is still un-coalesced but the non-polar (11–20) facet dominates the structure. The formed arrayed micro holes as a result of the un-coalescence lead to the formation of semi-polar facets, among which the (11–22) facet exhibits the largest area. Clearly, by controlling overgrowth time, the facet area ratio of semi-polar to non-polar GaN can be tuned, which in return determines the ratio of emission intensity of long wavelength emission to short wavelength emission once InGaN MQWs are grown on top.

In order to confirm the above idea, an InGaN/GaN MQW structure with 3 periods has been grown under identical conditions on the three templates obtained using different overgrowth time, namely 3000, 3500 and 4000 sec, which are labelled as sample A, sample B and sample C, respectively. All the samples end with a 100 nm GaN cap layer. Figure 5.1c–g clearly show that the facet area ratio of semi-polar to non-polar GaN is determined by controlling overgrowth time. The facet area ratio is reduced by increasing overgrowth time.

5.3 Result and Discussion

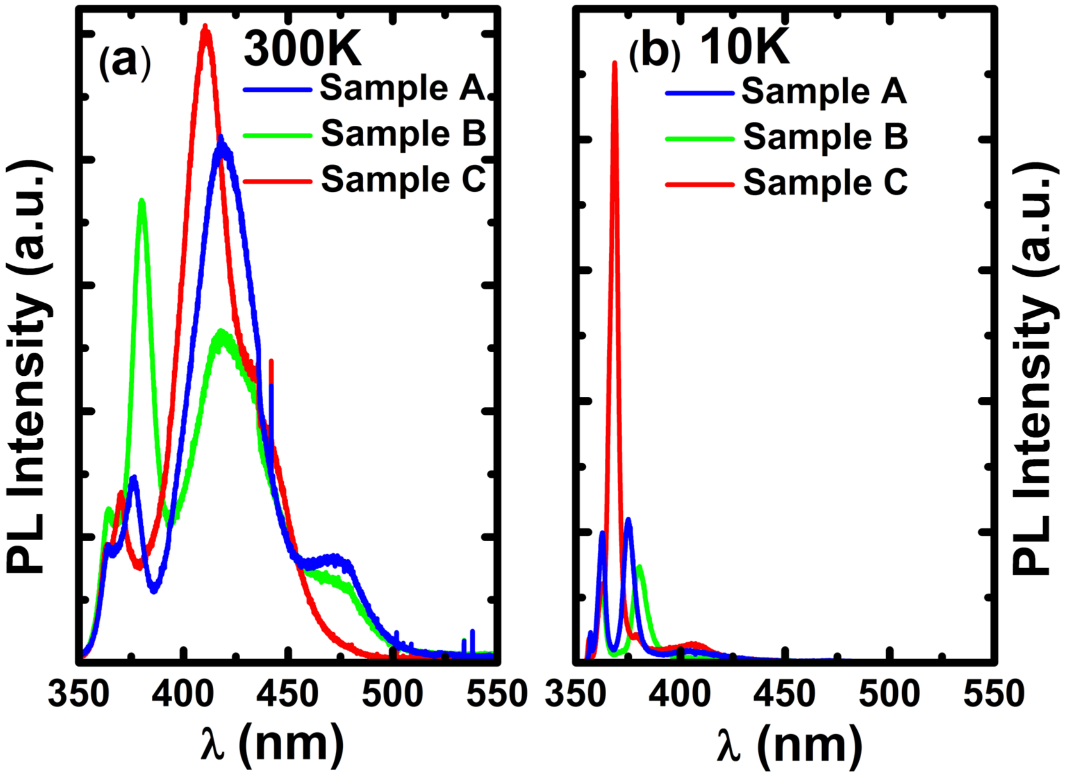

Figure 5.2. (a) PL spectra of sample A, B and C, measured at room temperature, and (b) 10 K using a 325 nm He-Cd laser.

Photoluminescence measurements have been carried out by using either a commercial 325 nm He-Cd laser or a 375 nm diode laser as the excitation source. The emission is dispersed by a monochromator (Horiba SPEX 500 M) and then detected by an air-cooled charge-coupled device (CCD). The samples are placed in a closed-cycle helium cryostat, where the temperature range can be controlled from 10 to 300 K.

Figure 5.2a shows the PL spectra of the three samples, measured by using a 325 nm He-Cd laser under an excitation power density of 100 W/cm^2 at room temperature (RT). In each case, there are three peaks present, one at 362 nm which is from the GaN layer, one around 380 nm, and another one around 410–420 nm. Figure 5.2b displays the PL spectra of these samples measured at 10 K also using the 325 nm He-Cd laser.

By examining the RT PL spectra as shown in Fig. 5.2a very carefully, for sample A and sample B, there exists an additional peak at ~ 475 nm. By detailed comparison, the peak at 475 nm in sample A shows higher intensity than that in sample B. These emissions below the GaN bandgap are from the InGaN MQWs grown on either the (11–20) non-polar facet or the semi-polar facets within the micro-holes formed as a result of overgrowth as shown in Fig. 5.1.

In order to identify the correspondence between these emission peaks and the multiple-facets, detailed CL measurements have been performed on the three samples using CL hyperspectral imaging[25]. The CL hyperspectral imaging was carried out at room temperature using a variable pressure field emission scanning electron microscope (FEI Quanta 250). The emitted light was collected by a Cassegrain reflecting objective, focussed on the entrance slit of a 1/8 m focal length spectrometer (Oriel MS125) and detected using an electron multiplying charge-coupled device (Andor Newton). The CL was collected in hyperspectral imaging mode, meaning a full CL spectrum was collected per pixel in an image[26]. The sample is placed at an angle of 45° with respect to the incident electron beam. The projection of the <0001> direction, i.e., +c direction, is pointing downward in the CL images.

As a typical example, Fig. 5.3a–d show the integrated CL intensity images of sample B calculated from the hyperspectral data set obtained at 5 kV for four spectral ranges of 383–388 nm, 405–415 nm, 432–455 nm and 465–500 nm, respectively, focusing on the InGaN MQWs grown on the different facets. Owing to the higher spatial resolution compared with the area averaged PL measurements in Fig. 5.2, the CL measurement allows us to identify four different emission peaks associated with the MQWs grown on the four different facets.

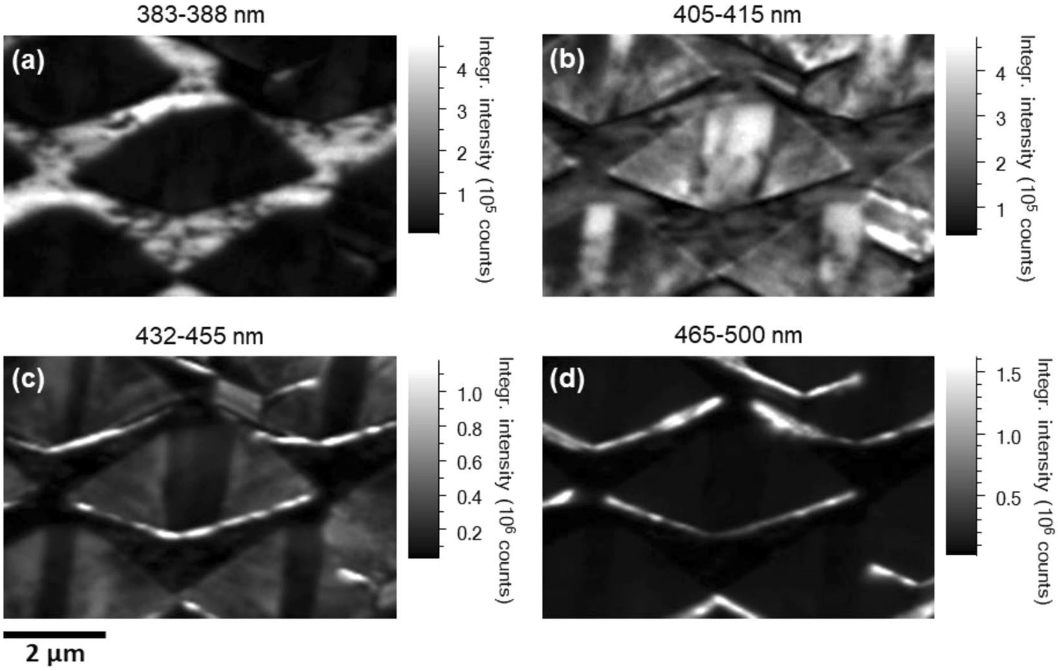

Figure 5.3. Room temperature integrated CL intensity images obtained at 5 kV of sample B calculated for the following spectral ranges: (a) 383–388 nm, (b) 405–415 nm, (c) 432–455 nm and (d) 465–500 nm. The images do not account for the 45° tilt of the sample, and thus the y-axis in each case will need to be corrected by a factor of 1.41.

The 383–388 nm emission is from the top flat surface, which is from the InGaN MQWs grown on the (11–20) non-polar facet as expected. The 405–415 nm emission is due to the InGaN MQWs grown on the semi-polar (11–22) facet (i.e., the semi-polar facet with the largest area within the micro-hole formed as shown in Fig. 5.1e). The emission at 432–455 nm is primarily from the (10–11) and (01–11) semi-polar facets, while the 465–500 nm emission peak is from the (10–1–1) and (01-1-1) semi-polar facets. It is well-known that InGaN grown on different semi-polar facets exhibit different indium incorporation efficiency, leading to emission with different wavelengths. The results further confirm that indium incorporation efficiency of InGaN on semi-polar GaN facets exhibits: (10-1-1) > (10–11) > (11–22), which is in good agreement with the previous studies[20]. All the semi-polar facets exhibit higher indium incorporation efficiency than the non-polar (11–20) facet, also matching the previous studies very well[17,18,28].

Comparing the RT PL of the three samples, the emission intensity ratio of short wavelength emission (non-polar) to long wavelength emissions (semi-polar) is different, as the non-polar facet area increases, and the multiple semi-polar facet area decreases with increasing overgrowth time. It is worth highlighting that both the (11–20) nonpolar facet and the semi-polar facets with well-controlled areas can be achieved, potentially allowing us to tune the ratio of the emission intensities of InGaN MQWs grown on these facets.

It is well-known that the radiative recombination lifetime of InGaN MQWs is very short at a low temperature, typically hundreds of picoseconds, where the radiative recombination processes at a low temperature dominate the emission. Therefore, if a 325 nm He-Cd laser is used as an excitation source, the emission from GaN and the emission from non-polar InGaN MQWs at 380 nm can be observed, while it would be difficult to observe the emission from any semi-polar GaN MQWs (where the InGaN content is higher than that in the non-polar InGaN MQWs). The physics behind is due to the fact that the radiative recombination lifetime of non-polar InGaN MQWs is so short that there is not enough time for excitons to diffuse to the semi-polar InGaN MQWs. This is what has been observed in Fig. 5.2b.

However, if a 375 nm laser is used as an excitation source, the emissions from the semi-polar InGaN MQWs can be observed as the non-polar InGaN MQWs at 380 nm are not optically excited considering that there may be a Stokes-shift[20]. Of course, at room temperature, it is well-known that non-radiative recombination processes dominate the emission of InGaN/GaN MQWs. As a result, the emission from semi-polar InGaN/GaN MQWs can be observed regardless of whether a 325 nm laser or 375 nm laser is used as an excitation source.

Figure 5.4a shows the excitation power dependent PL spectra of sample B measured at 10 K using a 325 nm He-Cd laser, indicating that there are only three peaks present with increasing excitation power density from 81 W/cm^2 to 69 kW/cm^2. The peaks at 357 nm and 362 nm are due to the near-band-edge emission (NBE) of GaN and the GaN basal-plane stacking fault related emission, respectively, which have been well-studied[28]. The peak at 380 nm is due to the non-polar InGaN MQWs, and there is no blue shift observed with increasing excitation power density, a typical fingerprint for non-polar InGaN MQWs, which do not exhibit the QCSE. These results agree well with our expectation stated above.

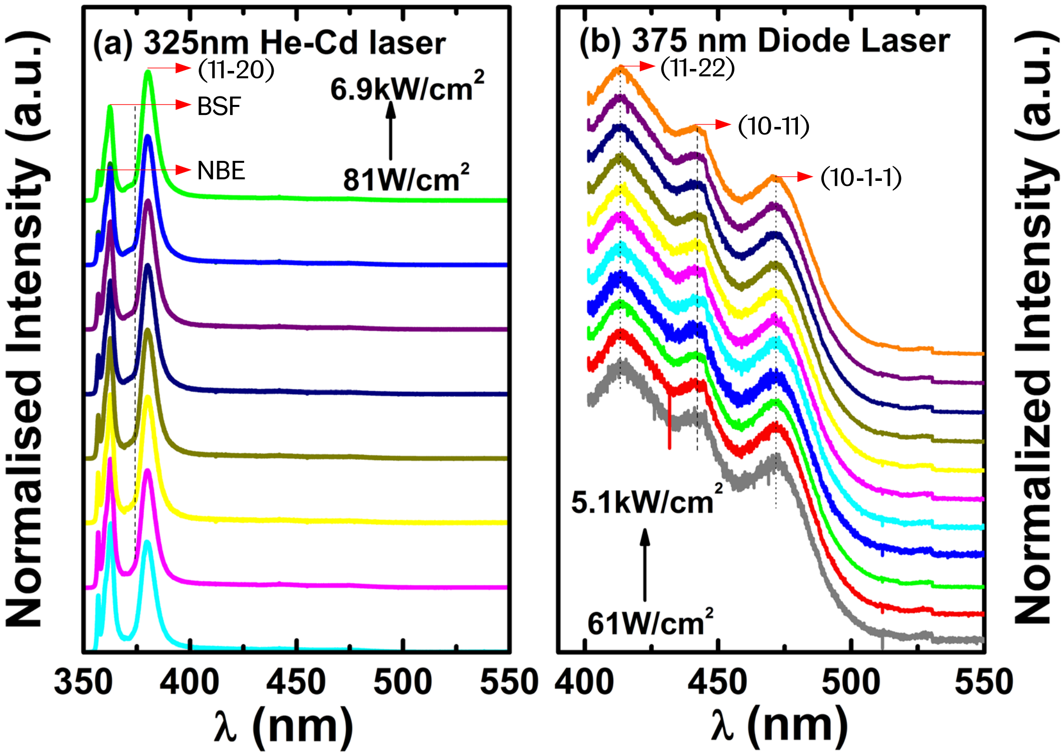

Figure 5.4. Excitation power density dependent PL spectra of sample B measured at 10 K using a 325 nm He-Cd laser (a); and a 375 nm diode laser (b).

In order to investigate the optical properties of the InGaN/GaN MQWs from semi-polar facets, a 375 nm laser diode is used as an excitation source, where the non-polar MQWs cannot be excited. Figure 5.4b shows the PL spectra as a function of excitation power density from 61 W/cm^2 to 5.1 kW/cm^2 measured at 10 K. The emission peaks around 413 nm, 442 nm, and 472 nm are from the MQWs on the different semi-polar facets as discussed above. In contrast to the non-polar (11–20) emission peak, these emission peaks at 413 nm, 442 nm and 472 nm exhibit a weak blueshift of up to 1 nm in emission wavelength with increasing excitation power density, a typical behaviour for semi-polar InGaN MQWs. Of course, the blueshift is much weaker than that for their c-plane counterparts, agreeing with significantly reduced QCSE in comparison with their c-plane counterparts.

5.4 Summary

In conclusion, we have reported a novel approach to grow a multiple-facet structure consisting of only semi-polar and non-polar GaN facets without involving any c-plane facets by means of overgrowth on a non-polar GaN micro-rod array template on r-plane sapphire. Multiple-colour InGaN/GaN MQWs grown on such a multiple facet template have been achieved. Both PL and CL measurements have confirmed that the longer wavelength emission is from the InGaN/GaN MQWs grown on semi-polar facets, while the shorter wavelength emission is from the MQWs grown on the (11–20) non-polar facet. This is due to higher indium incorporation efficiency of InGaN grown on a semi-polar facet in comparison with that grown on a non-polar facet. The emission intensity ratio of the longer wavelength emission to the shorter wavelength emission can be tuned by simply controlling the thickness of the multiple-facet templates. The presented approach has demonstrated a great potential to achieve a white phosphor-free LED with high performance.

Reference

1. Meneghesso, G., Meneghini, M. & Zanoni, E. Recent results on the degradation of white LEDs for lighting. J. Phys. D: Appl. Phys. 43, 354007 (2010).

2. Won, Y. H. et al. Effect of phosphor geometry on the luminous efficiency of high-power white light-emitting diodes with excellent color rendering property. Opt. Lett. 34, 1 (2009).

3. He, G., Zheng, L. & Yan, H. LED white lights with high CRI and high luminous efficacy. Proc. SPIE 7852, 50 (2010).

4. Mueller-Mach, R. et al. High efficient all-nitride phosphor-converted white light emitting diode. Phys. Stat. Solidi A 202, 1727 (2005).

5. Meneghini, M. et al. Stability and performance evaluation of high-brightness light-emitting diodes under DC and pulsed bias conditions. Proc. SPIE 6337, 63370R (2006).

6. Ishizaki, S., Kimura, H. & Sugimoto, M. Lifetime estimation of high power LEDs. J. Light Vis. Environ. 31, 11 (2007).

7. Hu, J., Yang, L. & Shin, M. W. Electrical, optical and thermal degradation of high power GaN/InGaN light-emitting diodes. J. Phys. D: Appl. Phys. 41, 035107 (2008).

8. Chow, W., Yeh, C. H., Liu, Y. F. & Liu, Y. Improved modulation speed of LED visible light communication system integrated to main electricity network. Electron. Lett. 47, 867 (2011).

9. Yamada, M., Narukawa, Y. & Mukai, T. Phosphor free high-luminous-efficiency white light-emitting diodes composed of InGaN multi-quantum well. Jpn. J. Appl. Phys. 41, L246 (2002).

10. Ooi, Y. K. & Zhang, J. Design analysis of phosphor-free monolithic white light-emitting-diodes with InGaN/GaN multiple quantum wells on ternary InGaN substrates. AIP Advances 5, 057168 (2015).

11. Shei, S. C. et al. Emission mechanism of mixed-color InGaN/GaN multi-quantum-well light-emitting diodes. Jpn. J. Appl. Phys. 45, 2463 (2006).

12. Lu., C. F. et al. Phosphor-free monolithic white-light LED. IEEE J. Sel. Top. Quantum Electron. 15, 1210 (2009).

13. Bernardini, F., Fiorentini, V. & Vanderbilt, D. Spontaneous polarization and piezoelectric constants of III-V nitrides. Phys. Rev. B 56, R10024(R) (1997).

14. Min, D. et al. Phosphor-free white-light emitters using in-situ GaN nanostructures grown by metal organic chemical vapor deposition. Sci. Rep. 5, 17372 (2015).

15. Lim, S. H. et al. Electrically driven, phosphor-free, white light-emitting diodes using gallium nitride-based double concentric truncated pyramid structures. Light Sci. Appl. 5, e16030 (2016).

16. Ko, Y. H., Song, J., Leung, B., Han, J. & Cho, Y. H. Multi-color broadband visible light source via GaN hexagonal annular structure. Sci. Rep. 4, 5514 (2014).

17. Wernicke, T. et al. Indium incorporation and emission wavelength of polar, nonpolar and semipolar InGaN quantum wells. Sci. Technol. 27, 024014 (2012).

18. Zhao, Y. et al. Indium incorporation and emission properties of nonpolar and semipolar InGaN quantum wells. Appl. Phys. Lett. 100, 201108 (2012).

19. Paskova, T. Development and prospects of nitride materials and devices with nonpolar surface. Phys. Status Solidi B 245, 1011 (2008).

20. Wang, T. Topical review: development of overgrown semi-polar GaN for high efficiency green/yellow emission. Semicond. Sci. Technol. 31, 093003 (2016).

21. Gong, Y. et al. High efficiency green-yellow emission from InGaN/GaN quantum well structures grown on overgrown semi-polar (11–22) GaN on regularly arrayed micro-rod templates. ECS Trans. 66, 151 (2015).

22. Bai, J. et al. (11–22) semipolar InGaN emitters from green to amber on overgrown GaN on micro-rod templates. Appl. Phys. Lett. 107, 261103 (2015).

23. Jiu, L., Gong, Y. & Wang, T. Overgrowth and strain investigation of (11–20) non-polar GaN on patterned templates on sapphire. Sci. Rep. 8, 9898 (2018).

24. Ranalli, F. et al. Non-polar AlN and GaN/AlN on r-plane sapphire. Phys. Status Solidi C 6, S780 (2009).

25. Bruckbauer, J., Edwards, P. R., Wang, T. & Martin, R. W. High resolution cathodoluminescence hyperspectral imaging of surface features in InGaN/GaN multiple quantum well structures. Appl. Phys. Lett. 98, 141908 (2011).

26. Edwards, P. R. et al. High-Resolution Cathodoluminescence Hyperspectral Imaging of Nitride Nanostructures. Microsc. Microanal. 18, 1212 (2012).

27. Koleske D. et al. Semi-polar GaN Materials Technology for High IQE Green LEDs. Sandia Report (2013).

28. Guhne, T. et al. Band-edge photoluminescence and reflectivity of nonpolar (11–20) and semipolar (11–22) GaN formed by epitaxial lateral overgrowth on sapphire. Phys. Rev. B 77, 075308 (2008).

Chapter 6

Optical and Polarisation Properties of Non-polar InGaN-based Light-emitting diodes Grown on Micro-rod Templates

We have demonstrated InGaN multiple-quantum-well (MQW) light-emitting diodes (LEDs) grown on non-polar a-plane GaN templates on sapphire, where the non-polar GaN templates with substantially improved quality have been achieved by means of overgrowth on regularly arrayed micro-rods with a “mushroom” configuration. Photoluminescence (PL) measurements show one main emission peak at 418 nm along with another weak peak at 448 nm. Wavelength mapping measurements carried out by using a high spatial-resolution confocal PL system indicate that the two emissions origin from different areas associated with the underlying micro-rod patterns. Electroluminescence measurements exhibit a negligible blue-shift of 1.6 nm in the peak wavelength of the main emission with increasing injection current from 10 to 100 mA, indicating an effective suppression in quantum confined Stark effect in the a-plane LED. Polarization measurements demonstrate a polarization ratio of 0.49 for the low-energy emission (~ 448 nm), while the main emission (~ 418 nm) shows a polarization ratio of 0.34. Furthermore, the polarization ratios are independent of injection current, while the energy separation between m-polarized and c-polarized lights increases with the injection current for both emissions.

6.1 Introduction

Last two decades have seen major developments in the field of III-nitride based optoelectronics, represented by InGaN-based blue emitters. However, the major achievements are predominately limited to GaN grown on c-plane substrates, where the fundamental limit in further developing c-plane III-nitride based optoelectronics exists due to polarization induced electric fields. The internal electric fields lead to the well-known quantum confined Stark effect (QCSE), and substantially decrease the oscillator strength of electron-hole pairs, thus reducing quantum efficiency[1-3].

In order to address this great challenge, one of the most promising solutions is to grow GaN along a nonpolar direction. Due to the absence of the polarization-related electric fields along the growth direction, nonpolar GaN is nearly QCSE free, which ensures the enhancement in exciton recombination. More importantly, nonpolar InGaN-based emitters exhibit another major advantage which current c-plane InGaN-based emitters lack, their polarized light source, resulting from the valence band splitting generated by anisotropic biaxial stress[4,5]. This is expected to play an important role in manufacturing backlighting in terms of improving power consumption and compactness[6], as the current approach is to insert a polarizer and thus up to 30% optical power is wasted.

Up to date, nonpolar III-nitride devices with high performance have to be grown on extremely expensive GaN substrates[7,8], where the size of GaN substrates is typically limited to a size of 10 × 10 mm^2. Therefore, it is necessary to develop a new approach to achieve nonpolar GaN on industry-matched substrates, such as sapphire or silicon. The crystal quality of current nonpolar GaN grown on either sapphire or silicon is far from satisfactory. Typically, non-polar GaN grown on sapphire without any extra processes exhibits a dislocation density of above $10^{10}/cm^2$ and a stacking fault density of above $10^6/cm$ [9,10]. Conventional epitaxial lateral overgrowth (ELOG) and related techniques have been employed to improve the crystal quality of nonpolar or semi-polar GaN on sapphire[11,12], which are based on selective area overgrowth on normal stripe-patterned templates. However, it is difficult for such a stripe-patterned template to achieve quick coalescence and an atomically flat surface as a result of intrinsically anisotropic in-plane growth rate[13].

Our group has achieved high quality nonpolar (11-20) GaN films by using an overgrowth approach on regularly arrayed non-polar GaN micro-rods on r-plane sapphire[13], demonstrating X-ray rocking curve line widths of 270 arcsec along the [0001] direction and 380 arcsec along the [1-100] direction, which is the best report for so far. In this work, we demonstrate nonpolar InGaN/GaN multiple quantum well (MQW) light-emitting diodes (LEDs) grown on such high quality nonpolar GaN templates. Optical and polarization properties have been investigated by photoluminescence (PL), Confocal PL, and polarized electroluminescence (EL) measurements.

6.2 Methods

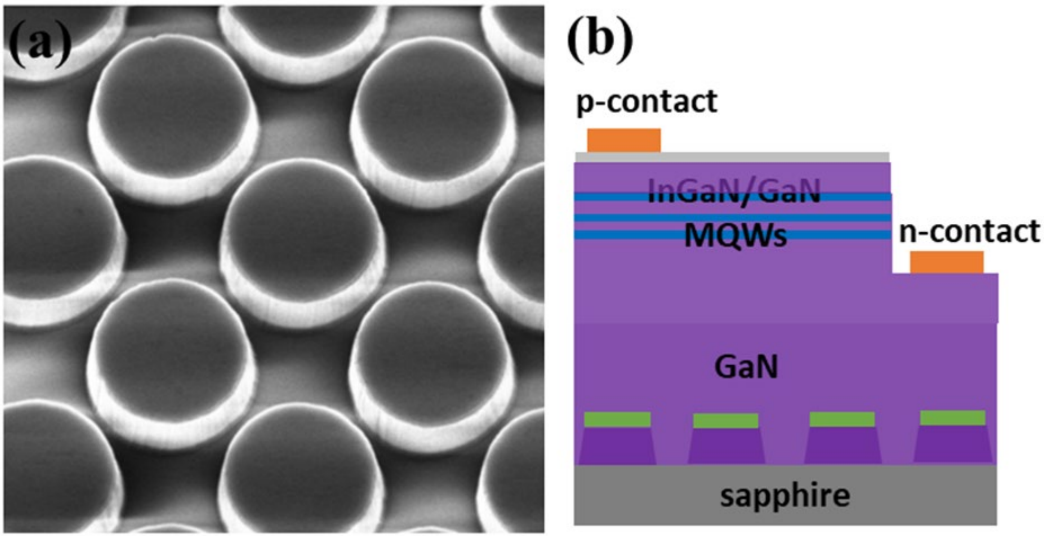

Figure 6.1. (a) SEM image of a micro-rod GaN template; and (b) Schematic of nonpolar InGaN/GaN MQW LED.

A standard nonpolar GaN layer is first grown on r-plane sapphire by a standard metal organic chemical vapour deposition using our high temperature AlN buffer technology[14]. Subsequently, the as-grown nonpolar GaN template is fabricated into regularly arrayed micro-rods by means of a standard photolithography technique and then dry-etching processes (Figure 6.1a). The micro-rod template then undergoes ultra-violet assisted photo-enhanced chemical etching processes[13], forming a mushroom configuration. The overgrowth on such a micro-rod arrayed template allows us to achieve not only substantially improved crystal quality, but also a quick coalescence and resulting atomically flat surface as our designed patterning can compensate for the intrinsically anisotropic in-plane growth rate of nonpolar GaN.

Following the growth of high quality overgrown nonpolar GaN with a layer thickness of 3 μm, a LED structure is grown, which consists of a 1 μm Si-doped n-type GaN layer, three pairs of InGaN/GaN MQWs, and finally a 150 nm Mg-doped p-type GaN layer. As shown in Figure 6.1b, lateral LEDs with a mesa size of 0.33 × 0.33 mm^2 were fabricated by a standard photolithography technique. A film of 100 nm ITO was deposited by an electron beam deposition technique and then annealed by a rapid thermal annealing process in order to form transparent p-type contact. N-type contact was formed on n-GaN by depositing Ti/Al/Ti/Au alloys. Finally, Ti/Au was deposited as a pad electrode on both p-type contact and n-contact as usual.

6.3 Result and Discussion

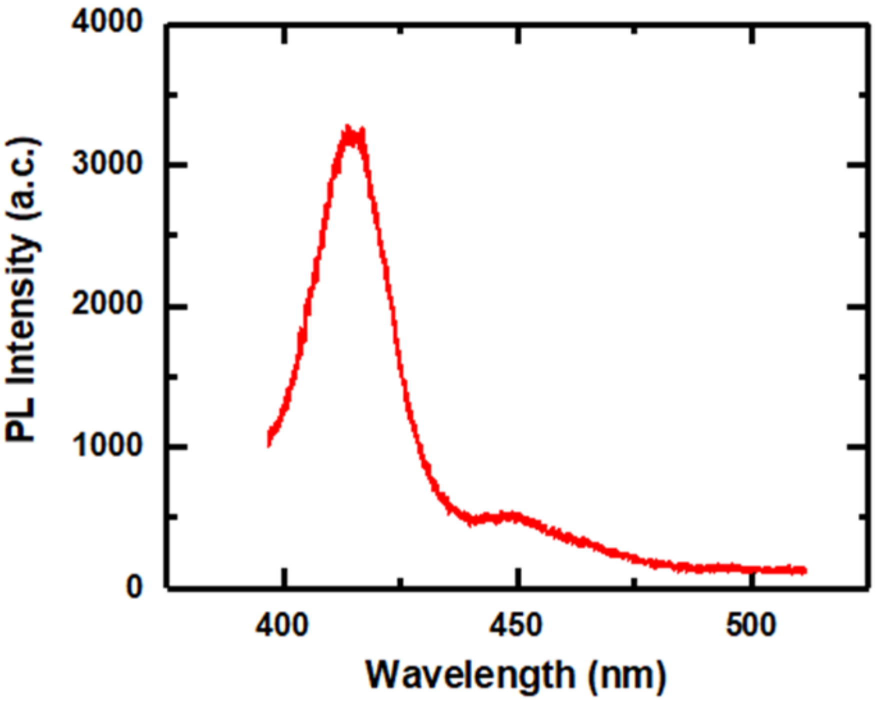

Figure 6.2. PL Emission spectra of a nonpolar InGaN/GaN MQW LED at room temperature.

PL measurements are performed on the LED sample using a 375 nm diode laser as an excitation source. The luminescence was dispersed by a 0.55 m monochromator and then detected by a Jobin Yvon CCD. Figure 6.2a shows the PL spectrum of the nonpolar LED sample measured at room temperature, indicating that the emission is dominated by an emission peak at around 418 nm.

Another weak emission has been observed on the longer wavelength side, at about 448 nm. In order to explore the origin of the double emission peaks from the InGaN/GaN MQWs, confocal PL measurements have been carried out using a 375nm laser source with a WiTec confocal microscopy and an optical microscope system, where the laser beam has been focused into a diameter of 200 nm. The emission is collected into a Horiba CCD, through a 300 nm grating.

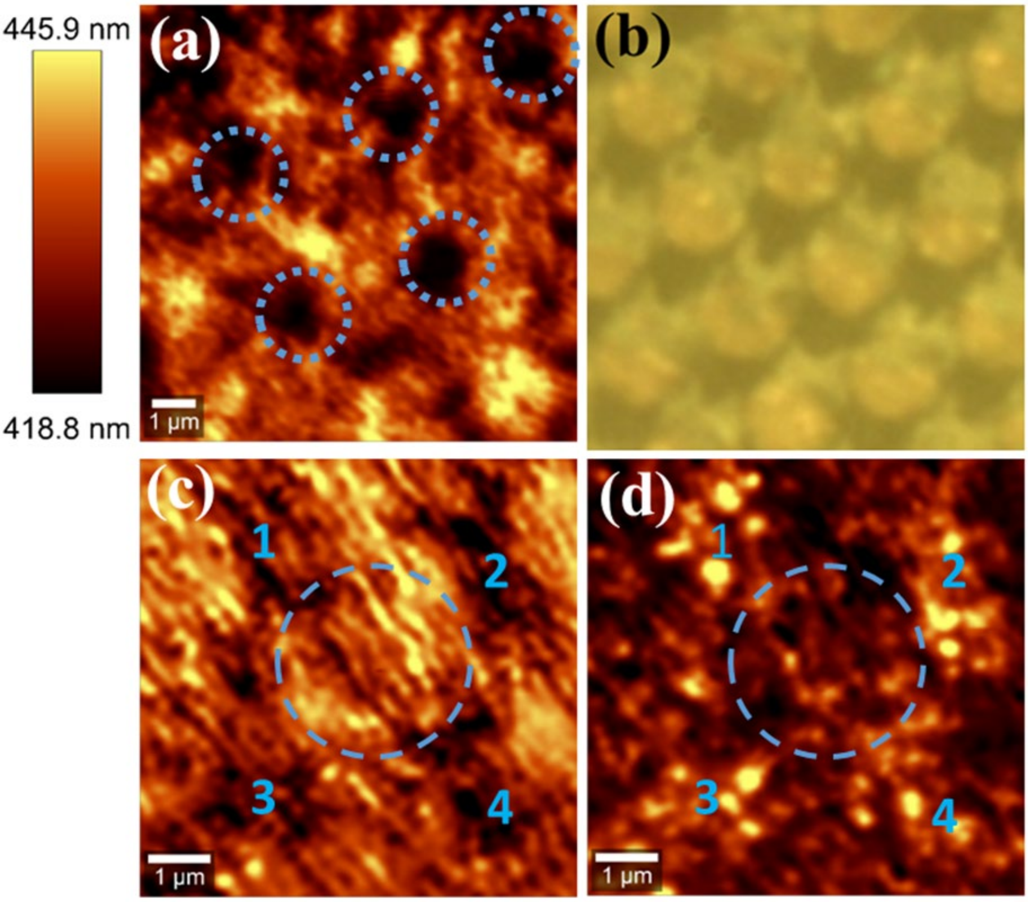

Figure 6.3. A wavelength map of confocal PL (a) and a microscope photo (b) for the nonpolar LED. The intensity maps of confocal PL with 418 nm (c) and 448 nm (d) emission for the nonpolar LED.

Figure 6.3a shows a typical wavelength mapping within an area of 10 μm × 10 μm, using a wavelength range from 418.8 nm to 445.9 nm. It is noted that the areas of dark regions and bright regions in the map form a distribution with a regular pattern. Comparing with the micro-rod pattern in Figure 6.3b, it is found the dark regions in the map marked by dashed circles correspond to the surface areas above micro-rods, and the bright regions corresponding to the surface areas above the micro-rod gaps. Furthermore, the 5 μm×5 μm intensity maps, which focus around one micro-rod, are taken using a filter of 418 nm and of 448 nm. In the map of 418 nm emission (Fig. 6.3c), the intensity is generally high across the map, except that a few positions around the micro-rod are dark, marked by 1, 2, 3 and 4. In contrast, these positions show the largest intensities in the map of 480 nm emission (Fig.6.3d). It indicates that the distribution of indium composition in the InGaN/GaN MQWs is related to the micro-rod patterned template for the GaN overgrowth, though a detailed investigation on the mechanism of indium composition variation is in progress.

Electroluminescence (EL) measurements are performed on bare-chip devices at room temperature in a continuous wave mode, using a microscope station with a Keithley 2400 source meter. Figure 6.4a shows the EL spectra measured at different injection currents. At low currents, only the emission with the longer wavelength is observed. The main emission with the shorter wavelength appears at higher currents, and the intensity increases with the increase of the injection current. At 100 mA current, the emission with the shorter wavelength becomes dominant over the spectrum. When the driving current is low, recombination has more chances of taking place at the QW energy band with a lower energy. At higher driving currents when the lower energy band is filled, excitons start to diffuse into the QW energy band with a higher energy. It is important to note, with the current increases from 10 mA to 100 mA, the wavelength of the main emission shifts only about 1.6 nm. It indicates suppression of piezoelectric field-induced QCSE in the nonpolar InGaN/GaN MQWs, and that the piezoelectric field is nearly eliminated in the nonpolar LED. Moreover, current-voltage (I-V) characteristic are displayed in Figure 6.4b, showing a good electrical property of the non-polar LED. The integrated EL intensity as a function of current is plotted in the inset of Fig. 6.4b, which increases linearly with increasing the current without any saturation tendency.

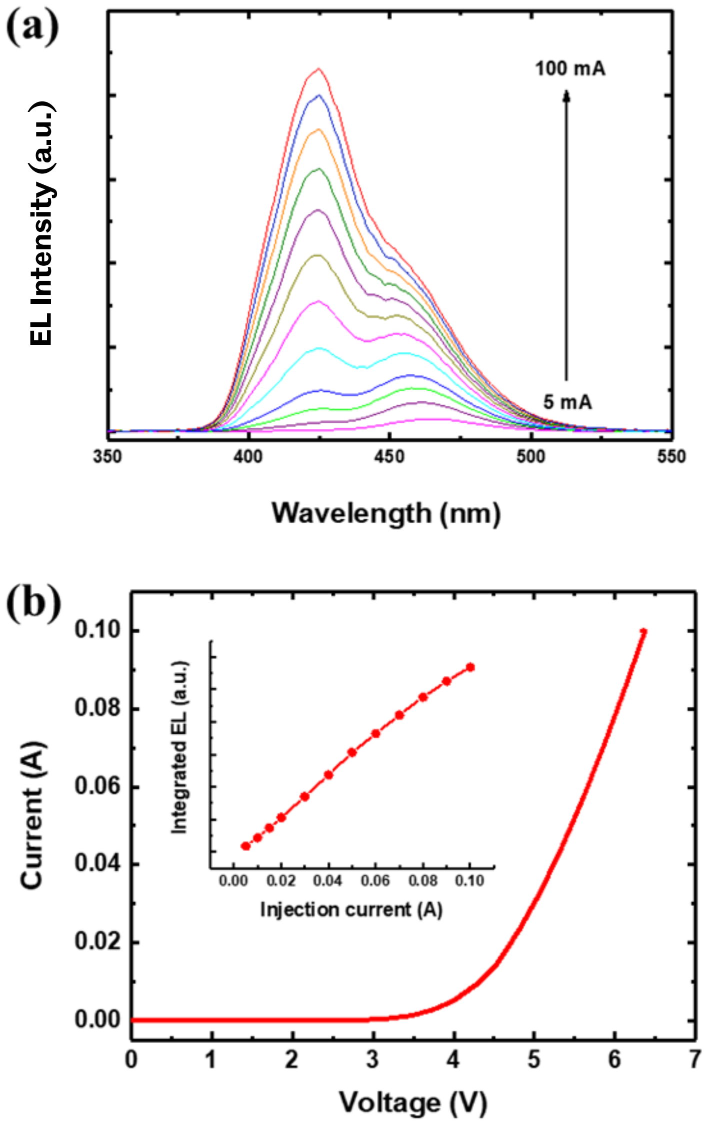

Figure 6.4. (a) EL spectra of the non-polar LED measured at different injection currents. (b) I-V characteristic, the inset is integrated EL as a function of injection current.

As we know, original valence band of a nonpolar InGaN/GaN QW system are broken into the sub-bands of |Y>, |Z>, and |X> states due to anisotropic strain, which are in order of decreasing electron energy[4]. The transition from the conduction band to the |Y> state is related to the light with polarization parallel to m-axis (perpendicular to the c-axis), whereas the transition involving the |Z> state occurs at a higher energy under polarization parallel to the c-axis. In order to investigate the polarization properties of the non-polar LED, polarized EL spectra are obtained from the top surface of the LED using on-wafer measurements, by rotating a polarizer positioned between the device and a spectrometer. During the experiments, the intrinsic polarization of the measurement system is taken into consideration, which has proven the c-plane LEDs to have negligible polarization characteristics.

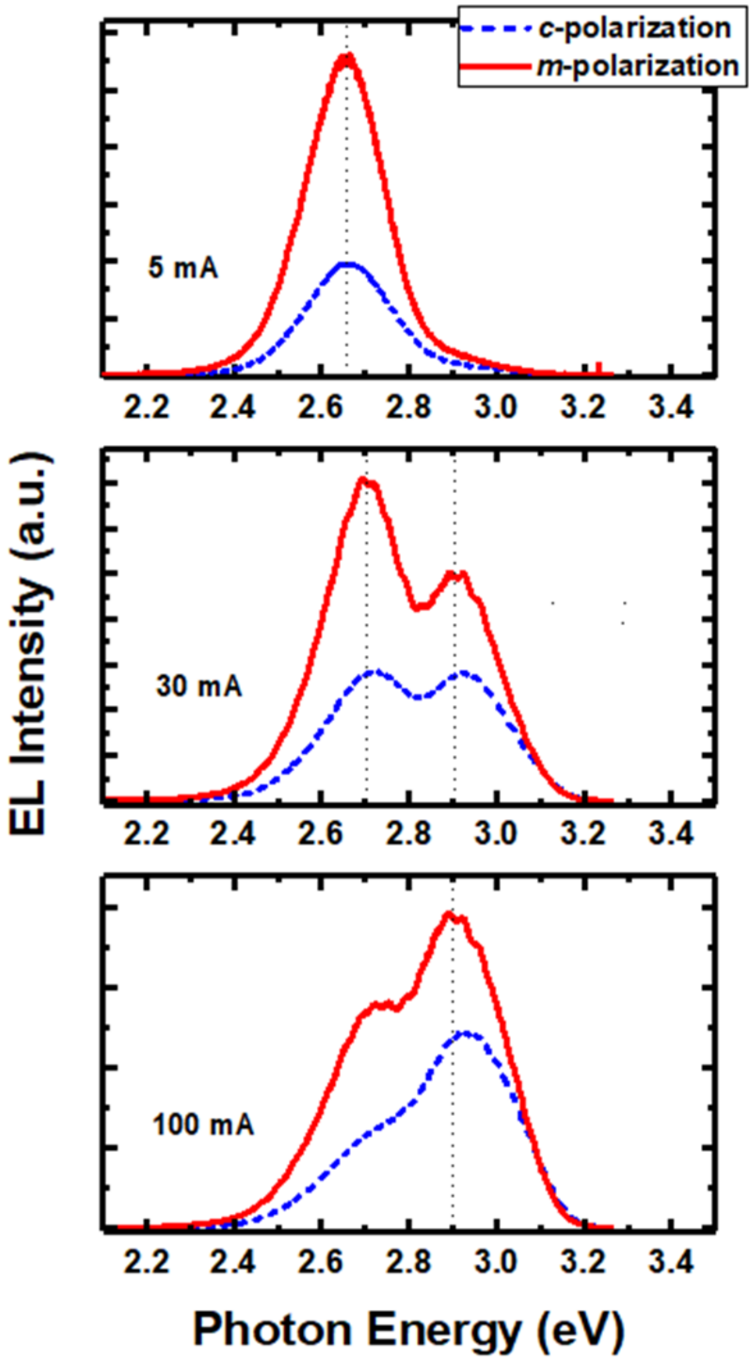

Figure 6.5. EL spectra with c-polarization and m-polarization at 5 mA, 30 mA and 100 mA.

Figure 6.5 shows the spectra along c-polarization and m-polarization measured at different driving currents of 5 mA, 30 mA, and 100 mA. Generally, the EL intensities with m-polarization are larger than those with c-polarization. Importantly, for the spectra at 30 mA with two emission peaks observed clearly, the intensity difference between the m-polarized light and the c-polarized light is bigger for the low-energy peak in comparison with the high-energy peak. It suggests the low-energy peak is more polarized than the high-energy peak. As we know, the increase in the indium composition induces the increase in anisotropic in-plane strain effect, resulting in a larger energy separation between the |Z> and |Y> states and a higher polarization ratio.

Figure 6.6 shows the normalized integrated intensities of nonpolar LEDs as a function of polarization angle. Due to the double emissions, the intensities are integrated across different energy ranges for the main emission (peak 1) and the low-energy emission (peak 2), respectively. Polarization ratio is defined as $(I_m - I_c)/(I_m + I_c)$, where I_m and I_c represent the integrated EL intensities parallel to the m and c directions, respectively. At 30 mA current, ρ is 0.34 and 0.49 for peak 1 and peak 2, respectively, which confirms that higher indium composition leads to a larger polarization degree. The ρ values obtained are comparable with other reports for nonpolar blue LEDs[15-18]. Actual polarization degrees for the nonpolar LED should be larger than the values obtained, because no special processing, such as using a confocal microscope or black absorber applied to bottom and side surfaces of devices[19], were performed in our measurements to reduce light scattering which severely affects the polarization. Furthermore, it is found that the polarization ratios for both emissions are nearly independent of injection current. When the light intensity is integrated across the whole energy range, the value of the double emission is found to decrease with the increase of the current, due to the current dependence of the two emissions with different ρ values.

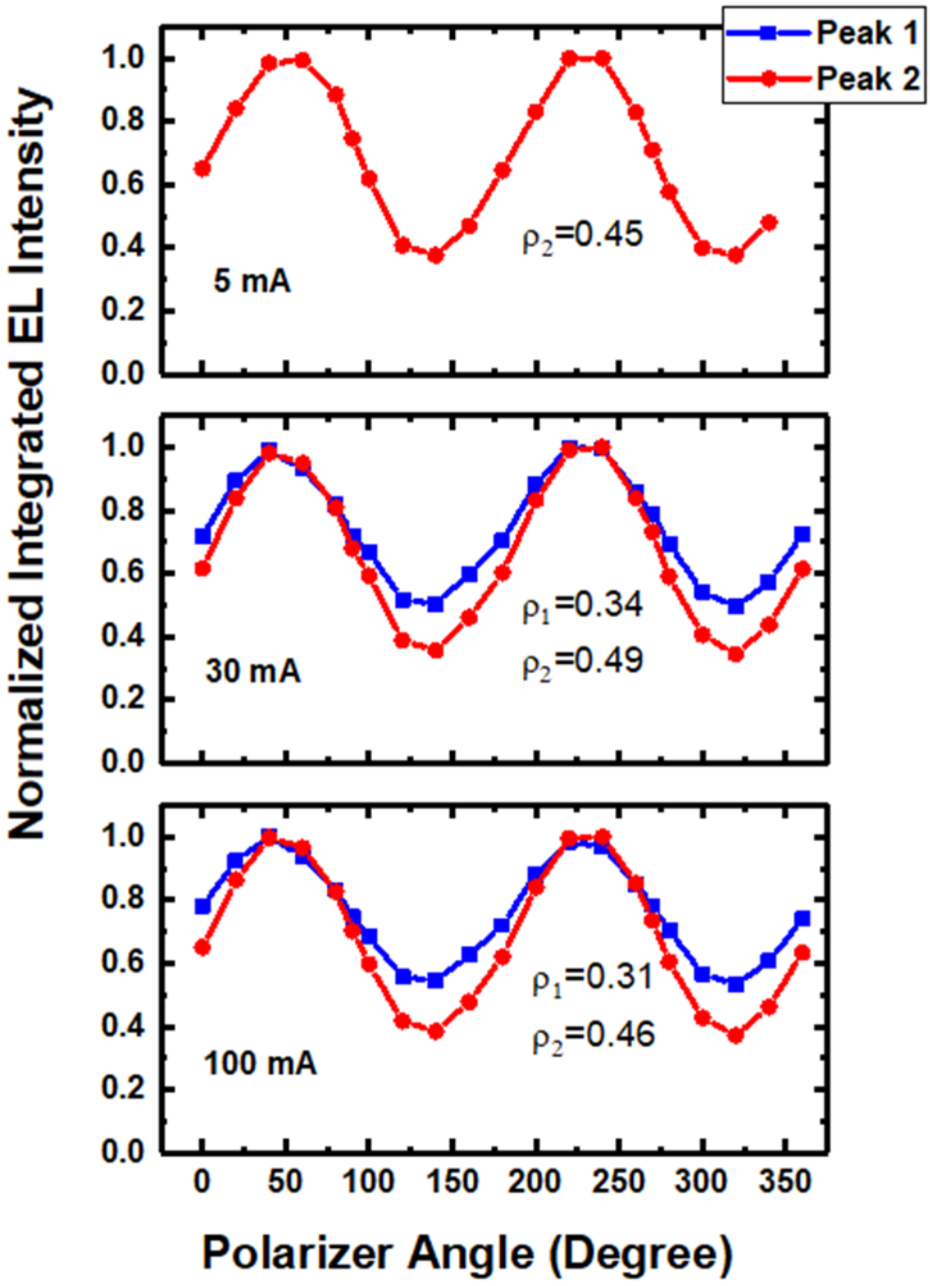

Figure 6.6. Polarization ratios for the 418 nm (peak 1) and 448 nm (peak 2) emissions at 5 mA, 30 mA and 100 mA.

The photon-energy difference ΔE between the emission spectra associated with the two polarizations is a useful quantity to estimate the energy difference between the |Z> and |Y> states. It is worth noting that the energy difference ΔE changes with the driving current. As shown in Figure 6.5, at 5 mA, there is no apparent energy shift (~8 meV) for peak 2, though a noticeable tail can be observed on the high-energy side of the c-polarized emission through normalized EL spectra. The energy shifts ΔE at 30 mA are about 20 meV and 16 meV for peak

1 and peak 2, respectively. At 100 mA, ΔE is increased to be 31 meV for peak 1. It means that ΔE increases with the driving current for both emissions, which is consistent with other reports on *m-plane* InGaN MQW LEDs[19,20]. It was explained by the anti-crossing of |Z> and |Y> subbands, or crystal momentum conservation. However, according to the calculation[4], there is no band mixing for a-plane InGaN/GaN QWs along the wave vector k_x direction. It is more likely related to the conversion of the crystal momentum upon recombination. Because the effective mass of the |Y> state is larger than that of the |Z> state, electron transitions to the |Y> state with large wave vectors *k* are suppressed due to the crystal momentum conservation. With increasing the current when the carriers are filling the states with larger *k*, the transition energy to the |Z> state increases faster than that to |Y>, hence resulting in larger ΔE values at increased currents.

6.4 Summary

In summary, nonpolar a-plane InGaN MQW LEDs have been achieved on high quality GaN grown on micro-rod templates. A double emission is observed for the nonpolar LED, which is found to be related to the overlying micro-rod template. The effect of piezoelectric field on optical properties is not observed in the power-dependent EL measurements. The polarization ratios for both emissions are nearly independent of the driving current, with a larger polarization degree for the emission with higher indium composition. The energy separation between m-polarized and c-polarized lights increases with the current for both emissions.

Reference

1. Bernardini, F., Fiorentini, V., & Vanderbilt, D. Spontaneous polarization and piezoelectric constants of III-V nitrides. Phys. Rev. B 56, R10024 (1997)

2. Waltereit, P., Brandt, O., Trampert, A., Grahn, H. T., Menniger, J., Ramsteiner, M., Reiche M., & Ploog, K. H. Nitride semiconductors free of electrostatic fields for efficient white light-emitting diodes. Nature 406, 865–868 (2000)

3. Takeuchi, T., Amano, H., & Akasaki, I. Theoretical Study of Orientation Dependence of Piezoelectric Effects in Wurtzite Strained GaInN/GaN Heterostructures and Quantum Wells. Jpn. J. Appl. Phys. 39, 413-416 (2000)

4. Huang, H., & Wu, Y. Study of polarization properties of light emitted from a-plane InGaN/GaN quantum well-based light emitting diodes. J. of Appl. Phys. 106, 023106 (2009)

5. Brinkley, S. E., Lin, Y. D., Chakraborty, A., Pfaff, N., Cohen, D., Speck, J. S., Nakamura, S., & DenBaars, S. P. Polarized spontaneous emission from blue-green m-plane GaN-based light emitting diodes. Appl. Phys. Lett. 98, 011110 (2011)

6. Masui, H., Chakraborty, A., Haskell, B. A., Mishra, U. K., Speck, J. S., Nakamura, S., & DenBaars, S. P. Polarized Light Emission from Nonpolar InGaN Light-Emitting Diodes Grown on a Bulk m-Plane GaN Substrate. Jpn. J. Appl. Phys. 44, L1329–L1332 (2005)

7. Yoshizumi, Y., Adachi, M., Enya, Y., Kyono, T., Tokuyama, S., Sumitomo, T., Akita, K., Ikegami, T., Ueno, M., Katayama, K., & Nakamura, T. Continuous-Wave Operation of 520 nm Green InGaN-Based Laser Diodes on Semi-Polar {2021} GaN Substrates. Applied Physics Express 2, 092101 (2009)

8. Zhong, H., Tyagi, A., Fellows, N. N., Chung, R. B., Saito, M., Fujito, K., Speck, J. S., DenBaars, S. P., & Nakamura, S. Demonstration of high power blue-green light emitting diode on semipolar (112-2) bulk GaN substrate. Electron. Lett. 43, 825-826 (2007)

9. Zakharov, D. N., Liliental-Weber, Z., Wagner, B., Reitmeier, Z. J., Preble E. A., & Davis, R. F. Structural TEM study of nonpolar a-plane gallium nitride grown on (11-20) 4H-SiC by organometallic vapor phase epitaxy. Phys. Rev. B 71, 235334 (2005)

10. Smalc-Koziorowska, J., Tsiakatouras, G., Lotsari, A., Georgakilas, A., & Dimitrakopulos, G. P. The defect character of GaN growth on r-plane sapphire. J. Appl. Phys. 107, 073525 (2010)

11. Imer, B., Wu, F., & DenBaars S. P., Speck, J. S. Improved quality (112-0) a-plane GaN with sidewall lateral epitaxial overgrowth. Appl. Phys. Lett. 88, 061908 (2006)

12. Iida, D., Iwaya, M., Kamiyama, S., Amano, H., & Akasaki, I. One-sidewall-seeded epitaxial lateral overgrowth of a-plane GaN by metalorganic vapor-phase epitaxy., J. Crystal Growth 311, 2887-2890 (2009)

13. Jiu, L., Gong, Y., & Wang, T. Overgrowth and strain investigation of (11–20) non-polar GaN on patterned templates on sapphire, Scientific Reports 8, 9898 (2018)

14. Wang, T., Bai, J., Parbrook, P. J., & Cullis, A. G. Air-bridged lateral growth of an $Al_{0.98}Ga_{0.02}N$ layer by introduction of porosity in an AlN buffer. Appl. Phys. Lett. 87, 151906 (2005)

15. Seo, Y. G., Baik, K. H., Song, K. M., Lee, S., Yoon, H., Park, J. H., Oh, K., & Hwang, S. M. Milliwatt-class non-polar a-plane InGaN/GaN light-emitting diodes grown directly on r-plane sapphire substrates, Current Applied Physics 10, 1407-1410 (2010)

16. Chiu, C. H., Kuo, S. Y., Lo, M. H., Ke, C. C., Wang, T. C., Lee, Y. T., Kuo, H. C., Lu, T. C., & Wang, S. C. Optical properties of -plane InGaN/GaN multiple quantum wells on non-polar sapphire substrates with different indium compositions. J. of App. Phys. 105, 063105 (2009)

17. Seo, Y. G., Baik, K. H., Song, H., Son, J. S., Oh, K., & Hwang, S. M. Orange non-polar InGaN/GaN light-emitting diodes grown on r-plane sapphire substrates. Optics Express 19, 12919 (2011)

18. Chou, Y., Li, H. W., Yin, Y. F., Wang, Y. T., Lin, Y. C., Lin, D. W., Wu, Y. R., Kuo, H. C., & Huang, J. J. Polarization ratio enhancement of a-plane GaN light emitting diodes by asymmetric two-dimensional photonic crystals. J. of Appl. Physics 115, 193107 (2014)

19. Brinkley, S. E., Lin, Y. D., Chakraborty, A., Pfaff, N., Cohen, D., Speck, J. S., Nakamura, S., & DenBaars, S. P. Polarized spontaneous emission from blue-green mm-plane GaN-based light emitting diodes. Appl. Phys. Lett. 98, 011110 (2011)

20. Masui, H., Yamada, H., Iso, K., Nakamura, S., & DenBaars, S. P. Optical polarization characteristics of m-oriented InGaN/GaN light-emitting diodes with various indium compositions in single-quantum-well structure. J. Phys. D: Appl. Phys. 41, 225104 (2008)

Chapter 7

Non-polar (11-20) GaN Grown on Sapphire with Double Overgrowth on Micro-rod/stripe Templates

Non-polar (11-20) GaN with low defect density can be achieved on sapphire by means of overgrowth on a micro-rod template recently developed, or on a conventional ⟨1-100⟩-oriented stripe template. The overgrowth on stripes block BSFs in the nonpolar GaN more effectively, but it is difficult to obtain a flat GaN surface due to its anisotropic pattern for overgrowth. The overgrowth on micro-rods can significantly reduce dislocations, simultaneously maintaining a smooth sample surface. Very recently, we develop a double overgrowth approach to grow (11- 20) GaN on sapphire, i.e. first overgrowth on stripes and second overgrowth on micro-rods. The double overgrowth technique successfully utilizes the strengths of the two kinds of overgrowths, further improving crystal quality, which will be a very promising approach to achieve high quality (11-20) GaN for large-scale industrial production.

7.1 Introduction

III-nitride semiconductors grown along either non-polar orientations are expected to exhibit unique performance in comparison with their c-plane counterparts in both electronics and photonics. It is well-known that c-plane III-nitride optoelectronics suffer from polarization-induced electric fields, leading to the so-called quantum confined Stark effect and thus a reduction in quantum efficiency[1-3]. Therefore, III-nitride light emitting diodes grown along a non-polar orientation are expected to lead to a significant improvement in internal quantum efficiency. In terms of electronics, GaN exhibits major advantages in fabricating high-power, high frequency and high-temperature devices due to its intrinsically high breakdown voltage, high saturation electron velocity and excellent mechanical hardness[4,5]. So far, III nitride based electronics are overwhelmingly dominated by AlGaN/GaN heterostructure field transistors (HFETs) grown on c-plane GaN surface[6,7], where strong polarisation formed across the interface between AlGaN and GaN leads to a high sheet carrier density of up to 10^{13} cm^{-2} obtained without modulation doping[1,8] and a depletion-mode transistor. However, practical applications ideally require enhancement-mode devices due to safety requirements. Furthermore, the sheet carrier density of a two-dimensional electron gas formed at the interface between GaN and AlGaN depends sensitively on polarisation. As a result, any change in strain would also affect the electrical performance of such HFETs, potentially leading to performance degradation and reliability issues[9-11]. In order to address these challenges, a simple but promising solution is to grow an AlGaN/GaN heterostructure with modulation doping along a non-polar direction, where the polarisation can be eliminated and thus the sheet carrier density of 2DEG can be tuned simply through optimising the doping level in AlGaN barrie[8].

Up to date non-polar III-nitride devices with high performance have to be grown on extremely expensive GaN substrates[12,13], where the size of GaN substrates is typically limited to a size of 10 × 10 μm^2 and thus such GaN substrates are not attractive to the industry at all. The crystal quality of current non-polar GaN grown on either sapphire or silicon is far from satisfactory. Typically, non-polar GaN grown on sapphire without any extra processes exhibits a dislocation density of above 10^{10} cm^{-2} and a stacking fault density of above 10^6 cm^{-1} [14,15], Therefore, it is crucial to develop a new method for the growth of non-polar GaN on industry-compatible substrates, such as sapphire or silicon. Conventional epitaxial lateral overgrowth (ELOG) and related techniques have been employed to improve the crystal quality of nonpolar or semi-polar GaN on sapphire[16-19], which are based on selective area overgrowth on normally stripe-patterned templates. Very recently, it has been found that such patterning leads to two major issues, although the crystal quality of non-polar GaN can be improved. Overgrowth on such stripe-patterned templates potentially generates severe non-uniformity, in particular, strain distribution, which in return strongly affects the electrical performance of non-polar III-nitride electronics[20]. Secondly, it is also difficult to employ such a stripe-patterned template to achieve quick coalescence and an atomically flat surface as a result of intrinsically anisotropic in-plane growth rate[20].

7.2 Methods

In order to address these great challenges, our group has achieved regularly arrayed non-polar (11-20) GaN micro-rods with a mushroom configuration on r-plane sapphire, using a dry-etching technique and subsequent ultra-violet (UV) assisted photo-enhanced chemical (PEC) etching processe[20]. Overgrowth on such a template allows us to obtain quick coalescence and an atomically flat surface as a result of our designed patterning which can compensate for the intrinsically anisotropic in-plane growth rate of non-polar GaN. Significant improvement in crystal quality has been achieved. More importantly, an excellent uniformity in strain distribution is also achieved across a 2-inch wafer. Very recently, we further combine the above approach with the conventional stripe-pattern based ELOG approach, leading to non-polar GaN with a step-change in crystal quality. In this paper, by means of scanning electron microscopy (SEM) and transmission electron microscopy (TEM), we comparatively study three kinds of overgrown (11-20) GaN layers on sapphire, namely, overgrown GaN on our micro-rod template (labelled as sample A), overgrown GaN on a standard stripe template (labelled as sample B), and overgrown GaN on stripes first and then on micro-rods (labelled as sample C). The mechanisms of defect reduction have been investigated, which are extremely important for further improvement of crystal quality.

First, non-polar (11-20) GaN is grown on *r*-plane sapphire, by a standard metal organic chemical vapour deposition (MOCVD) using our high temperature AlN buffer technology[21]. Subsequently, the as-grown template is fabricated into a regularly arrayed micro-rod template (for sample A growth), or a ⟨1-100⟩-oriented stripe template (for sample B growth). For sample C, an as-grown template is fabricated to a stripe template on which first overgrowth of nonpolar GaN is carried out and the regrown GaN is then further formed into a micro-rod template on which second overgrowth is carried out. Schematic drawings as shown in Fig. 7.1 display the approaches of the growth of sample A, sample B, and sample C, respectively. The fabrication of the patterned templates is descried in detail in[20].

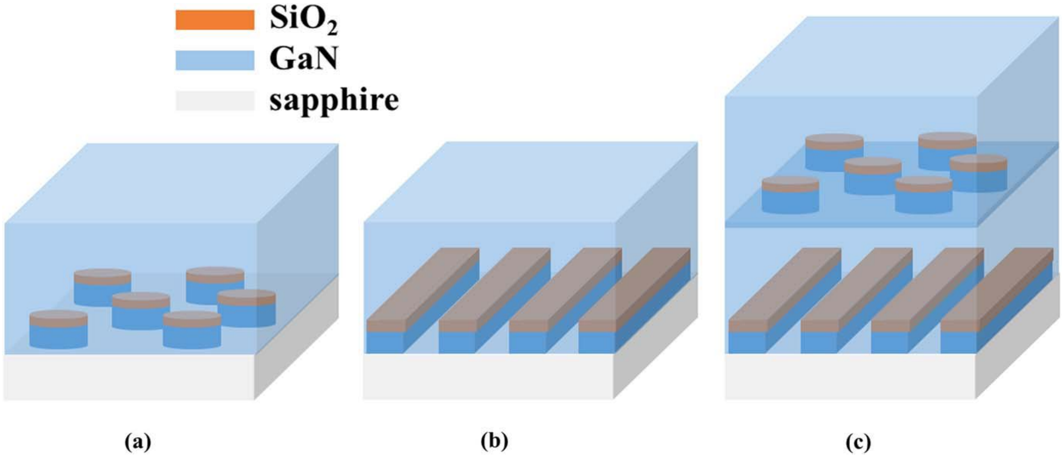

Figure 7.1. Schematic of (a) sample A, (b) sample B, and (c) sample C overgrown on sapphire substrates.

Fig. 7.2a shows a typical SEM image of a micro-rod template. Both the diameter and spacing of micro-rods are 2.5 μm. Note that the diagonal line of micro-rod square is deliberately made along c-direction of (11-20) GaN, so that the micro-rod spacing along c-direction is larger than those along other directions. A standard stripe pattern template is shown in Fig. 7.2b, where the parallel stripes orientate along the ⟨1-100⟩ direction, with both width and spacing of 1.5 μm. In both cases, the etching is performed down to the sapphire substrate and the formed SiO_2 mask remains on top of GaN micro-rods/stripes. The heights of micro-rods and stripes in the three samples are all about 1 μm. Before the overgrowth, the templates further undergo PEC etching in a KOH solution under UV illumination for 60 min. Due to the orientation dependence of the PEC etching, the micro-rods are etched from (000-1) facets while (0001) facets are un-etched. As shown in Fig. 7.2c, 'mushroom' configuration is formed for the micro-rods, which is expected to effectively suppress the ⟨000-1⟩ overgrowth. The stripes in Fig. 7.2d also demonstrate an undercut configuration of (000-1) sidewalls.

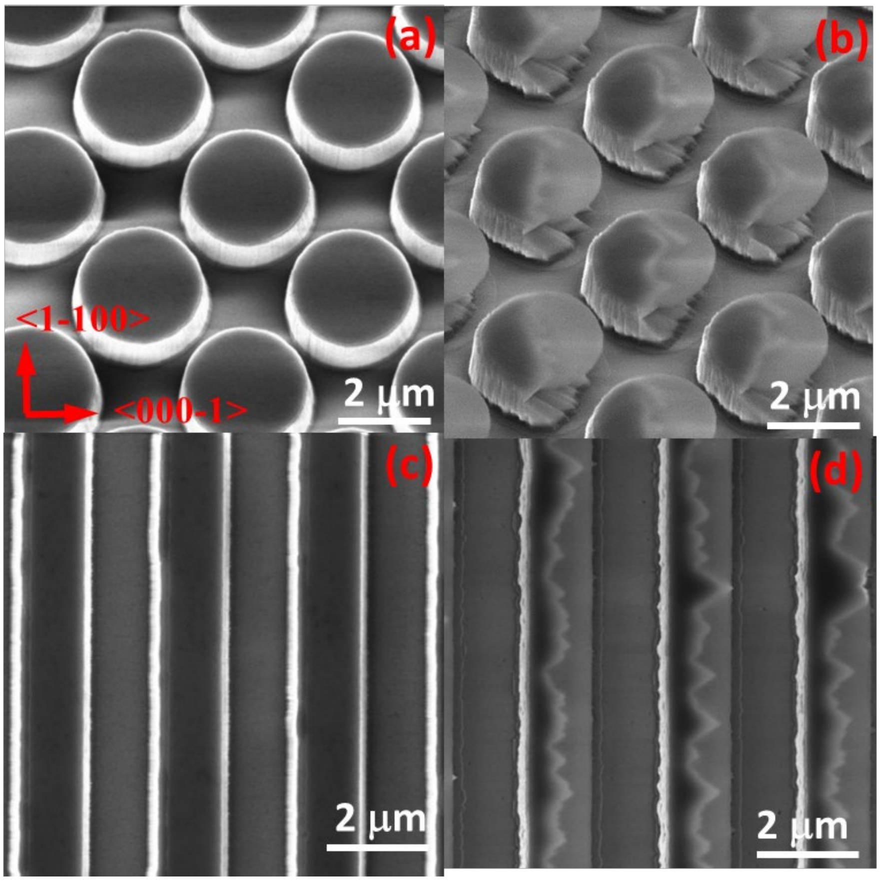

Figure 7.2. SEM images of a micro-rod template (a) before and (b) after KOH solution etching, and a stripe template (c) before and (d) after KOH solution etching, for the overgrowth of nonpolar GaN.

Subsequently, the micro-rod template is reloaded into the MOCVD reactor chamber for the GaN overgrowth. The growth pressure, growth temperature and V/III ratio are 118 torr, 1130 °C, 1800, respectively. Figure 7.3a shows the surface of (11-20) GaN overgrown after 4000 s on the micro-rod template. At this stage, the gap between the micro-rods has been completely filled. Though the ⟨0001⟩ growth rate can be much faster than those along other orientations, our unique pattern configuration of micro-rods where spacing distance along c-direction is larger than those along other directions, helps compensate the intrinsically anisotropic growth rate of nonpolar GaN. It thus leads to a quick completion of first coalescence. With the vertical growth becoming dominant, the overgrown GaN layer exceeds the height of the micro-rods, and the second coalescence is happening above the SiO_2 masks. Consequently, regularly spaced pits appear on the surface with each pit above each micro-rod (Fig. 7.3a). A full coalescence can be achieved after 8000 s (~3 μm) growth for the GaN on the micro-rod template, finally forming a smooth surface (Fig. 7.3b). However, it is not available for the overgrowth of nonpolar GaN on the stripe template. Figure 7.3c shows the surface of (11-20) GaN after 4000 s growth on the strip template. Due to that the ⟨000-1⟩ growth is suppressed, the priority ⟨0001⟩ growth, starting from +c face sidewalls of stripes, leads to the overgrown GaN in form of stripes. Simultaneously, GaN is grown along the vertical direction. As a result, when the +c face of one GaN stripe is meeting with the −c face of the neighbouring GaN stripe, the thicknesses of the two GaN stripes at the meeting place have a large difference, which produces a ⟨1-100⟩-oriented slit. The thickness difference cannot be smoothed out after 8000 s growth. As shown in Figure 7.3d, there are still a large density of stripy pits remained on the surface. The large non-uniformity in the nonpolar GaN growth on the stripe template is attributed to both its anisotropic pattern shape and the intrinsically anisotropic growth rate.

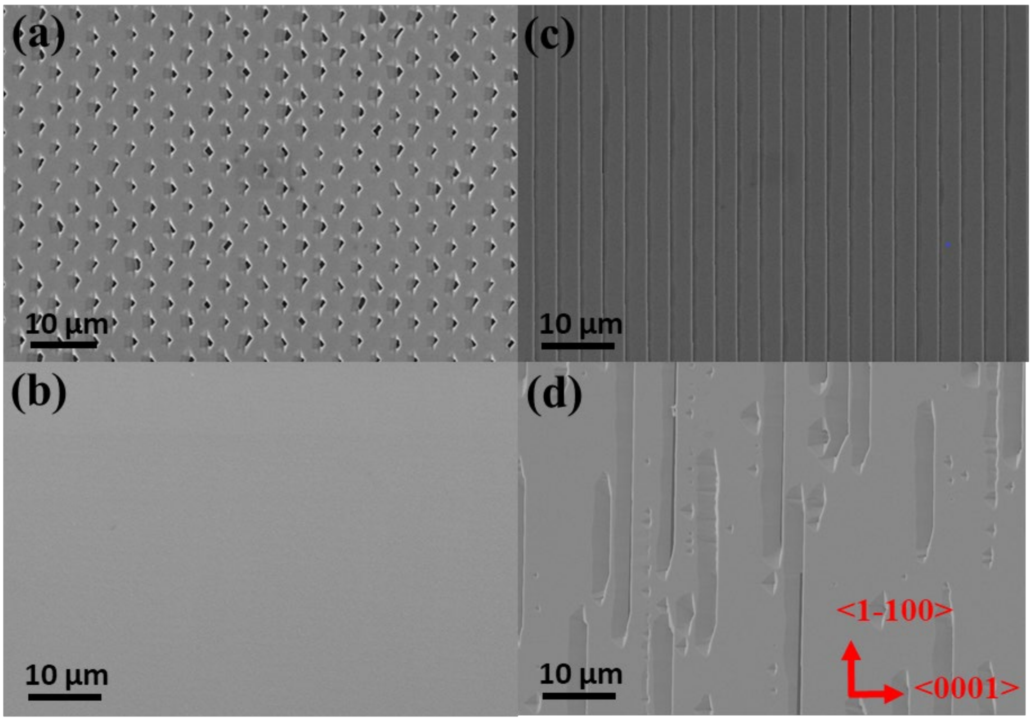

Figure 7.3. Plan-view SEM images of nonpolar GaN after (a) 4000 s and (b) 8000 s growth on a micro-rod template, and nonpolar GaN after (c) 4000 s and (d) 8000 s growth on a stripe template.

For sample A, sample B and sample C studied in this paper, the layer thicknesses of each overgrowth are identical, about 3 µm. The crystal qualities of the three nonpolar (11- 20) GaN samples are characterized by high resolution x-ray rocking curve (XRC) measurements as a function of azimuth angle, using a Bruker D8 high resolution x-ray diffractometer with Cu Kα radiation source (1.5418 Å) at the energy of 40 kV and 40 mA. The azimuth angle is defined as 0° when the projection of an incident x-ray beam on a nonpolar (11- 20) GaN surface is parallel to the c direction of (11-20) GaN, while it is defined as 90° when the projection of the incident x-ray beam is along the [1-100] direction, i.e. m direction.

7.3 Result and Discussion

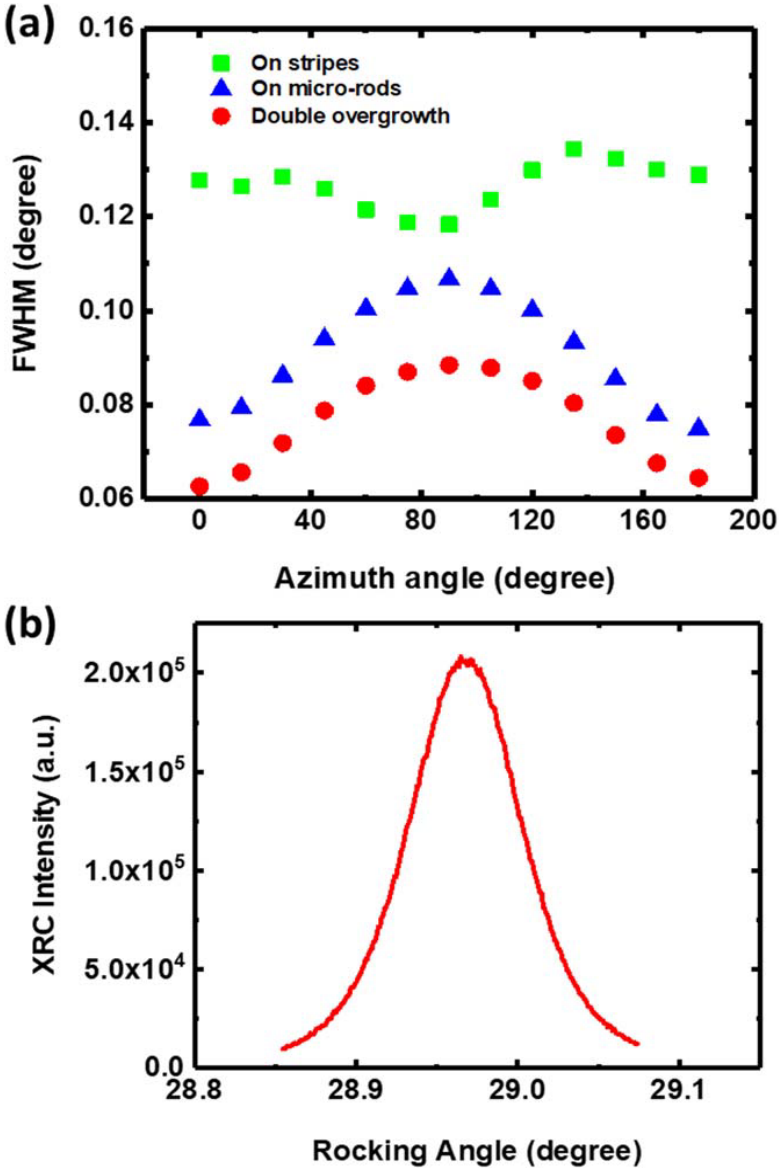

Figure 7.4. (a) The FWHMs of on-axis x-ray rocking curves as a function of azimuth angle for nonpolar (11-20) GaN grown on stripes, on micro-rods, and with double overgrowth approach. (b) X-ray rocking curve at azimuth angle of 90° for nonpolar GaN with double overgrowth approach.

Figure 7.4a shows the full width at half maximum (FWHM) of on-axis XRC as a function of azimuth angle for the three samples. For sample A, the FWHMs are 0.075° along the [0001] direction and 0.105° along the [1-100] direction, respectively, which are dramatically reduced compared to the 0.33° and 0.52° arcsec for the as-grown template (not shown here). With a similar thickness, sample B has broader FWHMs than sample A. Importantly, the double-overgrown sample demonstrates the smallest FWHM values among the three samples, with 0.063° along the [0001] direction and 0.087° along the [1-100] direction, respectively, which are the best report for non-polar (11-20) GaN on sapphire so far. As an example, the XRC at azimuth angle of 90° of sample C is presented in Fig. 7.4b. It indicates that the double overgrowth approach can further improve the crystal quality of nonpolar GaN compared to the stripe-only overgrowth and the micro-rod-only overgrowth.

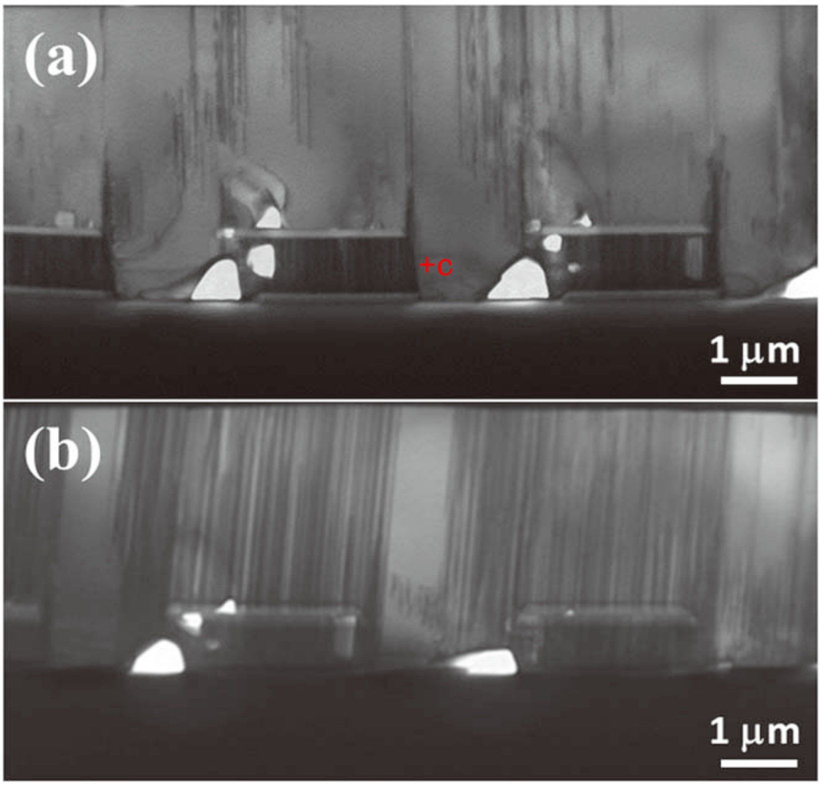

Figure 7.5. Cross-sectional TEM images of GaN grown on a micro-rod template, (a) taken around [1-100] zone-axis with g = 11-22 and (b) taken around [1-210] zone-axis with g = 10-10.

In order to gain insight into the origin of a significant improvement in crystal quality, microstructural characterisation is carried out on sample A and sample

C, using a Phillips EM 430 TEM operated at 200 kV with a point resolution of 0.2 nm. Figure 7.5a shows the typical cross-sectional TEM images of sample A, taken under two-beam conditions with g = 11-22 close to the [1-100] zone-axis, to observe threading dislocations (TDs) and partial dislocations. A TD is one that extends from the surface of a strained layer system and goes through the layer. It has three types in the wurtzite structure: edge-type, screw-type, and mixed-type.

In Fig. 7.5a, all three types of TDs and Frank partial dislocations can be observed. It is seen clearly that the dislocation density in the overgrown GaN is significantly reduced in comparison with the as-grown template existing in the form of micro-rods. The SiO_2 layer remained deliberately on the top of rods plays an important role in both blocking the dislocations and enhancing the lateral growth from rod sidewalls. At the bottom between two neighbouring micro-rods, one void is formed due to meeting of the GaN crystal growing along ⟨0001⟩ direction with the GaN crystal growing along ⟨000-1⟩ direction. As well known, the ⟨0001⟩ lateral growth of nonpolar GaN leads to defect-free GaN, while the ⟨000-1⟩ lateral growth allows defects to origin in the overgrown layers[22,23]. Therefore, the ⟨000-1⟩ faces of micro-rods in our case are deliberately etched by KOH solution to suppress the ⟨000-1⟩ growth. In addition, the ⟨0001⟩ growth rate can be much faster than the ⟨000-1⟩ growth by optimising growth conditions such as increasing the growth temperature, causing the ⟨000-1⟩-grown GaN to be confined near the N-face side of the micro-rod. Consequently, the overgrown GaN between the two micro-rods is nearly free of dislocations as shown in Fig. 7.5a. A small number of dislocations are only observed regularly in the upper part of overgrown GaN between two micro-rods, probably due to the growth from the nearby micro-rod on another row with a growth direction along ⟨1-100⟩.

One of the major planar defects in non-polar GaN is basal plane SFs (BSFs). Basal plane stacking faults (BSF) in the wurtzite structure can be treated as planar defects forming the ABC cubic structure locally within the usual ABABAB stacking sequence. In order to bring the BSFs in the non-polar GaN into contrast, it is necessary to tilt the specimen by ~30° from [1-100] zone-axis towards [1-210] zone-axis during a TEM observation. Figure 7.5b is a TEM image of sample A taken under g = 10-10 diffraction condition, where the BSFs in form of straight lines perpendicular to the surface can be seen clearly. Due to the ⟨0001⟩ lateral growth, BSFs diminished in some areas near the Ga-face side of micro-rods, because the original BSFs lying in basal planes could be impeded through the overgrowth only when the lateral growth proceeds normal to the basal planes, i.e. the ⟨0001⟩ growth. However, the BSF density is still high, especially around the micro-rods. This can be ascribed to the round sidewall of micro-rods, which causes the lateral growth to proceed along ⟨0001⟩ direction as well as along other directions, such as ⟨1-100⟩ direction, resulting in extending of pre-existing BSFs into the overgrown GaN layer.

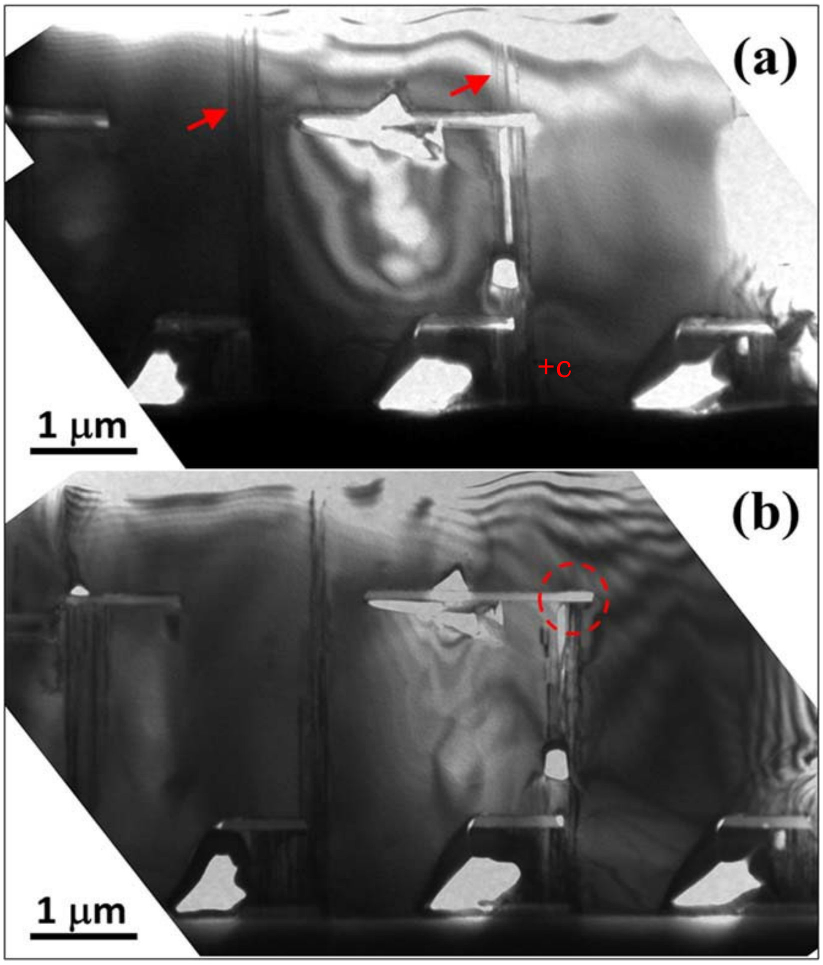

Figure 7.6. Cross-sectional TEM images of GaN grown with double overgrowth approach, (a) taken around [1-210] zone-axis with g = 10-10 and (b) taken around [1-100] zone-axis with g = 11-22.

In contrast, the overgrowth on stripe templates can impede BSFs in (11-20) GaN much more effectively, as the ⟨1-100⟩-oriented stripes have only (0001) and (-0001) facets, which make full use of the ⟨0001⟩ growth. Therefore, in our double-overgrowth approach, an overgrowth on the ⟨1-100⟩- oriented stripe template is employed as first step to efficiently block extending of BSFs in the as-grown template. It is clearly seen in Fig. 7.6a that the BSFs (marked by red arrows) are dramatically reduced compared to the as-grown template, with a density of ~1 × 10^4 cm^{-1}. Only a small amount of BSFs are observed near the Ga-face sidewall of each stripe, indicating they initiated where the ⟨0001⟩ growth just started. It is possibly ascribed to the inclined sidewall of stripes, which cannot ensure the growth from the stripes is totally along ⟨0001⟩ direction. With the vertical growth proceeding, the BSFs extend into the first-regrown GaN layer and even the second-regrown GaN layer. Due to that the SiO_2 layer for the second overgrowth is shaped as a disc with a diameter of 2.5 μm, it cannot completely block the BSFs lying along basal planes from penetrating into the second regrown GaN layer. However, the second overgrowth with micro-rod pattern can further reduce dislocations in the first regrown GaN layer. As shown in the image of Fig 7.6b, taken with g = 11-22 close to the [1-100] zone-axis where nearly all dislocations can be observed, some dislocations extending from the GaN overgrown on stripes are stopped under a SiO_2 disc (marked by red circle), leading to further reduction in dislocation density in the upper GaN layer. This is attributed to direct blocking by the SiO_2 layer or annihilation produced by the lateral growth during the second overgrowth process. According to plan-view TEM observation, the dislocation density is about 5 × 10^7 cm^{-2}.

7.4 Summary

We compared the nonpolar (11-20) GaN grown on regularly arrayed micro-rods, on ⟨1-100⟩-oriented stripes, and with a double overgrowth. The overgrowth on micro-rods can significantly reduce dislocations, simultaneously maintaining a smooth sample surface. The overgrowth on stripes block BSFs in the nonpolar GaN more effectively, but it is difficult to obtain a flat GaN surface due to its anisotropic pattern for overgrowth. The double overgrowth technique which employs the first overgrowth on stripes and the second growth on micro-rods, successfully utilizes the strengths of the two kinds of overgrowths and will be a very promising approach to achieve high quality nonpolar GaN for large-scale industrial production.

Reference

1. Bernardini F., Fiorentini V., & Vanderbilt D. Spontaneous polarization and piezoelectric constants of III-V nitrides. Phys. Rev. B 56, R10024-7 (1997).

2. Waltereit P., Brandt O., Trampert A., Grahn H T., Menniger J., Ramsteiner M., Reiche M. & Ploog, K. H. Nitride semiconductors free of electrostatic fields for efficient white light-emitting diodes Nature 406, 865-8 (2000)

3. Takeuchi T., Amano H., & Akasaki I., Theoretical study of orientation dependence of piezoelectric effects in wurtzite strained GaInN/GaN heterostructures and quantum wells Japan. J. Appl. Phys. 39, 413-6 (2000)

4. Asif Khan, M., Kuznia, J. N., Bhattarai, A. R. & Olson, D. T. Metal semiconductor field effect transistor based on single crystal GaN Appl. Phys. Lett. 62, 1786-7 (1993)

5. Wu, Y. F., Keller, B. P., Keller, S., Kapolnek, D., Kozodoy, P., Denbaars, S. P. & Mishra, U. K. Very high breakdown voltage and large transconductance realized on GaN heterojunction field effect transistors Appl. Phys. Lett. 69, 1438-40 (1996)

6. Yoshida, S., Ishii, H., Li, J., Wang, D. & Ichikawa, M. A. High-power AlGaN/GaN heterojunction field-effect transistor Solid. State. Electron. 47, 589-92 (2003)

7. Uemoto, Y. et. Al. 8300V blocking voltage AlGaN/GaN power HFET with thick poly-AlN passivation Tech. Dig. - Int. Electron Devices Meet. pp 861-4 (2007)

8. Paskova, T. Development and prospects of nitride materials and devices with nonpolar surfaces Phys. Status Solidi b 245, 1011-25 (2008)

9. Oku, T., Kamo, Y. & Totsuka, M. AlGaN/GaN HEMTs passivated by Cat-CVD SiN film Thin Solid Films 516, 545-7 (2008)

10. Chang, C. Y., Yu-Lin, W., Gila, B. P., Gerger, A. P., Pearton, S. J., Lo, C. F., Ren, F., Sun, Q., Yu, Z. & Han, J. Effect of gate orientation on dc characteristics of Si-doped nonpolar AlGaN/GaN metal-oxide semiconductor high electron mobility transistors Appl. Phys. Lett. 95, 082110 (2009)

11. Ishida, M., Kuroda, M., Ueda, T. & Tanaka, T. Nonpolar AlGaN/GaN HFETs with a normally off operation Semicond. Sci. Technol. 27, 024019 (2012)

12. Yoshizumi, Y. et. Al. Continuous-wave operation of 520 nm green InGaN-Based laser diodes on semi-Polar {20-21} GaN substrates Appl. Phys. Express 2, 092101 (2009)

13. Zhong, H., Tyagi, A., Fellows, N. N., Chung, R. B., Saito, M., Fujito, K., Speck, J. S., DenBaars, S. P. & Nakamura, S. InGaN/GaN quantum well structures with greatly enhanced performance on a-plane GaN grown using self-organized nano-masks Electron. Lett. 43, 825 (2007)

14. Zakharov, D. N., Liliental-Weber, Z., Wagner, B., Reitmeier, Z. J., Preble, E. A. & Davis, R. F. Structural TEM study of nonpolar a-plane gallium nitride grown on (11-20) 4H-SiC by organometallic vapor phase epitaxy Phys. Rev. B 7, 235334 (2005)

15. Smalc-Koziorowska, J., Tsiakatouras, G., Lotsari, A., Georgakilas, A. & Dimitrakopulos, G. P. The defect character of GaN growth on r-plane sapphire J. Appl. Phys. 107, 073525 (2010)

16. Imer, B. M., Wu, F., Denbaars, S. P. & Speck, J. S. Improved quality (11-20) a-plane GaN with sidewall lateral epitaxial overgrowth Appl. Phys. Lett. 88, 061908 (2006)

17. Ni, X., Özgür, Ü., Baski, A. A., Morkoç, H., Zhou, L., D Smith, J. & Tran, C. A. Epitaxial lateral overgrowth of (11-22) semipolar GaN on (1-100) m-plane sapphire by metalorganic chemical vapor deposition Appl. Phys. Lett. 90, 182109 (2007)

18. Iida, D., Iwaya, M., Kamiyama, S., Amano, H. & Akasaki, I. One-sidewall-seeded epitaxial lateral overgrowth of a-plane GaN by metalorganic vapor-phase epitaxy J. Crystal Growth 311, 2887-90 (2009)

19. Kriouche, N., Leroux, M., Vennégués, P., Nemoz, M., Nataf, G. & de Mierry, P. Filtering of defects in semipolar (11-22) GaN using 2-Steps lateral epitaxial overgrowth Nanoscale Res. Lett. 5, 1878-81 (2010)

20. Jiu, L., Gong, Y. & Wang, T. Overgrowth and strain investigation of (11-20) non-polar GaN on patterned templates on sapphire Sci. Rep. 8, 9898 (2018)

21. Wang, T., Bai, J., Parbrook, P. J. & Cullis, A. G. Air-bridged lateral growth of an Al0.98Ga0.02N layer by introduction of porosity in an AlN buffer Appl. Phys. Lett. 87, 151906 (2005)

22. Bai, J., Gong, Y., Xing, K., Yu, X. & Wang, T. Efficient reduction of defects in (1120) non-polar and (1122) semipolar GaN grown on nanorod templates Appl. Phys. Lett. 102, 101906 (2013)

23. Wang, T. Topical review: development of overgrown semi-polar GaN for high efficiency green/yellow emission Semicond. Sci. Technol. 31, 093003 (2016)

Chapter 8

Conclusions and Future Work

In this thesis, two kinds of novel overgrowth approaches to achieving high-quality non-polar III-nitrides have been presented, novel multiple-colour structures and non-polar InGaN/GaN LEDs based on the patterned templates have been obtained. Detailed investigation of structure and optical performance have been performed for further validation of our high quality and multiple-function patterned templates.

8.1 Summary of Results

8.1.1 Overgrowth of (11-20) GaN on Micro-rod Templates and Strain Investigation

By means of proper design and a combination of a standard photolithography and subsequent dry etching processes, regularly arrayed non-polar micro-rod GaN templates with special features have been fabricated. PEC etching has been further performed in order to create "mushroom configuration". Overgrowth has been conducted on the templates, leading to a major improvement in crystal quality compared to an as-grown GaN sample and an overgrown GaN on a stripe patterned template. The FWHM of XRC shows a massive reduction with a typical value of 270 arcsec along the [0001] direction and 380 arcsec along the [1-100] direction, respectively. The in-plane strain of overgrown (11-20) GaN was investigated by means of performing XRD and calculating from multiple symmetry and skew-symmetric reflections. The result indicates that the overgrown (11-20) GaN on our micro-rod templates exhibits an isotropic in-plane strain distribution while the distribution is highly anisotropic in both the as-grown GaN and the overgrown GaN on the stripe patterned template.

8.1.2 Monolithic Multiple Colour InGaN/GaN MQWs

Based on the overgrowth of (11-20) GaN on micro-rod templates, a multiple-facet structure which consists of only semi-polar and non-polar GaN facets has been fabricated. Due to the different indium incorporation efficiencies on semi-polar and non-polar facets, multiple-colour InGaN/GaN MQWs were achieved on such a structure. PL measurements show that it is possible to tune the intensity ratio of different wavelength emissions simply by controlling the facet area ratio through changing the overgrowth conditions. CL measurements further confirmed the emissions with different wavelengths from different semi-polar and non-polar facets.

8.1.3 Optical and Polarisation Properties of non-polar InGaN MQW LED

The study on the optical and polarisation properties of non-polar (11-20) InGaN/GaN LED was carried out by means of PL, confocal PL and EL measurements. PL measurements show that such non-polar LED exhibits a double peak emission, which is found to be related to the underlying micro-rod pattern. The power-depend EL measurements show that the blue-shift is negligible, indicating that the QCSE is effectively suppressed and the piezoelectric field is nearly eliminated. Polarisation measurements reveal that the polarisation ratio for both emissions is nearly independent of the injection current, while the emission with higher indium composition has larger polarisation degree. It is also found that the energy separation between m-polarised and c-polarised emissions increases with the increasing of injection current for both emissions.

8.1.4 Double Overgrowth of (11-20) GaN on micro-rod/stripe templates

The double overgrowth approach is evolved from the overgrowth (11-20) GaN on our micro-rod templates. The overgrowth on the micro-rods is a very effective approach to block dislocations with simultaneously maintaining a smooth surface, while the overgrowth on a stripe patterned template is more efficient to block BSFs. By utilizing both approaches, the double overgrowth further improved the crystal quality of overgrown (11-20) GaN. The on-axis XRC shows that the FWHMs further reduced to 227 arcsec along the [0001] direction and 313 arcsec along the [1-100] direction, respectively. TEM measurements further confirmed the defects reduction mechanism. The estimated density of dislocations and BSFs are 5×10^7 cm^{-2} and 1×10^4 cm^{-1}, respectively, which are the best report so far.

8.2 Future works

8.2.1 Optimisation and Fabrication of Monolithic Multiple Colour InGaN/GaN LED

We have demonstrated that it is possible to achieve monolithic multiple colour emissions by growing MQWs on a multiple-facet structure, and the intensity ratio of different emissions can be tuned by control the facets ratio through changing the overgrowth conditions. However, to achieve white light, the yellow emission is necessary. That means the indium composition has to be further increased, particularly on the semi-polar facets. In addition, the fabrication of electrically pumped LED on such a multiple-facet structure can be challenging due to the existence of micro-holes on the un-coalescence surface.

8.2.2 Stimulated Emission in Non-polar (11-20) GaN

Due to the utilisation of the overgrowth, the crystal quality of overgrown (11-20) GaN has been significantly improved. Therefore, there is a great chance to achieve a stimulated emission on our overgrown GaN. The stimulated emission can be investigated by using optical pumping and ASE measurements. It is also a good start for the further development of non-polar GaN-based LDs on our overgrown (11-20) GaN.

8.2.3 Growth and Characterisation of Devices on Double Overgrown (11-20) Non-polar GaN on Micro-rod/stripe Template.

The double overgrowth approach has developed by our team very recently. Therefore, there is no device growth/fabrication, and further characterisation needs to be performed in detail. It is expected to see an improvement of performance in devices grown on such (11-20) GaN with a step-change crystal quality.